Theory of Molecular-scale Transport in Nanojunctions

Songjun Hou

This dissertation is submitted for the degree of Doctor of Philosophy

September 2019

Department of Physics, Lancaster University, UK

A journey of a thousand miles begins with a single step.

Declaration

This thesis has not been submitted in support of an application for another degree at this or any other university. This thesis documents work carried out between March 2017 and June 2019 at Lancaster University, UK, under the supervision of Prof. Colin J. Lambert and funded by a Faculty of Science and Technology Scholarship.

Songjun Hou

Sep, 2019

Abstract

It remains a major challenge to identify and exploit room-temperature quantum interference (QI) effects in charge transport through molecular systems at the angstrom scale, although extensive and intensive research has been carried out by experimentalists and theoreticians. In this thesis, I investigate charge transport properties, thermoelectricity and solvent influences at the molecular scale by means of density functional theory (DFT) and equilibrium Green's function theory. The charge transport properties of halide perovskite quantum dots (QDs) are first investigated. It is demonstrated that room-temperature quantum interference (QI) is observed based on the fact that the conductance decays exponentially with the increasing distance between the two gold-gold tips and also there is a distinct conductance "jump" at the end of the sliding process. These findings open the way to new conceptual designs for perovskite-based molecular devices by exploiting QI effects. As for the property of exponentially attenuating electrical conductance with the length, molecular wires with low decaying factor β ($G \sim e^{-\beta l}$) are of significance to realize the molecular electronics. Here we measured and calculated the single-molecule conductances of a series of cumulenes and cumulene analogues, where the number of consecutive C=C bonds in the core is $n = 1, 2, 3$ and 5. The [n]cumulenes with $n = 3$ and 5 have almost the same conductance, and they are both more conductive than the alkene ($n = 1$). The lack of length-dependence in the conductance of [3]cumulene and [5]cumulene is attributed to the strong decrease in HOMO-LUMO gap with increasing length. The conductance of the allene ($n = 2$) is much lower, due to its twisted geometry. Therefore, I

suggest the cumulene series as a good candidate for high conductance molecular wires. Additionally, and also significantly, seeking materials for harvesting energy is an urgent task facing the serious global energy shortage. Herein, I investigated the electrical and thermoelectrical properties of glycine chains with and without cysteine terminal groups. The electrical conductance of $(Gly)_n$, $(Gly)_nCys$ and $Cys(Gly)_nCys$ molecules (where Gly, Cys represent glycine and cysteine and n=1-3) was found to decay exponentially with length l as $e^{-\beta l}$ ($\beta \sim 1.0$ Å^{-1}). Furthermore, it is shown the $(Gly)_1Cys$ and $Cys(Gly)_1Cys$ systems show good thermoelectrical performance (high Seebeck coefficients $\sim$ 0.2 mV/K). With the contributions of both electrons and phonons taken into consideration, a high figure of merit ZT=0.8 is obtained for $(Gly)_1Cys$ at room temperature, suggesting that peptide-based SAM junctions are promising candidates for thermoelectric energy harvesting. In the investigations of charge transports above, it is realized that the functionalities, reproducibility, stability of molecular junctions not only depend on the functional-molecular cores, but also on other effects such as connecting anchors and solvents. Therefore the conductances of single-molecule junctions with different anchoring groups in a variety of solvent environments are studied. It is found that the conductance of single-molecule junctions can be manipulated by nearly an order of magnitude by varying the solvent, and the solvent gating effect depends significantly on the choice of anchor group. My work suggests that the solvent-molecule interaction can provide significant solvent gating effect for the weakly coupled (-SMe anchor) single-molecule junctions.

Acknowledgements

First and foremost, I would like to thank my supervisor, Professor Colin J. Lambert, without whose encouragement, guidance and valuable discussion this thesis would be impossible to complete. The tutorials he delivered in the first year of my PhD study help to have an intensive understanding of Transport Theory. Then I would thank my beloved wife and colleague, Qingqing Wu who gives me the largest support and encouragement for everything. She gives me courage to challenge myself and also do challenging research. I also would like to thank the experimental collaborators from Oxford University and Liverpool University i.e. Prof. Harry L. Anderson, Wenjun Xu, Prof. Richard J. Nichols, Prof. Simon J. Higgins and Dr. Edmund Leary. I also want to thank my collaborators from Prof. Wenjing Hong's group in Xiamen University i.e. Haining Zheng and Zheng Tang. I am also so grateful for discussions with Steven Bailey and Iain Grace, and help from Michael and many others in Colin's group. I would like to thank the Faculty of Science and Technology for providing a studentship. And finally, I would thank my beloved parents and younger sister who support me all the way to pursue my dream. I am really grateful for their love and understanding.

List of publications

[1] “Thermoelectric properties of oligoglycine molecular wires,” Songjun Hou, Qingqing Wu, Hatef Sadeghi and Colin J. Lambert, Nanoscale, 11, 3567-3573, 2019.

[2] “Unusual Length-Dependence of Conductance in Cumulene Molecular Wire,” Wenjun Xu#, Edmund Leary#, Songjun Hou#, Sara Sangtarash, Teresa González, Gabino Rubio-Bollinger, Qingqing Wu, Hatef Sadeghi, Lara Tejerina, Kirsten Christensen, Nicolás Agraït, Simon Higgins, Colin Lambert, Richard Nichols, Harry Laurence Anderson, Angew. Chem. 131, 8466-8470, 2019

[3] “A single-molecule porphyrin-based switch for graphene nano-gaps”, Qingqing Wu, Songjun Hou, Hatef Sadeghi, Colin J Lambert, Nanoscale, 10, 6524-6530, 2018

[4] “Atomically defined angstrom-scale all-carbon junctions”, Zhibing Tan, Dan Zhang, Han-Rui Tian, Qingqing Wu, Songjun Hou, Jiuchan Pi, Hatef Sadeghi, Zheng Tang, Yang Yang, Junyang Liu, Yuan-Zhi Tan, Zhao-Bin Chen, Jia Shi, Zongyuan Xiao, Colin Lambert, Su-Yuan Xie, Wenjing Hong, Nature Communications, 10, 1748, 2019

[5] “Low-Frequency Noise in Graphene Tunnel Junctions”, Paweł Puczkarski, Qingqing Wu, Hatef Sadeghi, Songjun Hou, Amin Karimi, Yuewen Sheng, Jamie H Warner, Colin J Lambert, G Andrew D Briggs, Jan A Mol, ACS nano, 12, 9451-9460, 2018

[6] “Room-temperature Quantum Interference in Perovskite Quantum Dot Junctions”, Haining Zheng,# Songjun Hou,# Chenguang Xin,# Qingqing Wu, Feng Jiang, Zhibing Tan, Xin Zhou, Yuelong Li, Jueting Zheng, Jiuchan Pi, Longyi Zhang, Wenxiang He, Qingmin Li, Junyang Liu, Yang Yang, Jia Shi, Xiaodan Zhang, Ying Zhao, Colin Lambert, Wenjing Hong, submitted to Nature Communications

[7] “Solvent-induced gating of charge transport through single-molecule junctions”, Zheng Tang,# Songjun Hou,# Qingqing Wu, Zhibin Tan, Jueting Zheng, Ruihao Li, Junyang Liu, Yang Yang, Hatef Sadeghi, Jia Shi, Iain Grace, Colin J. Lambert, and Wenjing Hong, submitted to JPCL

[8] “Charge transport through hydrogen bonded supramolecular oligoglycine wires”, Songjun Hou, Qingqing Wu, Haining Zheng, Runze He, Xiantao Guan, Colin J. Lambert, Wenjing Hong, submitted to Nanoscale

Contents

1 Introduction

The transistor is the essential building block of modern electronic devices. Since smaller transistors are more efficient, companies have been trying to make the transistor smaller and smaller. Forty years ago, the size of a transistor is about 10 μm, while the current transistors have reached the dimensions of less than 5 nm in research devices.[1][2] However, further miniaturization of electronic devices based on conventional top-down lithography remains challenging not only from the perspective of technique limitations, but also due to the lack of fundamental understanding of transport mechanisms.[3] Consequently silicon technology is unlikely to be reduced to molecular level (on the order of 1 nm).[4] In this sense, the bottom-up fabricated molecular-scale electronics has the potential to partly replace the silicon transistor in the future, since they can accomplish a variety of electronic functionalities including rectification,[5][6] memory and switching.[7][8] Additionally, molecular-level devices provide potential ways to

extend Moore's Law, which predicts the limits of conventional silicon integrated circuits due to the prospect of size reduction.[9]

Molecular electronics treats single molecules or self-assembled monolayers (SAMs) as functional cores in circuits, which brings the scale down to a regime where quantum mechanics effects could be observed and are important. In the early 1970s, the concept for using the intrinsic functionality of molecules for electronic devices was first proposed by Arieh Aviram and Mark Ratner.[10] They theoretically demonstrated a molecule could show rectifier property when this molecule consists of a donor π systems and an acceptor π system, separated by a sigma-bonded (methylene) tunnelling bridge. On the other hand, the pioneering experiments were carried out by Hans Kuhn and Dietmar Möbius, where the single layers of molecules were used to form functional units.[11] It took the researchers about 20 years to set up the first junction to measure the transport through a single molecule.[12] In this measurement, scanning tunnelling microscopy (STM) was used, as shown in Figure 1-1a. Through controlling the tip up and down, a single molecule could be embedded between the gold tip and the gold substrate. Another widely used measurement method is the mechanically controlled break junction (MCBJ), as shown in Figure 1-1b, which was first introduced by Moreland *et al.* and Muller *et al.* [13], [14] First a notched metal wire is glued onto a substrate, which could be bent by a piezo-controlled pushing rod. When the substrate is bent gradually, this wire is elongated and finally fractured, forming two sharp electrodes and a nanogap. Then the nearby molecule with two terminal anchoring groups come and connect the two electrodes. [15] Recently, a new type of MCBJ based on $\pi - \pi$ stacking was developed shown in Figure 1-3, where graphene

coated coper wires are utilized as electrodes and series of fullerenes have been sandwiched to form all-carbon electronic device.

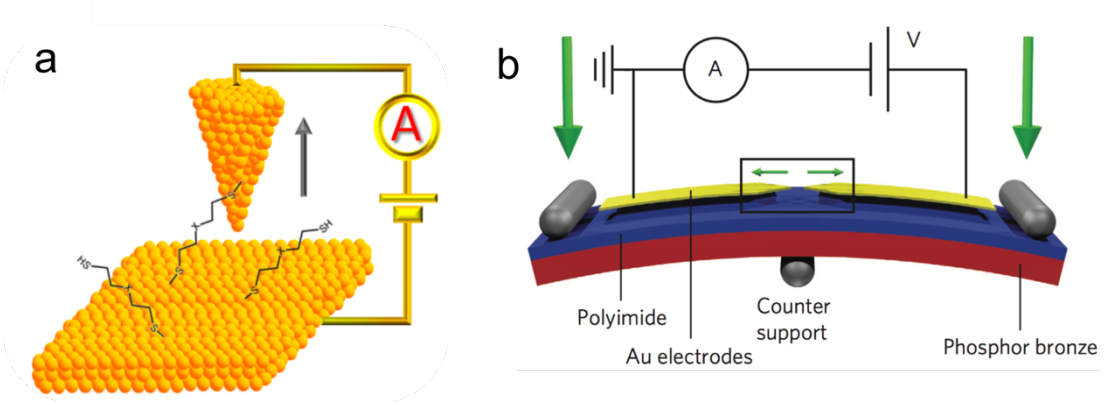

Figure 1-1 Schematic illustration of (a) scanning tunnelling microscopy (STM)[16] **and (b) mechanically controlled break junction (MCBJ).**[17]

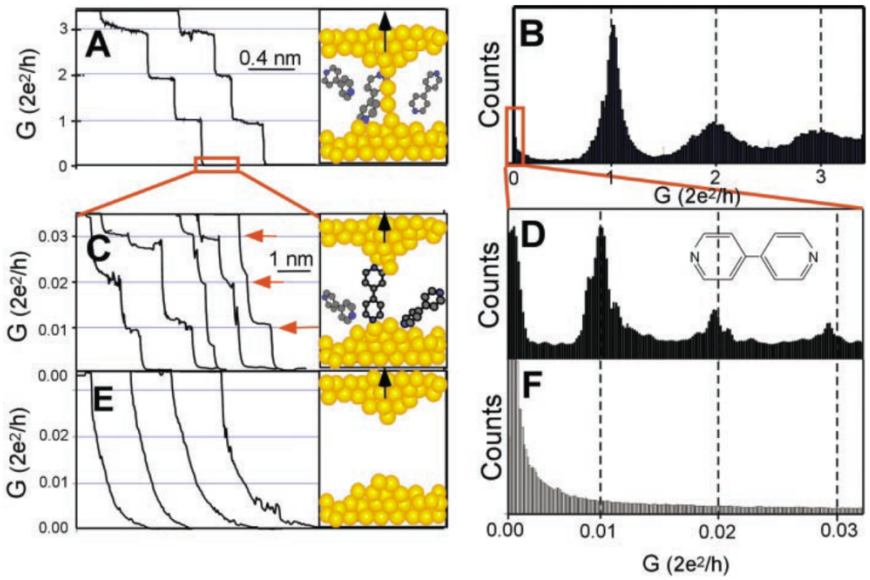

Figure 1-2 Utilizing conductance histograms to identify single-molecule electrical conductance. (A) The conductance of a gold contact formed between the STM tip and the substrate decreases in quantized units of $G_0 = \frac{2e^2}{h}$ as the tip is pulled away. (B) Corresponding conductance histogram shows well-defined peaks near 1 G_0, 2 G_0, 3 G_0 due to conductance quantization. (C) The tip-substrate contact is broken, new conductance steps appear if molecules are present in the solution. These conductance steps arise from the formation of a molecular junction between the

tip and the substrate electrodes. (D) Conductance histogram of the molecular junction depicted in (C) shows peaks near 0.01 G_0, 0.02 G_0, 0.03 G_0 that are ascribed to one, two and three molecules, respectively. (E and F) As a control experiment, no such steps or peaks are observed in the absence of molecules.[18]

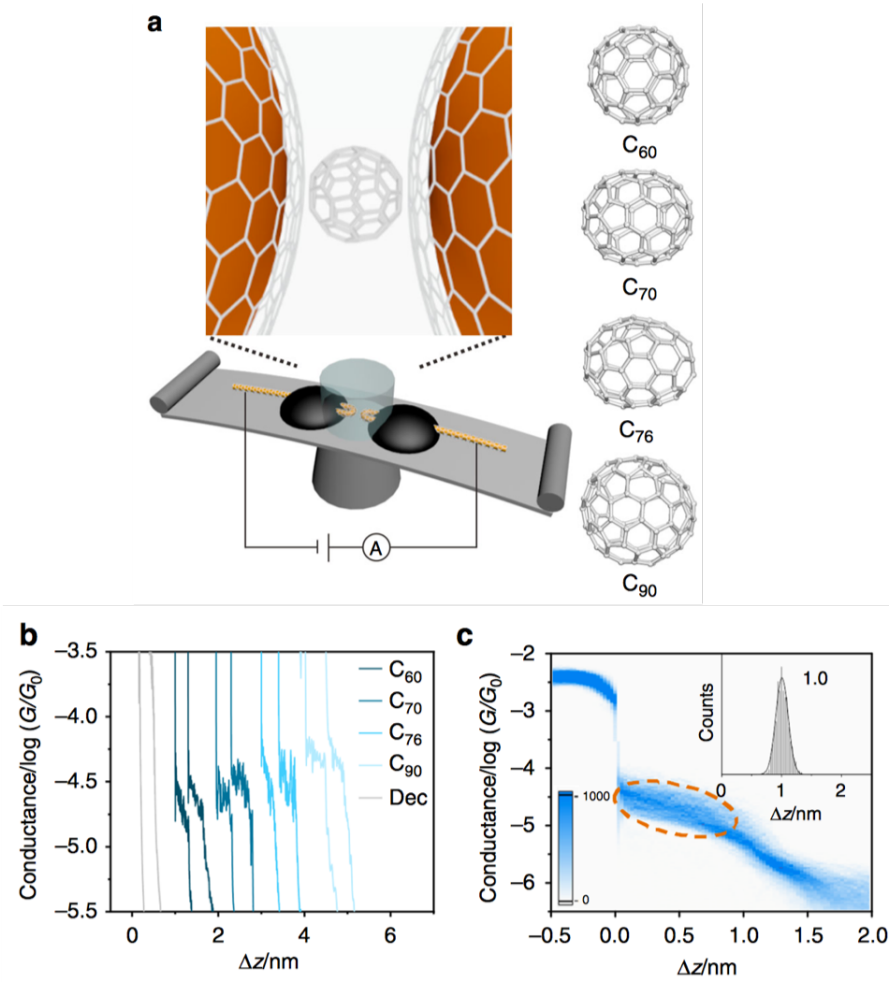

Figure 1-3 2d conductance measurement of C_{60}, C_{70}, C_{76} and C_{90} in graphene vertical junction (a) Schematic of the MCBJ graphene vertical junction and the chemical structures of these molecules. (b) Typical individual conductance-displacement curves. (c) Two-dimensional conductance histogram.[19]

Although the molecules could be wired into junctions using an STM or MCBJ, unequivocally identifying the conductance of a single molecule between metallic electrodes is still challenging, since the measured conductance depends on the metal-molecule contact geometry. It is natural to use a statistical method to

quantify the conductance of a molecular junction. This so-called conductance histogram method was first used by Xu and Tao[18] to identify the conductance of a molecular junction with 1000 conductance curves, as shown in Figure 1-2, where thousands of conductance curves are generated by repeatedly moving two metallic electrodes into and out of contact, and then the most probable conductance is identified. Furthermore, the conductance curves could be shown in 2-dimensional mode, as shown in Figure 1-3c, which shows in the pulling process, a plateau appears indicating the formation of a junction. The length of the plateau means the amount of elongation a junction can sustain before breaking.

The modern transport theory used to describe such experiments is based on scattering theory and Landauer formula, which are described in the next chapter.

2 Transport theory

As discussed in the Introduction, there has been impressive progress in the field of molecular electronics from the experimental point of view. In this chapter, I would like to discuss the transport theory, specifically, the equilibrium Green's Function approach combined with density functional theory. First I shall introduce the Landauer formula, since it correlates current (conductance) with transmission function and then as an example, derive the transmission formula from a simple tight binding model. Finally, a brief description of density functional theory is given.

2.1 Bond currents and the Landauer formula

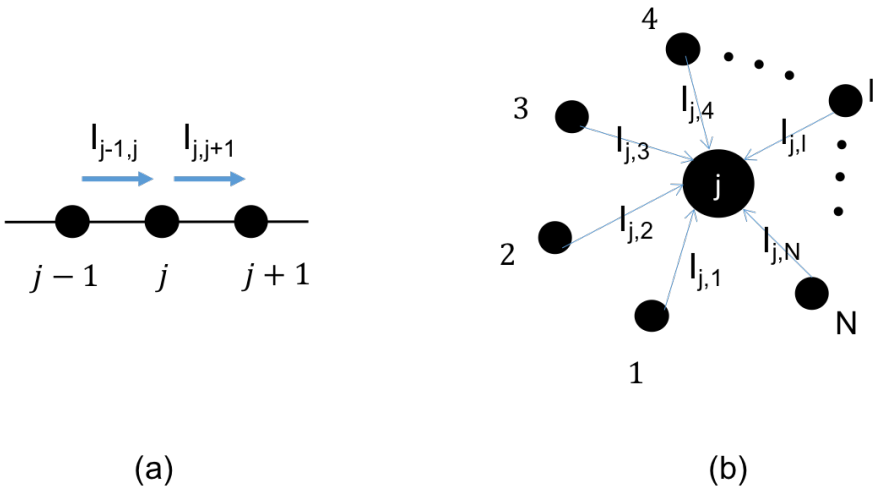

(a) (b)

Figure 2-1 Schematic of bond current through site j connected with two sites (a) and N sites (b).

For a N-site system, the magnitude of current going from one site to another could be derived by considering the time dependant Schrödinger equation, which could be written as

$$i\hbar\frac{d\boldsymbol{\phi}_j(\boldsymbol{t})}{\boldsymbol{dt}}=\sum_{\boldsymbol{l=1}}^{\boldsymbol{N}}\boldsymbol{H}_{j,l}\boldsymbol{\phi}_l(\boldsymbol{t}) \qquad (2.1)$$

Here j, l label the sites and H is the Hamiltonian. As shown in Figure 1-1(a), we can then write current as

$$\frac{\boldsymbol{dP}_j(\boldsymbol{t})}{\boldsymbol{dt}}=\boldsymbol{I}_{j-1,j}-\boldsymbol{I}_{j,j+1} \qquad (2.2)$$

Where $P_j(t)=\left|\phi_j(t)\right|^2=\phi_j^*(t)\phi_j(t)$. To obtain expressions for the currents, substitute Eq. (2.1) into (2.2), to yield

$$\frac{\boldsymbol{dP}_j(\boldsymbol{t})}{\boldsymbol{dt}}=\frac{\boldsymbol{1}}{\boldsymbol{i\hbar}}\sum_{\boldsymbol{l=1,l\neq j}}^{\boldsymbol{N}}\left[\boldsymbol{\phi}_j^*(\boldsymbol{t})\boldsymbol{H}_{jl}\boldsymbol{\phi}_l(\boldsymbol{t})-\boldsymbol{\phi}_j(\boldsymbol{t})\boldsymbol{H}_{jl}^*\boldsymbol{\phi}_l^*(\boldsymbol{t})\right] \qquad (2.3)$$

Here, the contributions coming from site 1 to site N are considered, as shown in Figure 2-1(b). Since the two items on the right of Eq. (2.3) are conjugated, $\frac{\mathrm{dP_j(t)}}{\mathrm{dt}}=\frac{2}{\hbar}Im(\phi_j^*(t)H_{jl}\phi_l(t))$. Therefore, if we consider a one dimensional infinite chain with a hopping element γ, whose eigenstate is a plane wave $\phi_j=Ae^{ikj}$ carrying

bond current $I = V|A|^2$ at each site for each direction, where $V = \frac{1}{\hbar}\frac{dE}{dk} = \frac{2\gamma}{\hbar} sink$ is the group velocity, while the total bond current through each site is 0. For simplicity therefore, in following discussions we use the plane wave carrying unit current $\phi_j = \frac{1}{\sqrt{V}} e^{ikj}$.

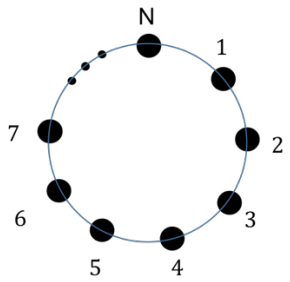

Figure 2-2 N sites ring model. It could be used to derive Landauer formula because its eigenstates include imaginary parts.

To derive the Landauer formula consider the N site ring model shown in Figure 2-2. For this model, the eigenstates are $\phi_j^n = \frac{e^{ikj}}{\sqrt{N}}$, where $k = \frac{2n\pi}{N}$. $n = \frac{Nk}{2\pi}$ $then\ \Delta n = \frac{N}{2\pi}\frac{\Delta k}{\Delta E}\Delta E = \frac{N}{2\pi}\frac{1}{\hbar V}\Delta E$. Meanwhile $\frac{V}{N}$ is the current carried by each state. Therefore the total current carried by Δn states is $\Delta I = \Delta n \times \frac{V}{N} = \frac{1}{h}\Delta E$, meaning the current carried by the the states in the energy interval ΔE is $\frac{1}{h}\Delta E$. If spin is taken into consideration, this doubles to yield

$$\Delta \boldsymbol{I} = \frac{\boldsymbol{2}}{\boldsymbol{h}}\Delta \boldsymbol{E} \qquad (2.4)$$

To study a real device, we consider two ideal reservoirs with different temperature.

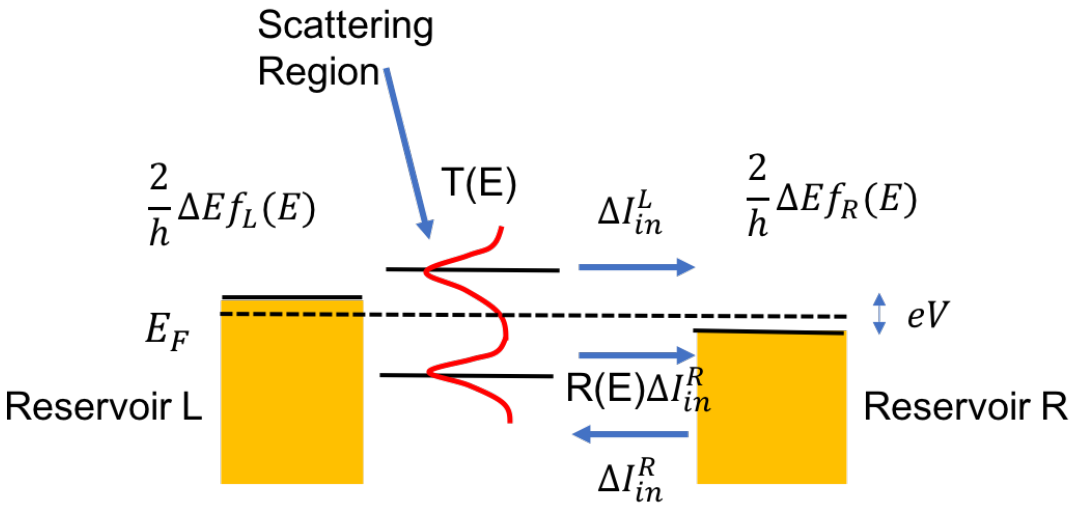

Figure 2-3 Two ideal reservoirs with a scattering region in between. The two black lines mean two energy levels and the transmission function is described by T(E). The number of electrons sent from the left and right reservoirs are $\frac{2}{h}\Delta E f_L(E)$ and $\frac{2}{h}\Delta E f_R(E)$ separately, where $f_{L,R}(E)$ is Fermi-Dirac distribution. On the right side of scattering region, the currents coming from these two electrodes are presented. The potential difference eV between two leads is due to the voltage applied.

As shown in Figure 2-3, the current transported through the scattering region is $\Delta I = \Delta I_{in}^L + R(E)\Delta I_{in}^R - \Delta I_{in}^R = \frac{2}{h}\Delta E[T(E)f_L(E) + (R(E)-1)f_R(E)] =$ $\frac{2}{h}\Delta E T(E)[f_L(E) - f_R(E)]$, where R(E) is the reflection coefficient, $R(E) + T(E) = 1$, $\Delta I_{in}^L, \Delta I_{in}^R$ are the currents coming from left, right leads respectively, $f_{L,R} = 1/(e^{\frac{E-E_F^{L,R}}{k_B T_{L,R}}} + 1)$ is the Fermi-Dirac distribution of the left and right reservoir, k_B is Boltzmann's constant. After integrating over all energies, we obtain the Landauer formula

$$\boldsymbol{I = \frac{2}{h}\int_{-\infty}^{+\infty} dE T(E)(f_L(E) - f_R(E))} \qquad (2.5)$$

If we consider one electron per state, $q = -|e|$, $|e|$ is the charge of a proton

$$\boldsymbol{I^q = \frac{2q}{h}\int_{-\infty}^{+\infty} dET(E)(f_L(E) - f_R(E))} \qquad (2.6)$$

If we set the voltage difference between the left and right reservoirs to be V, then $E_F^{left} = E_F - \frac{qV}{2}$ and $E_F^{right} = E_F + \frac{qV}{2}$. Therefore, the approximation at zero temperature is

$$\boldsymbol{I^q = \frac{2q}{h}\int_{E_F+\frac{qV}{2}}^{E_F-\frac{qV}{2}} dET(E)} \qquad (2.7)$$

For Eq. (2.6), we can do Taylor expansion for $f_L(E)$ and $f_R(E)$ and ignore the items higher than 1st order, we get

$$\boldsymbol{I = \frac{2}{h}\int_{-\infty}^{+\infty} dE\left(-\frac{\partial f}{\partial E}\right)T(E)[\frac{E - E_F}{T}\Delta T + q\Delta V]} \qquad (2.8)$$

, where $\Delta T = \mathrm{T_L} - T_R, \Delta V = \mathrm{V_L} - V_R$, $\mathrm{T_{L,R}}$ and $\mathrm{V_{L,R}}$ mean the temperature and voltage of left lead and right lead respectively. Then, if we consider the charge or heat carried by this transmitted electron. We get

$$\begin{pmatrix} I^q \\ \dot{Q} \end{pmatrix} = \frac{2}{h}\begin{pmatrix} q^2 L_0 & \frac{qL_1}{T} \\ qL_1 & \frac{L_2}{T} \end{pmatrix}\begin{pmatrix} \Delta V \\ \Delta T \end{pmatrix} \qquad (2.9)$$

In which, $L_n = \int_{-\infty}^{+\infty} dE \left(-\frac{\partial f}{\partial E}\right) T(E)(E - E_F)^n$ and $q = -|e|$ is the electronic charge. At finite temperature, if $\Delta T = 0$, $I^q = \frac{2}{h} q^2 L_0 \Delta V = G\Delta V$**.** So

$$\boldsymbol{G = \frac{2q^2}{h} L_0 = \frac{2q^2}{h} \int dE \left(-\frac{\partial f}{\partial E}\right) T(E)} \qquad (2.10)$$

In the low temperature limit, $-\frac{\partial f}{\partial E} \approx \delta(E - E_F)$, and using $\int dx f(x)\delta(x - a) = f(a)$, then we obtain

$$\boldsymbol{G = \frac{2q^2}{h} T(E_F) = G_0 T(E_F)} \qquad (2.11)$$

, where $G_0 = \frac{2q^2}{h} \approx 7.7 \times 10^{-5}\ S$, is the quantum of conductance. If we set $I^q = 0$**,** Eq. 2.9 becomes

$$\boldsymbol{\frac{\Delta V}{\Delta T} = -\frac{L_1}{q L_0 T} = -S} \qquad (2.12)$$

, where S is Seebeck coefficient describing the induced thermoelectric voltage in response to a unit temperature difference across the material. Eq. (2.9) can be rewritten as

$$\begin{pmatrix} \boldsymbol{\Delta V} \\ \boldsymbol{\dot{Q}} \end{pmatrix} = \begin{pmatrix} \boldsymbol{1/G} & \boldsymbol{S} \\ \boldsymbol{\Pi} & \boldsymbol{\kappa_e} \end{pmatrix} \begin{pmatrix} \boldsymbol{I^q} \\ \boldsymbol{\Delta T} \end{pmatrix} \qquad (2.13)$$

, where $\Pi = \frac{-L_1}{qL_0}$ is Peltier coefficient, $\kappa_e = \frac{2}{hT}(L_2 - \frac{L_1^2}{L_0})$ is the electronic contribution to the thermal conductance. For energy E close to Fermi energy E_F, if transmission function T(E) varies approximately linearly with E on the scale of $k_B T$,

then we get $L_0 \approx T(E_F)$, $L_1 \approx (qT)^2 \alpha \left(\frac{dT(E)}{dE}\right)_{E=E_F}$ and $L_2 \approx (qT)^2 \alpha T(E_F)$ where $\alpha = \left(\frac{1}{qT}\right)^2 \int_{-\infty}^{+\infty} dE \left(-\frac{\partial f}{\partial E}\right)(E - E_F)^2 = \left(\frac{K_B}{q}\right)^2 \frac{\pi^2}{3} =$ 2.44x10^{-8} WΩK^{-2} is the Lorenz number. Hence in this limit, we get

$$\boldsymbol{S \approx -\alpha |e| T \left(\frac{dlnT(E)}{dE}\right)_{E=E_F}} \qquad (2.14)$$

$$\boldsymbol{\kappa_e \approx \alpha T G} \qquad (2.15)$$

. Eq. (2.14) means the Seebeck coefficient is proportional to the slope of the transmission function on a logarithmic scale at Fermi energy. Eq. (2.15) is called the Wiedemann-Franz Law tells us that the thermal conductance due to electrons is linearly correlated with the electrical conductance.

The thermoelectric efficiency is characterized by a dimensionless thermoelectric figure of merit

$$\boldsymbol{ZT = \frac{GS^2T}{\kappa_e + \kappa_p}} \qquad (2.16)$$

, where T is the reference temperature, κ_e, κ_p are thermal conductances due to electrons and phonons separately. If we ignore the contribution coming from phonons, the electronic figure of merit $ZT_e = \frac{GS^2T}{\kappa_e} = \frac{(L_1)^2}{L_0 L_2 - (L_1)^2}$, recalling Wiedemann-Franz Law, $ZT_e = \frac{GS^2T}{\kappa_e} \approx \frac{GS^2T}{\alpha TG} = \frac{S^2}{\alpha}$. Then if we want $ZT_e > 1$, then S > 150 μV/K is required.

In practice, to calculate the thermal conductance due to phonons, the force constant matrix, *K*, is obtained by finite differences

$$\boldsymbol{K_{i\alpha,j\beta}} = \frac{\boldsymbol{\partial^2 E}}{\boldsymbol{\partial r_{i\alpha}\partial r_{j\beta}}} = -\frac{\boldsymbol{F_{j\beta}(Q_{i\alpha}) - F_{j\beta}(-Q_{i\alpha})}}{\boldsymbol{2Q_{i\alpha}}} \quad (2.17)$$

, where E is the total energy and $r_{i\alpha}(r_{i\beta})$ is the displacement of atom $i(j)$ in the coordinate direction $\alpha(\beta)$. In my calculations below, the geometry is relaxed using SIESTA [20] until the force of each atom is smaller than 0.02 eV/Å. By shifting each atom (i) by $Q_{i\alpha} = \pm 0.01$ Å in the direction $\alpha = x, y, z$, the forces on atom along $\beta = x, y, z$ direction, $F_{j\beta}(Q_{i\alpha})$ is calculated. The dynamical matrix D can be obtained by $D_{i\alpha,j\beta} = K_{i\alpha,j\beta}/\sqrt{m_i m_j}$, where m_i (m_j) is the mass of atom $i(j)$. Then the dynamical matrix is used to compute the transmission probability of phonons. The corresponding phononic thermal conductance is given by

$$\boldsymbol{\kappa_p(T)} = \int_0^\infty \frac{\hbar\boldsymbol{\omega}}{\boldsymbol{2\pi}} \boldsymbol{T_p(\omega)} \frac{\boldsymbol{\partial f_{BE}(\omega, T)}}{\boldsymbol{\partial T}} \boldsymbol{d\omega} \quad (2.18)$$

, where $f_{BE}(\omega, T) = 1/[e^{\left(\frac{\hbar\omega}{k_B T}\right)} - 1]$ is the function of Bose-Einstein distribution, $T_p(\omega)$ is the phonon transmission function . Then, the full figure of merit can be given by Eq. (2.16).

Therefore, to obtain charge and heat currents due to electrons or phonons, their transmission functions are needed. In section 2.2, I shall discuss how to use a simple model to derive the transmission formula based on quantum scattering theory, whose general form is implemented in the transport code Gollum.[21]

2.2 Transmission function

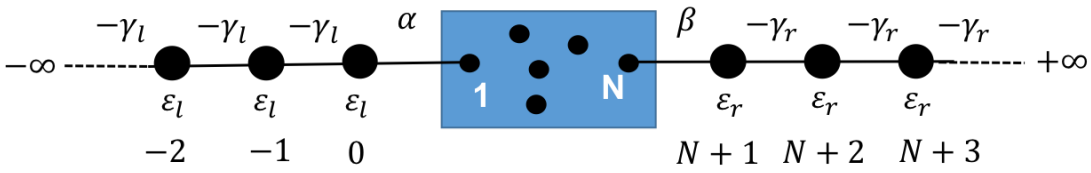

Figure 2-4 A scattering region connected with two semi-infinite one-dimensional leads. The left and right leads are two semi infinite one-dimensional chains with on-site energy $\varepsilon_{l,r}$ and hopping integral $-\gamma_{l,r}$. The sites are labeled as ... -2, -1, 0, ..., 1, ..., N, ..., N+1, N+2, N+3, ...

As an example of the transmission and reflection coefficients of electrons with energy E passing through a scattering region, I consider the simple tight binding model s shown in Figure 2-4, in which a scattering region with N sites is connected to two semi-infinite one-dimensional leads through sites 1 and N. Then the wavefunctions in the left lead and right lead are: $\phi_j = \frac{e^{ik_L j} + re^{-ik_L j}}{\sqrt{v_L}}$ and $\psi_j = \frac{te^{-ik_R j}}{\sqrt{v_R}}$ respectively, where r and t are reflection and transmission amplitudes while the v_L and v_R are the group velocities. The wave function in the scattering region will be denoted f_j (j=1-N). The Schrodinger equation for the wavefunctions in different parts of the system is:

$$j \le -1 \qquad \boldsymbol{\varepsilon_L \phi_j - \gamma_L \phi_{j-1} - \gamma_L \phi_{j+1} = E\phi_j} \qquad (2.19)$$

$$j = 0 \qquad \boldsymbol{\varepsilon_L \phi_0 - \gamma_L \phi_{-1} - \alpha f_1 = E\phi_0} \qquad (2.20)$$

$$j = 1 \qquad \boldsymbol{\sum_{i=1}^{N} H_{1i} f_i - \alpha \phi_0 = E f_1} \qquad (2.21)$$

$2 \le j \le N-1$ $$\sum_{i=1}^{N} \boldsymbol{H_{ji} f_i = E f_j} \quad (2.22)$$

$j = N$ $$\sum_{i=1}^{N} \boldsymbol{H_{Ni} f_i - \beta \psi_{N+1} = E f_N} \quad (2.23)$$

$j = N+1$ $$\boldsymbol{\varepsilon_R \psi_{N+1} - \beta f_N - \gamma_R \psi_{N+2} = E \psi_{N+1}} \quad (2.24)$$

$j \ge N+2$ $$\boldsymbol{\varepsilon_R \psi_j - \gamma_R \psi_{j-1} - \gamma_R \psi_{j+1} = E \psi_j} \quad (2.25)$$

At j=0 and N+1, using continuity, we could get

$$\boldsymbol{\alpha f_1 = \gamma_L \phi_1} \quad (2.26)$$

$$\boldsymbol{\beta f_N = \gamma_R \psi_N} \quad (2.27)$$

. Based on Eq. (2.21), (2.22) and (2.23), we also get

$$\boldsymbol{(E-H)} \begin{pmatrix} \boldsymbol{f_1} \\ \vdots \\ \boldsymbol{f_N} \end{pmatrix} = \begin{pmatrix} \boldsymbol{-\alpha \phi_0} \\ \vdots \\ \boldsymbol{-\beta \psi_{N+1}} \end{pmatrix} \quad (2.28)$$

. If we set $g = \frac{1}{E-H} = \begin{pmatrix} g_{11} & \cdots & g_{1N} \\ \vdots & \ddots & \vdots \\ g_{N1} & \cdots & g_{NN} \end{pmatrix}$, $\hat{g} = \begin{pmatrix} g_{11} & g_{1N} \\ g_{N1} & g_{NN} \end{pmatrix}$ then

$$\begin{pmatrix} \boldsymbol{-\alpha \phi_0} \\ \boldsymbol{-\beta \psi_{N+1}} \end{pmatrix} = \boldsymbol{\hat{g}^{-1}} \begin{pmatrix} \boldsymbol{f_1} \\ \boldsymbol{f_N} \end{pmatrix} \quad (2.29)$$

. Solving Eq. (2.26), (2.27) and (2.29), we can obtain the transmission coefficient

$$\boldsymbol{T = |t|^2 = 4 \Gamma_L \Gamma_R |G_{N1}|^2} \quad (2.30)$$

, where $\Gamma_{L,R} = Im(\Sigma_{L,R})$, $\Sigma_L = \frac{-\alpha^2 e^{ik_L}}{\gamma_L} = \sigma_L - i\Gamma_L$, $\Sigma_R = \frac{-\beta^2 e^{ik_R}}{\gamma_R} = \sigma_R - i\Gamma_R$, then $\Gamma_L = \frac{\alpha^2 sink_L}{\gamma_L}$, $\Gamma_R = \frac{\beta^2 sink_R}{\gamma_R}$, $G_{N1} = \frac{g_{N1}}{\Delta}$, $\Delta = 1 - g_{11}\Sigma_L - g_{NN}\Sigma_R + \Sigma_L\Sigma_R(g_{11}g_{NN} - g_{1N}g_{N1})$.

The above expression is valid for any phase coherent tight-binding scatterer connected to one dimensional leads. In the following, I shall discuss two examples, which illustrate generic behaviours which occur when the energy of an electron, one is either to an energy level of the scatterer (resonant transport), or between two levels (off-resonance transport).

2.2.1 Breit-Wigner formula

The Green's function of a closed system can be written as $g = \frac{1}{E-H} = \sum_{i=1}^{N} \frac{|\lambda_n><\lambda_n|}{E-H} = \sum_{i=1}^{N} \frac{|\lambda_n><\lambda_n|}{E-\lambda_n}$, where λ_n, $|\lambda_n>$ $(n = 1 \dots N)$ are the eigenvalues and eigenstates of a system with a NxN Hamiltonian H. For simplicity, we assume there are no degeneracies. In principle, all the eigenstates contribute to the Green's function. However, when the energy of electron is close to one level, the Green's function is dominated by the eigenstate corresponding to that level. For example, when $E \approx \lambda_n$

$$\boldsymbol{g \approx \frac{|\lambda_n><\lambda_n|}{E-\lambda_n}} \qquad (2.31)$$

Then $g_{ij} = \frac{\varphi_i^n \varphi_j^n}{\mathrm{E}-\lambda_\mathrm{n}}$, where φ_i^n is the amplitude of eigenstate $|\lambda_\mathrm{n}>$ on site i. This yields $g_{11} = \frac{(\varphi_1^n)^2}{\mathrm{E}-\lambda_\mathrm{n}}$, $g_{NN} = \frac{(\varphi_N^n)^2}{\mathrm{E}-\lambda_\mathrm{n}}$, $g_{1N} = g_{N1} = \frac{\varphi_1^n \varphi_N^n}{\mathrm{E}-\lambda_\mathrm{n}}$, and after substituting these parameters into Eq. (2.30), we get the Breit-Wigner formula

$$\boldsymbol{T = \frac{4\tilde{\Gamma}_L \tilde{\Gamma}_R}{\left(E - \tilde{\lambda}_n\right)^2 + \left(\tilde{\Gamma}_L + \tilde{\Gamma}_R\right)^2}} \qquad (2.32)$$

Where $\tilde{\Gamma}_\mathrm{L} = \Gamma_\mathrm{L}(\varphi_1^n)^2 = \frac{\alpha^2 sink_L}{\gamma_L}(\varphi_1^n)^2, \tilde{\Gamma}_\mathrm{R} = \Gamma_\mathrm{R}(\varphi_N^n)^2 = \frac{\beta^2 sink_R}{\gamma_R}(\varphi_N^n)^2$, $\tilde{\lambda}_\mathrm{n} = \lambda_n + \tilde{\sigma}_\mathrm{L} + \tilde{\sigma}_\mathrm{R}$, $\tilde{\sigma}_\mathrm{L} = \sigma_\mathrm{L}(\varphi_1^n)^2 = \frac{-\alpha^2 cosk_L}{\gamma_L}(\varphi_1^n)^2, \tilde{\sigma}_\mathrm{R} = \sigma_\mathrm{R}(\varphi_1^n)^2 = \frac{-\beta^2 cosk_R}{\gamma_R}(\varphi_N^n)^2$. For a non-degenerate closed system, when its energy level spacing is much larger than the coupling $\left(\tilde{\Gamma}_\mathrm{L} + \tilde{\Gamma}_\mathrm{R}\right)$, each of the resonances could be well described by such a Breit-Wigner formula. An example of a three level system is shown in Figure 2-5.

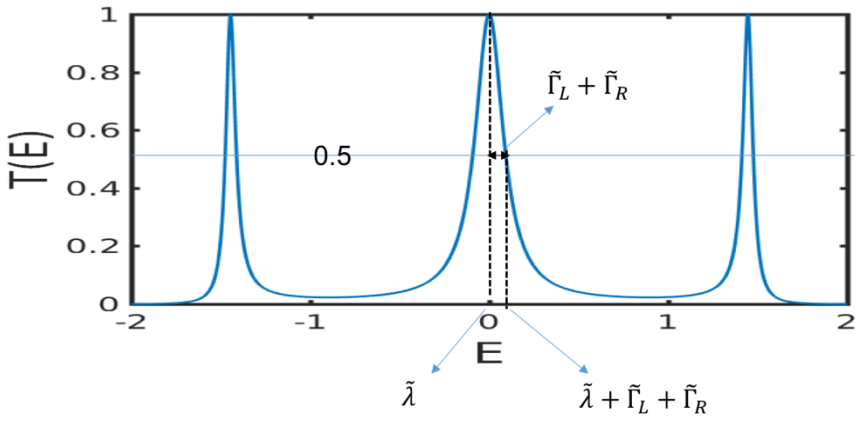

Figure 2-5 The transmission coefficients T(E) of three levels system. Any individual peak could be described by Breit-Wigner foumula. Some features are shown in the middle peak. When $E = \tilde{\lambda}$, The maximum of T(E), $T_{max} = \frac{4\tilde{\Gamma}_\mathrm{L}\tilde{\Gamma}_\mathrm{R}}{(\tilde{\Gamma}_\mathrm{L}+\tilde{\Gamma}_\mathrm{R})^2}$. When $\mathrm{E} = \tilde{\lambda}_\mathrm{n} + \tilde{\Gamma}_\mathrm{L} + \tilde{\Gamma}_\mathrm{R}$, $T = \frac{1}{2}T_{max}$. Therefore, $\tilde{\Gamma}_\mathrm{L} + \tilde{\Gamma}_\mathrm{R}$ is usually named as half width of resonance. For symmetrical system, $\tilde{\Gamma}_\mathrm{L} = \tilde{\Gamma}_\mathrm{R}$, $\mathrm{T_{max}}$=1.

2.2.2 Fano resonance

Normally, electron transport through a molecule is dominated by conduction through broadened highest occupied molecular orbital (HOMO) or lowest unoccupied molecular orbital (LUMO) , resulting in Breit-Wigner resonances. However, in some cases, a localized state coupling to a continuum state is present, which leads to Fano resonance.[22] For simplicity, Eq. (2.32) could be rewritten as $T(E) = \frac{4\Gamma_L\Gamma_R}{(E-\lambda_n)^2+(\Gamma_L+\Gamma_R)^2}$, where λ_n is the nth eigenvalue, then if a 'pendant' orbital λ_p is coupled to λ_n through a hopping element α, Eq. (2.32) is replaced by

$$\boldsymbol{T(E) = \frac{4\Gamma_L\Gamma_R}{(E-\lambda)^2+(\Gamma_L+\Gamma_R)^2}} \qquad (2.33)$$

Where $\lambda = \lambda_n + \frac{\alpha^2}{E-\lambda_p}$ (obtained from the decimation method). When $E = \lambda_p$, λ diverges and leads to an anti-resonance. On the other hand, when $E - \lambda = 0, (E-\lambda_n)(E-\lambda_p) - \alpha^2 = 0$, two resonances are expected at two solutions close to λ_n and λ_p separately. The former is the normal Breit-Wigner resonance, while the latter and the anti-resonance at λ_p forming Fano resonance.

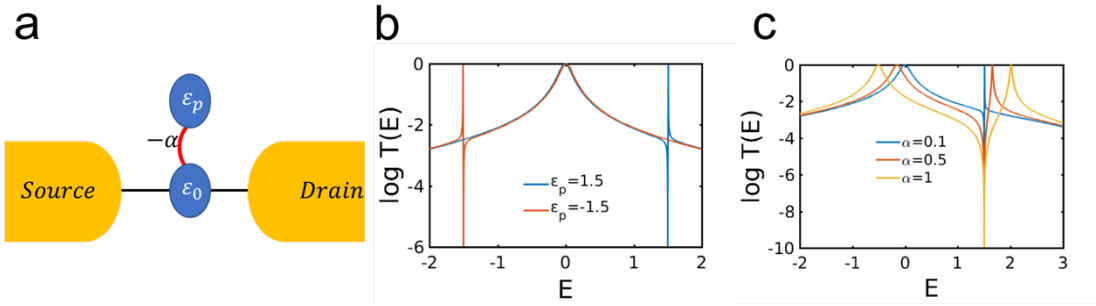

Figure 2-6 Explanation of Fano resonance. (a) The schematic of one site $\varepsilon_0 = 0$ with 'pendant' ε_p attaching to two leads (b) $\varepsilon_p = 1.5$ *or* -1.5 demonstrating the

position of anti-resonance is determined by ε_p (c) $\varepsilon_p = 1.5$ while $\alpha = 0.1, 0.5, 1$ respectively, demonstrating that the positions of the two resonance determined by α, when α is small enough, a typical Fano-resonance is expected as indicated in equation $(E - \lambda_n)(E - \lambda_p) - \alpha^2 = 0$.

2.2.3 Product rule and Mid-gap theory

Instead of considering the energy of electrons flowing through the molecule close to one of the eigenvalues of the system, now we now consider the case where the energy of electrons is located in the HOMO-LUMO gap; in other words, the electron transport is off resonance. In this case, according to the expression of Green's function of a molecule, $g = \sum_{i=1}^{N} \frac{|\lambda_n><\lambda_n|}{E-\lambda_n}$, where λ_n , $|\lambda_n >$ $(n = 1 \dots N)$ are the eigenvalue and eigenstate, the contribution coming from all the eigenstates should be taken into consideration. As an example, consider a fictitious molecule possessing only two orbitals, (a HOMO and LUMO), then Green's function is replaced by

$$\boldsymbol{g_{ij} = C_H \phi_i^H \phi_j^H + C_L \phi_i^L \phi_j^L} \qquad (2.34)$$

In this expression, $C_H = \frac{1}{E_F - E_H}$, $C_L = \frac{1}{E_F - E_L}$, $\phi_i^{H,L}$ and $\phi_j^{H,L}$ are the amplitudes of HOMO (LUMO) at input position i and output position j separately. The physics of the electrode and the chemistry of the molecule are contained in E_F and molecular orbitals respectively. Specially, if we choose $E_F = \frac{E_H + E_L}{2}$, meaning E_F is located in the middle of HOMO − LUMO gap, then $C_L =$

$-C_H = \frac{1}{\delta}$, where δ is half the HOMO-LUMO gap given by $\delta = \frac{E_L - E_H}{2}$, Eq. (2.34) is replaced by mid-gap Green's function

$$\boldsymbol{g_{ij} = \frac{1}{\delta}(\phi_i^H \phi_j^H - \phi_i^L \phi_j^L)} \qquad (2.35)$$

. For simplicity, we denote $a_H = \phi_i^H \phi_j^H$ and $a_L = \phi_i^L \phi_j^L$. The MOs can be positive or negative at different positions, so a_H and a_L could have opposite signs or the same sign, corresponding to destructive quantum interference (QI) or constructive QI respectively. Although in real molecules, all molecular orbitals need to be considered, in many cases, for eigenstates other than the HOMO and LUMO, the larger energetic distance E_n to E_F leads to a larger denominators. Therefore, in these cases, we could get quantitative results even just considering the HOMO and LUMO.

2.3 Scattering theory in practice

Sometimes, it is convenient to use a simple tight binding model to capture the main features of a system. However, in most cases, it is essential to simulate the system at an ab initio level. In this thesis, all the Hamiltonians including electrodes and scattering region are extracted from the DFT (density functional theory) software SIESTA (Spanish Initiative for Electronic Simulations with Thousand of Atoms),[20] which uses strictly localized atomic basis. In the following section, I shall introduce DFT briefly.

In the many-body Schrödinger equation, it is reasonable to ignore the movement of the much heavier nuclei, which is the so called Born-Oppenheimer approximation. Then we can get the Schrödinger equation for many-electron

$$\left\{-\frac{\hbar^2}{2m}\sum_j \nabla_j^2 - \sum_{j,l}\frac{Z_l e^2}{|r_j - R_l|} + \frac{1}{2}\sum_{j\neq j'}\frac{e^2}{|r_j - r_j'|}\right\}\Psi = E\Psi \qquad (2.36)$$

, where r_j are the positions of the electrons and R_l, Z_l are the positions and atomic numbers of the nuclei, Ψ, E are the wave function and energy. Then the solved wave function Ψ depends on the positions (ignoring spin for simplicity)

$$\Psi = \Psi(r_1, r_2, \ldots r_N) \qquad (2.37)$$

. Then if we want to get the solution, the number of degrees of freedom in Eq. (2.33) increases exponentially making this problem computationally intractable. For

example, if we choose the space with $m \times m \times m$ discretized grid, then the dimension of Ψ is m^{3N}. For $m = 10, N = 10$, the dimension is as large as 10^{30} even for this very small system (10 electrons). This difficulty is usually called 'exponential wall'. [23] It is impossible to solve this Schrödinger equation even using the most powerful computers available today.

One way to overcome this barrier is DFT. The prototype Thomas-Fermi theory (TF) appeared in the 1920s, however, it was not clear how to establish a strict connection between the electron density used in TF theory and the wave function used in many-electron Schrodinger equation, until the two Kohn-Hohenberg (H-K) theorems were proposed.[23] The first H-K theorem demonstrates that the ground state properties of a many-electron interacting system are determined by an electron density that depends on only three spatial coordinates. The second H-K theorem also called H-K variational principle, which proves the energy of ground state E could be obtained by minimizing an energy functional, which is a function of the electron density. However, this theory did not become useful at that time because these two theorems do not specify the form of this functional. Later the Kohn-Sham equation, where the system is presented by many independent particles moving in external potential was proposed to solve the problem:

$$\left\{-\frac{\hbar^2}{2m}\nabla^2 + V_{eff}(r)\right\}\Psi(r) = E_{KS}\Psi(r) \qquad (2.38)$$

, the first term is the kinetic energy and the effective potential is:

$$\boldsymbol{V_{eff}(r) = V(r) + \int \frac{n(r)}{|r - r'|} dr' + V_{xc}(r)} \qquad (2.39)$$

Here the first term is the external potential, the second term is the Hartree potential, which represents the electron repulsion and the third term is exchange-correlation potential. As the analytical form of V_{xc} is unknown, several approximations have been derived semi-empirically, in which the local density approximation (LDA) and the generalized gradient approximation (GGA) have been using widely. Since V(r) is induced by the nuclei, the electrons could be divided into two groups: valence electrons and inner core electrons. The inner core electrons don't affect the chemical properties of atoms, and also it is expensive to include them in simulations. Therefore, it is feasible to use a fake potential to describe the potential felt by the valence electrons, namely a 'Pseudopotential'. Then, the Kohn-Sham equation could be solved self-consistently, as shown in Figure 2-7. The resulting mean-field Hamiltonian and overlap matrices were then extracted to be used for computing the electrical properties of the devices with transport code Gollum.[21]

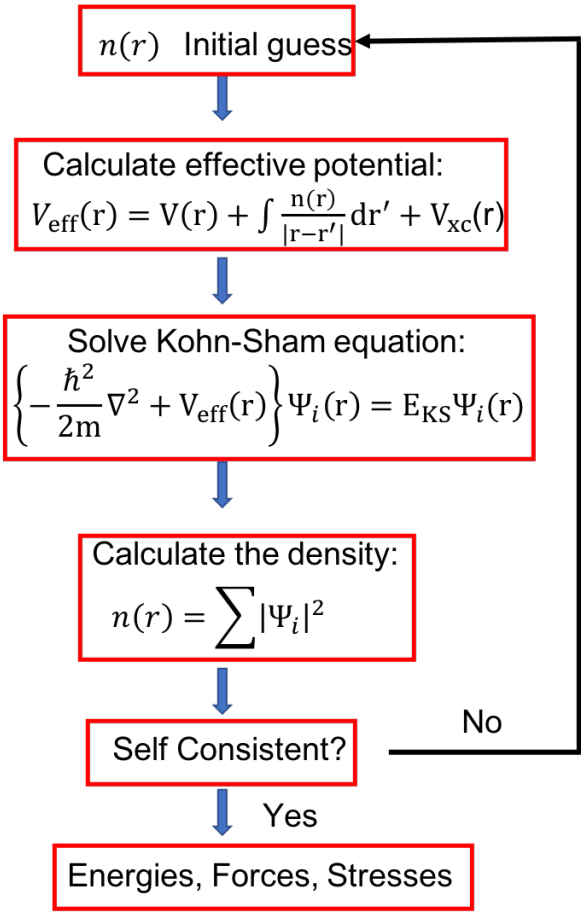

Figure 2-7 The self consistent process of solving Kohn-Sham equation.

3 Room-temperature Quantum Interference in Perovskite Quantum Dot Junctions

Identification and exploitation of room-temperature quantum interference (QI) effects in electron transport through molecular systems at the Ångstrom scale is a major theoretical and experimental challenge. In this work, the experimentalists (Wenjing Hong's group in Xiamen University) report the first observation of QI effects in halide perovskite quantum dots (QDs) using a mechanically controllable break junction (MCBJ) technique. Single-QD conductance measurements reveal that there are multiple distinguishable conductance peaks for the MAPbBr3 and MAPbBr3-xClx perovskite QDs, whose displacement distributions match the lattice constant of QDs, suggesting that during each MCBJ cycle, the gold electrode slides through different lattice sites of the QD, and interacts via Au-halogen coupling. There is a distinct conductance "jump" at the end of the sliding process,

just before the contact breaks, which is further evidence that QI effects dominated charge transport in these single-QD junctions. This conductance jump is confirmed by our theoretical calculations utilizing density functional theory (DFT) combined with quantum transport theory. These findings open the way to new conceptual designs for perovskite-based molecular devices, based on exploiting QI effects.

3.1 Introduction

Quantum interference (QI) effects have attracted great interest in investigations of charge transport through a diversity of single-molecule devices, including molecular switches,[24] thermoelectric devices[25] and molecule field-effect transistors.[26] QI originates from de Broglie waves of electrons traversing different pathways through single-molecule junctions, making it possible to tune their molecular conductance over orders of magnitude by modifying substituent groups [27][28] and molecular topologies. Experimental and theoretical investigations of room-temperature QI effects have focused mainly on organic molecular wires, including linearly conjugated systems,[24] heterocyclic aromatics[29] and even σ-conducting wires,[30] and therefore there is an urgent need to investigate QI-controlled transport in inorganic molecular-scale systems. Here the experimentalist and I identify signatures of room-temperature QI in perovskite-based electronic materials, attracted by their unique quantum yield and high carrier mobility and by a need to understand how their macroscopic charge transport properties lead to quantum effects at the nanoscale.

Perovskite materials are attracting extraordinary attention in applications such as light-emitting diodes (LED),[31] electroluminescence (EL) devices,[32] photodetector[33][34] and solar cells.[35][36] Although there are many experimental investigations of charge transport through bulk perovskites materials, including thin films,[37] nanocrystals[38] and even single crystals,[39] investigations at the nanoscale, to reveal QI effects in their room-temperature transport properties remains a major experimental challenge. Recent extensions of single-molecule charge transport measurements of conjugated molecular families[40] to molecular assemblies,[41][42][43] nanoparticles[44] and clusters,[45] offer an opportunity to gain insight into macroscopic charge transport through Ångstrom-scale perovksite materials. In addition, recently developed Au-halogen interfacial engineering allows the measurement of transport through perovskite single-QD devices.[46][47][48] Here the experimentalists report the first observation of room-temperature QI effects in halide perovskite quantum dots (QDs) at the Ångstrom scale, using a mechanically controllable break junction technique (MCBJ). The measurements and my underpinning theory provide new insight into charge transport through perovskite materials at the Ångstrom scale and create a new pathway to exploit QI effects in quantum-controlled perovskite materials.

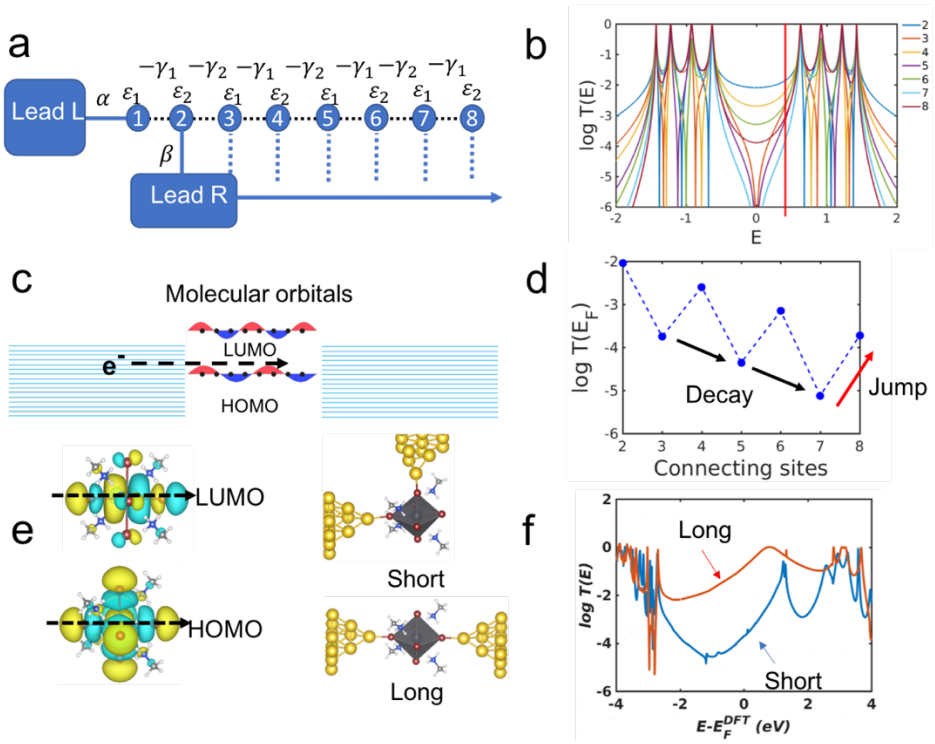

Figure 3-1 The orthogonality of molecular orbitals and quantum interference (QI) of 1Pb cluster. a, Schematic of tight binding model comprising a 8-site diatomic chain as the scattering region, where site 1 is connected to left lead L and sites 2-8 are connected sequentially to right lead R. In this model, all site energies are set to zero. To induce a HOMO-LUMO gap, nearest neighbor hopping integrals are chosen to alternate between $\gamma_1 = 1, \gamma_2 = 0.5$. b, The corresponding transmission functions when lead R is attached different sites from 2 to 8 in a. The Fermi energy is chosen at E_F =0.3 and indicated by the red line. c, Schematic of coherent tunneling across a molecule, where the highest occupied molecular orbital (HOMO) and the lowest unoccupied molecular orbital (LUMO) of a one-dimensional chain of 8 sites are plotted. The red and blue colours denote regions of positive and negative molecular-orbital amplitude. The black dots represent site 1-8 sites in figure a. d, Transmission function $T(E_F)$ at the Fermi energy for different site connections to the right lead. Decaying oscillations and a jump (indicated by the red arrow) in the last connection are observed, which originate from QI. e, Left panel: The HOMO and LUMO of a relaxed 1Pb $MAPbBr_3$ cluster. Note that the number of nodes is 4 and 5 respectively in the direction indicated by the black dashed lines. Right panel: A relaxed 1Pb $MAPbBr_3$ cluster is embedded between two gold electrodes, with two different connections, denoted 'Short' and

'Long' separately. Pb, Br, N, C, H and Au atoms are represented by large gray, purple, blue, small gray, white and yellow balls. f, Transmission spectra for the two connections in figure 1e, showing that the longer path is more conductive than the shorter one.

"On-resonance" transport through quantum dots or molecules is mediated by electrons whose energy coincides with a single molecular orbital (MO), but only occurs when electrostatic or electrochemical gating is used to move the MO energy towards the Fermi energy of the electrodes. In contrast, transport through non-gated molecules is usually "off-resonance" and mediated by electrons whose energy lies within the energy gap between the HOMO and LUMO. Consequently if a succession of measurements is made, with a series of electrode spacings L, then the electrical conductance G decays exponentially as

$$G \sim e^{-\beta L}, \qquad (1)$$

where the attenuation factor β is an increasing function of the energy gap between the HOMO and LUMO. As described in [49][50], in this "co-tunneling" regime, transport is also controlled by inter-orbital QI between the HOMO and LUMO, which can create additional signatures superposed on this exponential trend, and can be understood qualitatively by inspecting the signs of the HOMO and LUMO at the points of contact between the molecule and electrode. As an example of this sign dependence, if the electrodes make contact with the left and right ends of the molecule in Figure 3-1e, then QI is controlled by the signs of the HOMO and LUMO at each end of the molecule. The LUMO in Figure 3-1e has a positive amplitude on the left (corresponding to the colour yellow) and a negative amplitude on the right (corresponding to the colour blue). Hence the product of the left and right

amplitudes (which I denote a_L) is negative. On the other hand, the HOMO in Figure 3-1e has a positive amplitude on the left (corresponding to the colour yellow) and a positive amplitude on the right. Hence the product of the left and right amplitudes (which I denote a_H) is positive. As discussed in [49][50], if the orbital products a_L and a_H have the opposite signs (as in Figure 3-1e), then they interfere constructively and when they have the same signs, they interfere destructively. Constructive quantum interference (CQI) leads to relatively high electrical conductance, whereas destructive quantum interference (DQI) leads to relatively low electrical conductance. Hence when electrodes are attached to the ends of the molecule in Figure 3-1e, one anticipates a relatively high electrical conductance. The fact that LUMO and HOMO orbital products corresponding to contacts at the ends of such molecules are of opposite sign is a consequence of orthogonality, because if the nodal structure of the LUMO and HOMO are the same in the direction transverse to their long axis, then orthogonality requires that the number of sign changes encountered along their long axis must differ by unity. Therefore CQI is expected to be a common feature of end-contacted molecules. A counterintuitive consequence of this QI feature is that if one electrode is placed at the left end of a molecule and the other electrode makes successive contacts along the length of a molecule, then as the spacing L between the electrodes increases, the conductance measured at the largest value of L should lie above the trend defined by equation (1). This feature is illustrated by the simple Huckel model shown in Figure 3-1a, whose HOMO and LUMO are shown in Figure 3-1c. If the left electrode is fixed at site 1 and the right electrode is placed on successive sites, L = 2, 3, ……8, then as shown in Figure 3-1d, the electoral conductance G_8 at the largest value of $L = 8$, is

higher than the conductance G_7 corresponding to the shorter length $L = 7$. Figure 3-1b shows the transmission function for this simple model. Clearly, if contact is made with successive sites, then quantum oscillations can occur over a wide range of electron energies E within the HOMO-LUMO gap. On the other hand, as indicated in Figure 3-6c, a more appropriate model for contacting perovskite clusters involves successive contacts with odd numbered sites (sites R1, R2 and R3 in Figure 3-6c, and following the black arrows in Figure 3-1d) , followed by a conductance jump at the final contact (site R4 in Figure 3-6c; red arrow in Figure 3-1d). In other words, quantum oscillations are likely to be absent, but QI would be signaled by a conductance jump at largest contact separation. For comparison, Figure 3-1f shows the transmission functions obtained from density functional theory for the short and long perovskite junctions of Figure 3-1e and again reveals counterintuitively that the conductance of the latter is higher than that of the former over a wide energy range.

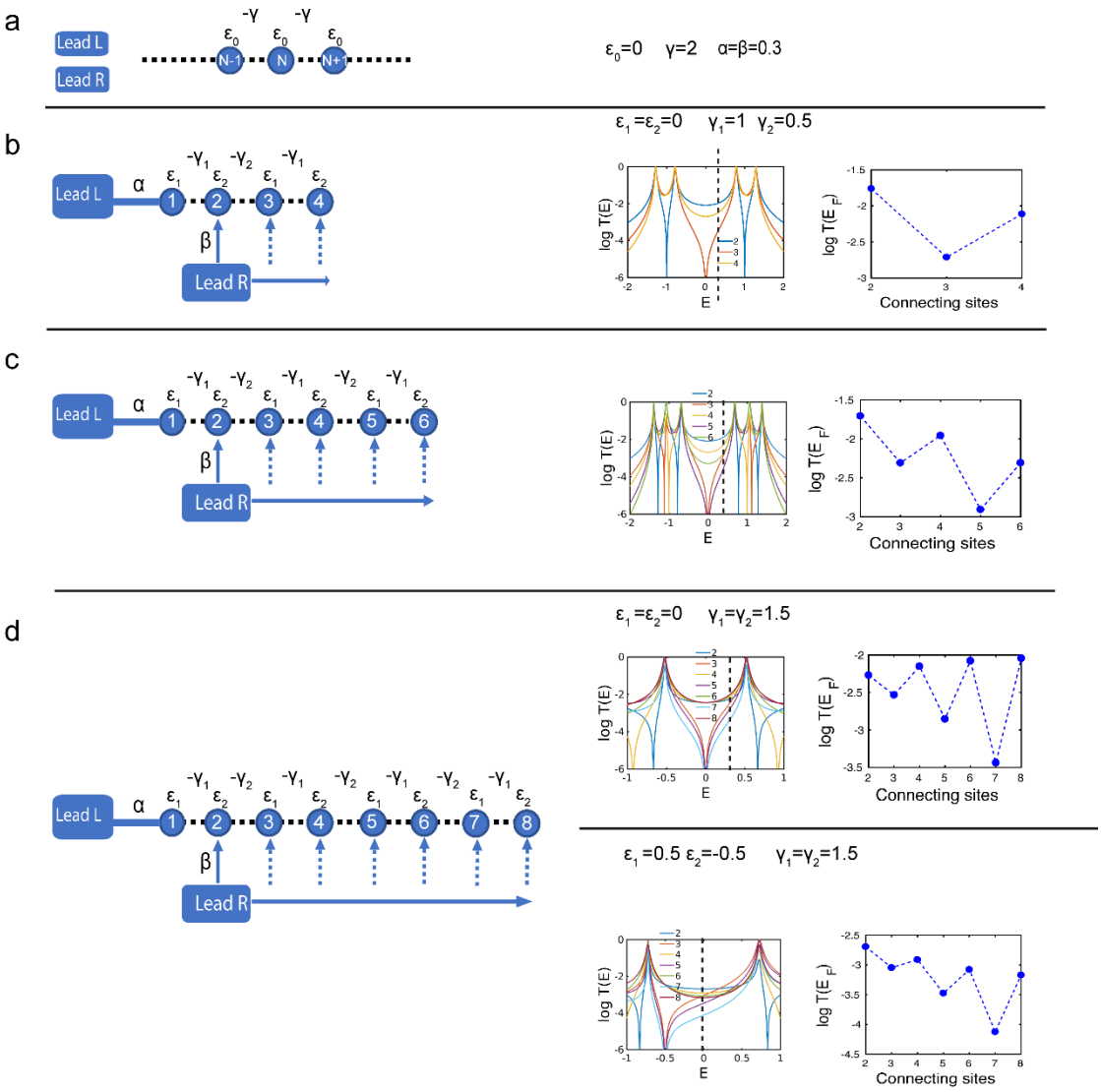

Figure 3-2 The tight binding model. a, The schematic of the uniform left and right lead parameter used in our simulations. b, The schematic of model with 4 sites diatomic chain. Site 1 is connected to Lead L, sites 2-4 are connected to Lead R sequentially. On the right side, the corresponding transmission spectra and the T(E_F) are plotted. The Fermi energy chosen is indicated by the dashed line. c, the schematic of model with 6 sites diatomic chain. Site 1 is connected to Lead L, sites 2-6 are connected to Lead R sequentially. On the right side, the corresponding transmission spectra and the T(E_F) are plotted. The Fermi energy chosen is indicated by the dashed line. d, the schematic of model with 8 sites diatomic chain. Site 1 is connected to Lead L, sites 2-8 are connected to Lead R sequentially. On the right side, the corresponding transmission spectra and the T(E_F) are plotted. The Fermi energy chosen is indicated by the dashed line. Different from the case I

discussed in Figure 3-1, where the ε is same while the γ is different, two cases are discussed here, 1- both the ε and γ are same. 2- the γ is same while the ε is different. With all the cases here, I demonstrate the jump behavior in the final point is generic.

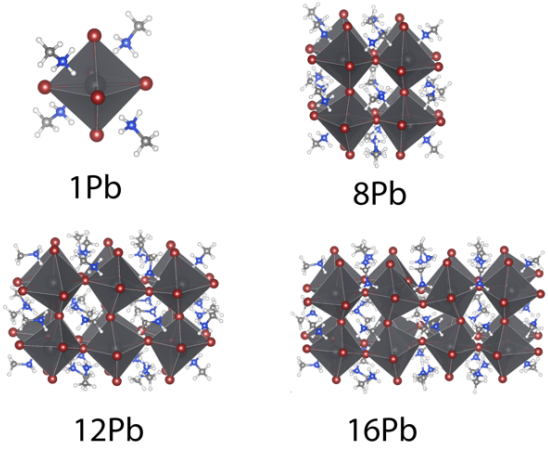

Figure 3-3 The relaxed conformations for neutral 1Pb, 8Pb, 12Pb and 16Pb $MAPbBr_3$ clusters. For 1Pb (MA_4PbBr_6), 8Pb ($MA_{20}Pb_8Br_{36}$) and 12Pb ($MA_{28}Pb_{12}Br_{52}$), I use the lowest energy coordinates in the literature[51] and then relaxed these structures using SIESTA. I constructed 16Pb ($MA_{36}Pb_{16}Br_{68}$) by adding another four octahedron units based on the 12Pb, and then relaxed.

The above analysis suggests that perovskite quantum clusters provide an ideal playground for identifying room-temperature QI transport features at the Ångstrom scale (also see Figure 3-2 for 4 and 6 sites models). Therefore I now provide an investigation of transport through perovskite clusters by combining using MCBJ experiments with DFT calculations. The experiments were carried out by our collaborators in Xiamen University.

3.2 Results and discussions

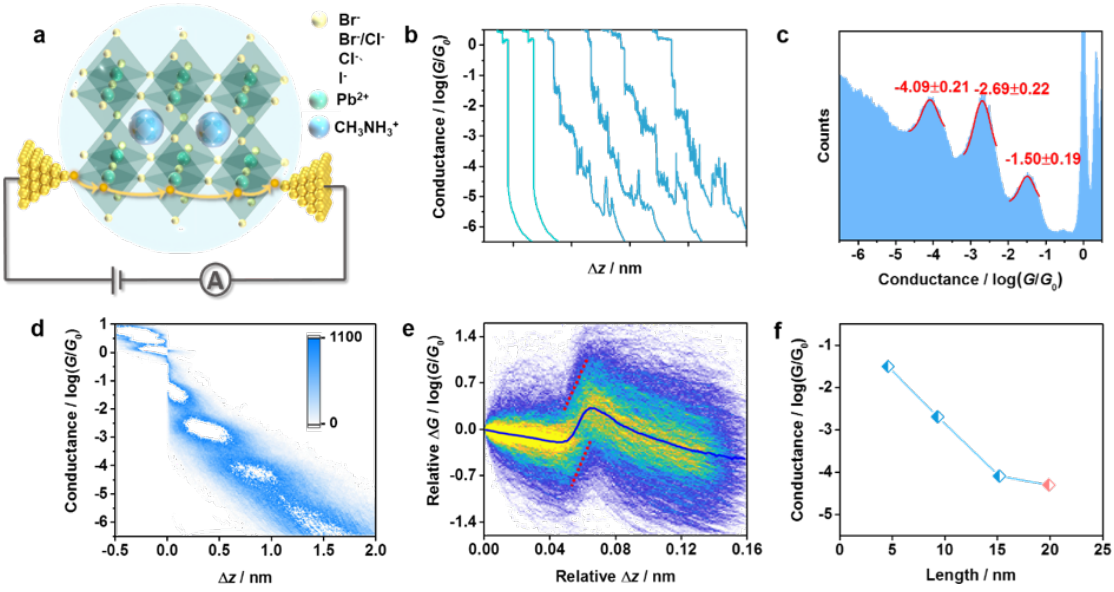

Figure 3-4 MCBJ single-molecule experimental results of $MAPbBr_3$ QDs. a, Schematic of MCBJ experimental principle in $MAPbX_3$ QDs. (MA= $CH_3NH_3^+$, X=I^-, Br^-, Cl^-, mixture of Br^- and Cl^-.) The yellow arrows indicate the sliding process of the gold electrodes during the MCBJ measurements. b, Typical individual conductance-distance traces of pure solvent (green) and $MAPbBr_3$ QDs (blue). c, 1D Conductance histograms of $MAPbBr_3$ QDs constructed without data selection (over 3500 traces). d, All-data-point 2D conductance versus relative distance (Δz) histogram of $MAPbBr_3$ QDs. e, 2D relative conductance (ΔG) verse relative displacement (Δz) histogram of the "jump curves" (over 2900 traces). f, The *I-V* characteristic curves of $MAPbBr_3$ QDs determined from conductance histograms at bias voltages ranges from 50mV to 250mV.

The experimental team investigated electron transport through single-QD junctions bonded to two gold electrodes through Au-halogen bonds. Four types of organic-inorganic halide perovskite perovskite QDs $MAPbX_3$ (MA= $CH_3NH_3^+$, X=I^-, Br^-, Cl^-, mixture of Br^- and Cl^-) were synthesized with oleic acid and octylamine as

ligands to enhance colloidal stability and suppress QD aggregation effects.[52] As shown in Figure 3-4a, the typical ABX_3 perovskite-type structure was composed of the framework of $[PbI_6]^-$ octahedra occupied by methylammonium cation (MA^+) in the four octahedra central positions. Single-QD conductance measurements of **$MAPbBr_3$** were carried out using the MCBJ technique in a solution containing 0.365 mg/mL QDs in a solvent of 1, 3, 5-trimethylbenzene (TMB) [53][54]. As shown in Figure 3-4b, the individual conductance-distance traces of pure solvent (green curves) without QDs showed a monotonic exponential decay after the rupture of gold-gold atomic contact at conductance quantum G_0 (where G_0 is the conductance quantum, which equals $2e^2/h$), while three distinguished conductance plateaus appeared in the traces of **$MAPbBr_3$** (blue curves). The corresponding 1D conductance histogram of **$MAPbBr_3$** (Figure 3-4c) shows that pronounced conductance peaks are located at $10^{-1.50}$ (P1), $10^{-2.69}$ (P2) and $10^{-4.09}$ (P3) G_0, respectively. The 2D conductance-displacement histogram is plotted in Figure 3-4d, and shows multiple distinct conductance clouds, indicating a high molecular junction formation probability and uniform charge transport properties of each configurations.

They also characterized the bias-voltage dependence of single-QD conductance over the range 50 mV to 250 mV. It was found that the current gradually increased and the current-voltage exhibited a linear relation, which corresponded well with the Simmons model of *I-V* characteristics at low bias voltage, suggesting that charge transport is mediated by an off-resonant coherent tunneling mechanism. While the bias voltage increased beyond 300 mV, the single-QD junctions, however,

became quite unstable and the conductance values were difficult to identify, which may be due to the destruction of the perovskite clusters at such high electric fields.

Interestingly, they observed a clear conductance jump at the end of the third plateau in ~70% of the individual conductance-distance traces of **$MAPbBr_3$** QDs. To express the jump in conductance more clearly, they refer to the treatment of 2D relative force vs relative displacement histograms using conductive atomic force microscope (AFM) technique.[55] As shown in Figure 3-4e, the 2D relative conductance (ΔG) versus relative displacement (Δz) histogram was constructed from the digitized conductance data after the third conductance plateau. Each data point was set at a new zero-relative conductance position along the conductance coordinate (y-axis) and generated to 2D histogram without further analysis. A clear jump in conductance could be observed at the relative displacement of ~0.04nm, confirming that the single-QD junction exhibited higher conductive state at the end of the sliding process of the two gold electrodes on the QDs.

To further reveal the possible binding geometries of the single QD junctions, they measured the single-molecule conductance of all ligands used in the synthesis of the QDs including oleic acid, octylamine, $PbBr_2$, $PbCl_2$, MACl and MABr. However, no conductance plateaus were observed, suggesting that the ligands did not provide the binding sites. Previous studies revealed that hydrogen bonding [Br...H-N+] bridged the lattice and ligand on the surface of perovskite QDs, indicating that only halogen was exposed to the outside of the quantum dots and had an opportunity to interact with the gold electrode.[56][57] Charge transport investigation of halogen-terminated single-molecule oligothiophene junctions also

suggested that Au-halogen interaction could act as a robust anchoring group for binding the molecule to the gold electrodes.[46] As for other atoms, the MA^+ were located at the center of the regular octahedron, which were impossible to connect to the gold electrodes, and the adjacent distance of the MA^+ was also not in accordance with the displacement distributions. The electronegativity of the Pb^{2+} was low, and the Pb^{2+} were hidden within the Br networks, so that they could not have provided a reliable interaction with the gold electrodes. Therefore, the gold electrodes could only interact with halogen, though Au-Br coordination by replacing the ligands, to form stable Au-QD-Au junctions.

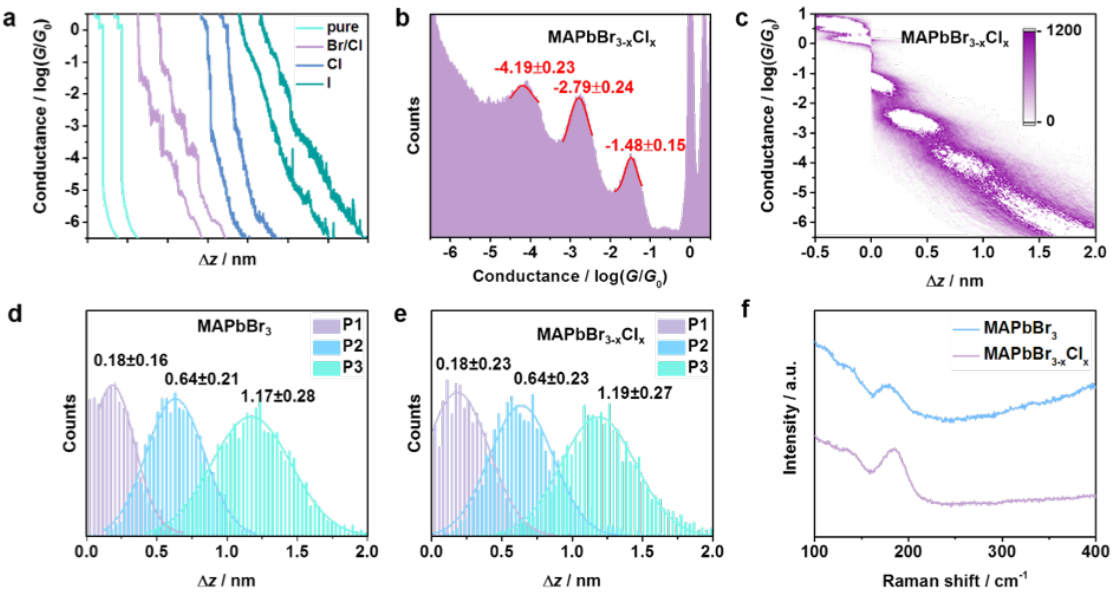

Figure 3-5 MCBJ conductance experimental results of $MAPbBr_{3-x}Cl_x$, $MAPbCl_3$ and $MAPbI_3$ QDs. a, Typical individual conductance-distance traces of pure solvent, $MAPbBr_{3-x}Cl_x$, $MAPbCl_3$ and $MAPbI_3$. b, 1D Conductance histogram constructed without data selection for $MAPbBr_{3-x}Cl_x$. The conductance-distance traces were recorded over 3500 traces. c, All-data-point 2D conductance versus relative distance (Δz) histogram for $MAPbBr_{3-x}Cl_x$. d, The displacement distributions of three plateaus for $MAPbBr_3$. e, The displacement distributions of three plateaus for $MAPbBr_{3-x}Cl_x$. f, Raman spectra of Au-Br interaction on the gold substrate with SHINERS nanoparticles.

To further validate the binding hypothesis, they carried out the single-QD conductance measurements of $\mathbf{MAPbBr_{3-x}Cl_x}$, $\mathbf{MAPbCl_3}$ and $\mathbf{MAPbI_3}$ QDs. Figure 3-5a showed typical individual conductance-distance traces of pure solvent and these three QDs. For $\mathbf{MAPbBr_{3-x}Cl_x}$, multiple conductance features were also observed, which were similar to those of $\mathbf{MAPbBr_3}$. The 1D and 2D conductance histograms of $\mathbf{MAPbBr_{3-x}Cl_x}$ also showed three conductance features located at $10^{-1.48}$, $10^{-2.79}$ and $10^{-4.19}$ G_0, respectively, and the trend of *I-V* characteristic curves was also similar with that of $\mathbf{MAPbBr_3}$, suggesting the binding of $\mathbf{MAPbBr_{3-x}Cl_x}$ also came from the Au-Br coordination. they also constructed the conductance histogram for $\mathbf{MAPbCl_3}$ and $\mathbf{MAPbI_3}$ from ~3000 individual traces, and no conductance peaks was observed, while the peak of gold-gold atomic junction at G_0 for $\mathbf{MAPbI_3}$ became less clear than others. Furthermore, we calculated the Au-halogen binding energy by using DFT and found that the Au-halogen binding energy was in accordance with the order of Au-I > Au-Br > Au-Cl. The comparison of different QDs suggested that for $\mathbf{MAPbCl_3}$ QDs, the bond energy of Au-Cl bond was too weak to form stable Au-QD-Au junctions. In contrast, the strong Au-I bond may break the crystal structure of $\mathbf{MAPbI_3}$ with the stretching of the electrode.

To reveal the binding configurations of the multiple conductance features, they analyzed the relative displacement distribution of $\mathbf{MAPbBr_3}$ and $\mathbf{MAPbBr_{3-x}Cl_x}$ QDs. As shown in Figure 3-5d and e, for $\mathbf{MAPbBr_3}$ QDs, the most probable displacements of each conductance features were 0.18±0.16 nm, 0.64±0.21 nm and 1.17±0.28 nm, respectively, while the most probable displacements were 0.18±0.23 nm, 0.64±0.23 nm and 1.19±0.27 nm for $\mathbf{MAPbBr_{3-x}Cl_x}$ QDs. The average displacement differences were determined to be ~0.5 nm from the difference of the above

values, which were quite similar for both QDs. The difference of adjacent statistical lengths was approximately consistent with the adjacent lattice distance of Br, confirming that it was the Au-Br coordination provided the binding sites for Au-QD-Au junctions, during the sliding of gold electrode across the QD's surface. To provide direct evidence of the Au-Br bond, they further performed the shell-isolated nanoparticle-enhanced Raman spectroscopy (SHINERS) that 3.65 mM perovskite QDs were dropped on the evaporated gold films and then the as-prepared shell-isolated gold nanoparticles were added for Raman enhancement. As shown in Figure 3-5, two distinct Raman peaks could be observed at ~180 cm^{-1} in $MAPbBr_3$ and $MAPbBr_{3-x}Cl_x$, which confirmed the formation of Au-Br bond. [58], [59]

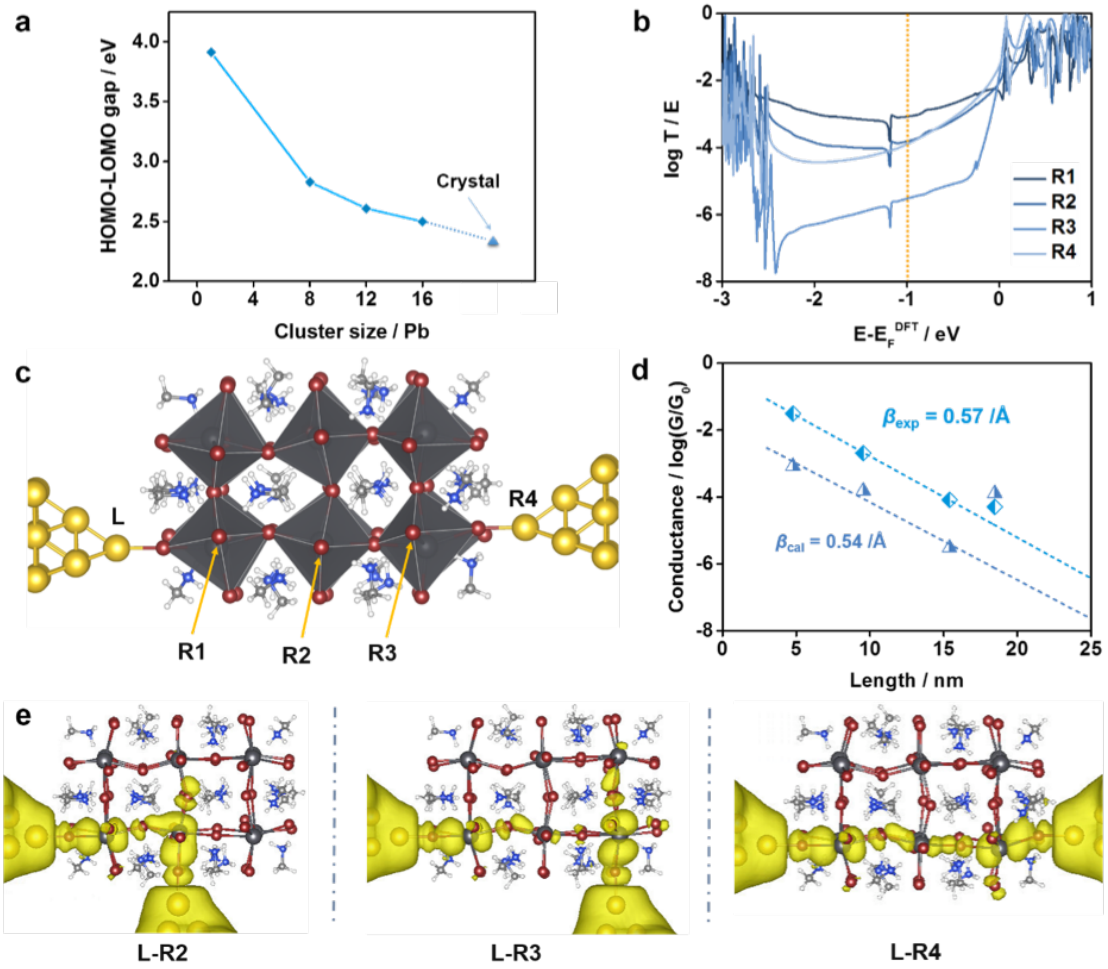

Figure 3-6 The charge transport property of 12Pb $MAPbBr_3$ with different connectivities. a, HOMO-LUMO gaps with respect to the size of $MAPbBr_3$ clusters. b, The transmission spectra of different connectivities as the function of $E - E_F^{DFT}$. c, Relaxed conformation for a 12Pb $MAPbBr_3$ cluster attached to two gold electrodes, where Pb, Br, N, C, H and Au atoms are depicted in large gray, purple, blue, small gray, white and yellow balls, respectively. The Br atoms connected to gold electrode are indicated by the orange arrows. The Br atom connected to left lead is labelled as 'L', while the Br atoms attached to right lead are labelled 'R1', 'R2', 'R3' and 'R4'. d, The corresponding conductance evolution versus the increasing separation between the two electrodes. The blue dots stand for the room temperature conductance derived from the transmission spectra in (b) at -1 eV while the corresponding dashed lines show the corresponding linear fit to $\ln G = -\beta L + constant$ where L is the separation between two Br atoms. For comparison, the experimental results are plotted as black dots fitted by a black

dash line. The conductance of 'L-R4' is shown by the blue diamond. e, The LDOS with yellow color in the energy window from –1.5 eV to -0.5 eV for 'L-R2' 'L-R3' and 'L-R4' separately at the isosurface 0.00008.

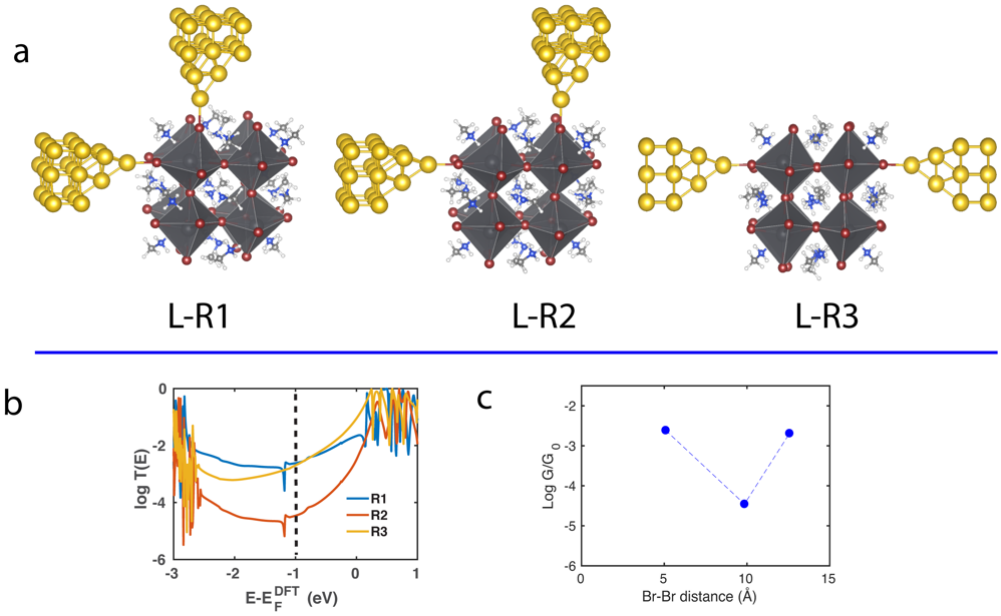

Figure 3-7 The DFT theoretical calculation of 8Pb $MAPbBr_3$ cluster. a, The conformations for 8Pb $MAPbBr_3$ cluster embedded in two gold electrodes with 3 different connectivity L-R1, L-R2 and L-R3. b, The corresponding transmission spectra. c, The room temperature conductance with the E_F=-1 eV as indicated by the black dashed line in b.

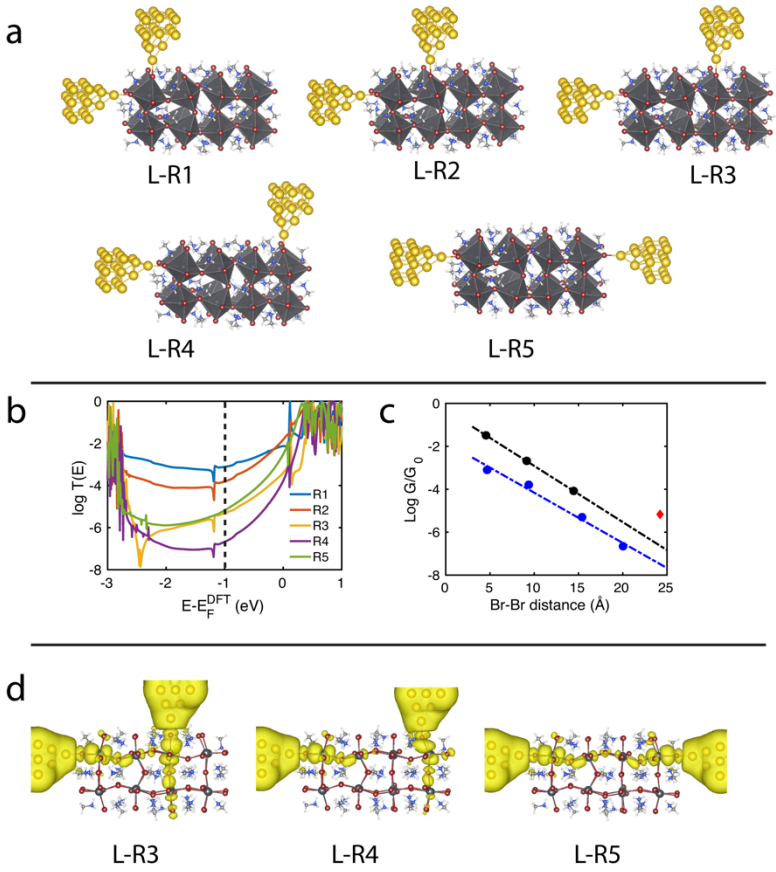

Figure 3-8 The DFT theoretical calculation of 16Pb $MAPbBr_3$ cluster. a, The conformations for 16Pb $MAPbBr_3$ cluster embedded in junctions with 5 different connectivity L-R1, L-R2, L-R3, L-R4 and L-R5. b, The corresponding transmission spectra. c, The room temperature conductance versus their distances with the E_F=-1 eV as indicated by the black dashed line in b, the experimental results also put here for comparison. The jump conformation L-R5 is indicated by the red diamond. d, The LDOS with yellow color in the energy window from –1.5 eV to -0.5 eV for 'L-R3' 'L-R4' and 'L-R5' separately at the isosurface 0.00004.

In order to gain further insight into the conductance trends observed in the MCBJ measurements, transmission spectra *T(E)* were calculated by combining the DFT package SIESTA[60] with the quantum transport code Gollum[61]. Initially I modelled the minimal unit of a single octahedron. Since the fringe halide ions in a

perovskite lattice are known to be coordinated by the ligands of oleate acid and n-octylamine, the **$MAPbBr_3$** neutral charge clusters (1Pb (MA_4PbBr_6), 8Pb ($MA_{20}Pb_8Br_{36}$), 12Pb ($MA_{28}Pb_{12}Br_{52}$), 16Pb ($MA_{36}Pb_{16}Br_{68}$)) were built with the same method as the literature.[51] as shown in Figure 3-3. For the crystal **$MAPbBr_3$**, our calculated band gap of 2.31 eV agrees well with the experimental value 2.24 eV,[62] which is plotted in Figure 3-6a, along with the HOMO-LUMO gaps of $MAPbBr_3$ clusters of different sizes. As the size of the clusters decreases, their HOMO-LUMO gaps increase to 2.5 eV (for 16Pb) and further to 3.91 eV (for 1Pb) due to the stronger quantum confinement effect. In the current study, the fully relaxed 12Pb **$MAPbBr_3$** cluster was connected to two gold electrodes through two Br atoms as shown in Figure 3-6c, where the Br atom labeled by 'L' was attached to left gold electrode, the right gold electrode was attached successively to Br atoms labeled by 'R1', 'R2', 'R3' and 'R4' to model a pulling process. The corresponding transmission spectra are plotted in Figure 3-6b, as Br atom contacting the right gold electrode is changed from 'R1' to 'R4', the conductance decreases due to the increasing length L between the two electrodes. As expected, when the Fermi energy is located within the HOMO-LUMO gap, charge transfer takes place via off-resonant tunneling and the conductance decays exponentially with L. After fitting the natural logarithm of the room-temperature conductance (E_F=-1.0 eV) to a linear function, an attenuation factor of $\beta = 0.54/\text{Å}$ was obtained, which is consistent with our measured value of $0.57/\text{Å}$, as shown in Figure 3-6d. The β value of perovskite QDs junctions is higher than oligothiophenes,[63] oligo(p-phenylene ethynylene)s[64] and diketopyrrolopyrrole oligomers.[65] More interestingly, in agreement with our experiments and the discussion above

Figure 3-4, when the right electrode is moved from 'R3' to the furthest distance 'R4', I obtain a much higher conductance compared with the shorter path 'R3' as shown in Figure 3-6b (the green curve) and red (the last red diamond point). This increase is also reflected in the qualitative behaviour of the local density of states (LDOS) for 'L-R2', 'L-R3'and 'L-R4' as shown by yellow surfaces in Figure 3-6e. In contrast with R3, the weights of LDOS extend almost continuously between the left electrode and R4. This increase at the most distant electrode separation is also found in 1Pb, 8Pb and 16Pb $MAPbBr_3$ clusters as shown in Figure 3-1, Figure 3-7, Figure 3-8. Other possible connectivities for 16Pb $MaPbBr_3$ cluster were also explored, I find this jump behavior is generic although different β factors are observed (0.72/Å and 1.2/Å seperately), as shown in Figure 3-9 and Figure 3-10, the latter is larger due to the higher energy barrier which makes it less likely to appear in experiment.

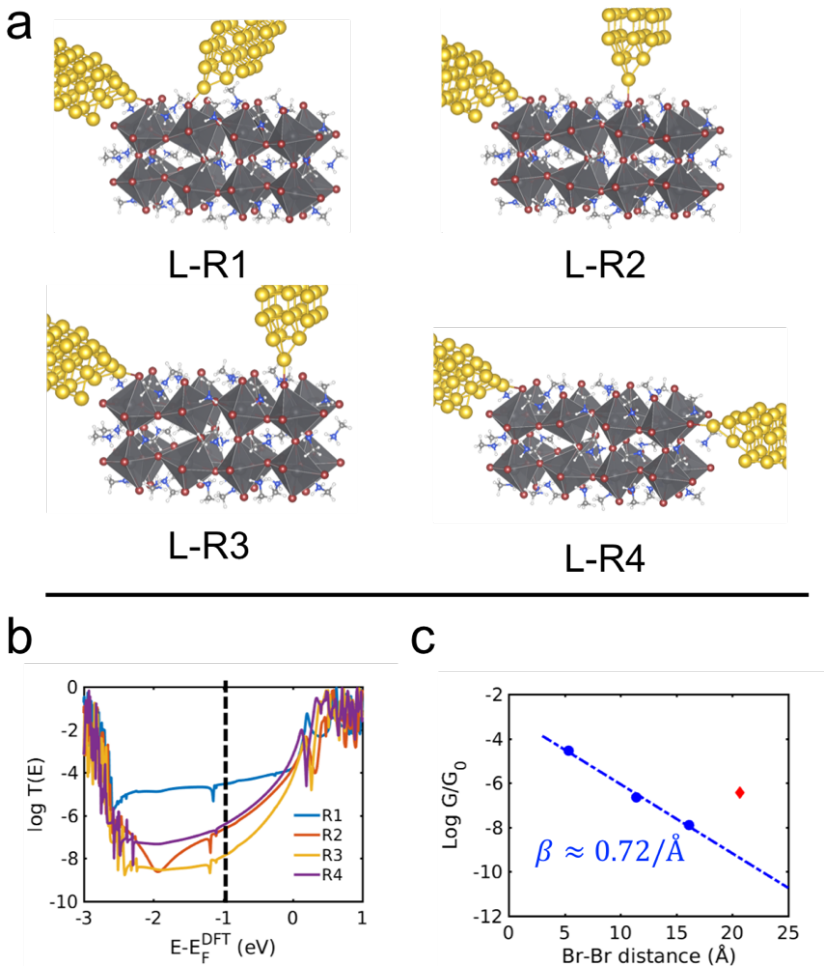

Figure 3-9 The DFT theoretical calculation of 16Pb $MAPbBr_3$ cluster with left lead connecting to another Br atom. a, The conformations for 16Pb $MAPbBr_3$ cluster embedded in junctions with 4 different connectivity L-R1, L-R2, L-R3, L-R4. b, The corresponding transmission spectra. c, The room temperature conductance versus their distances with the E_F=-1 eV as indicated by the black dashed line in b. The jump conformation L-R4 is indicated by the red diamond.

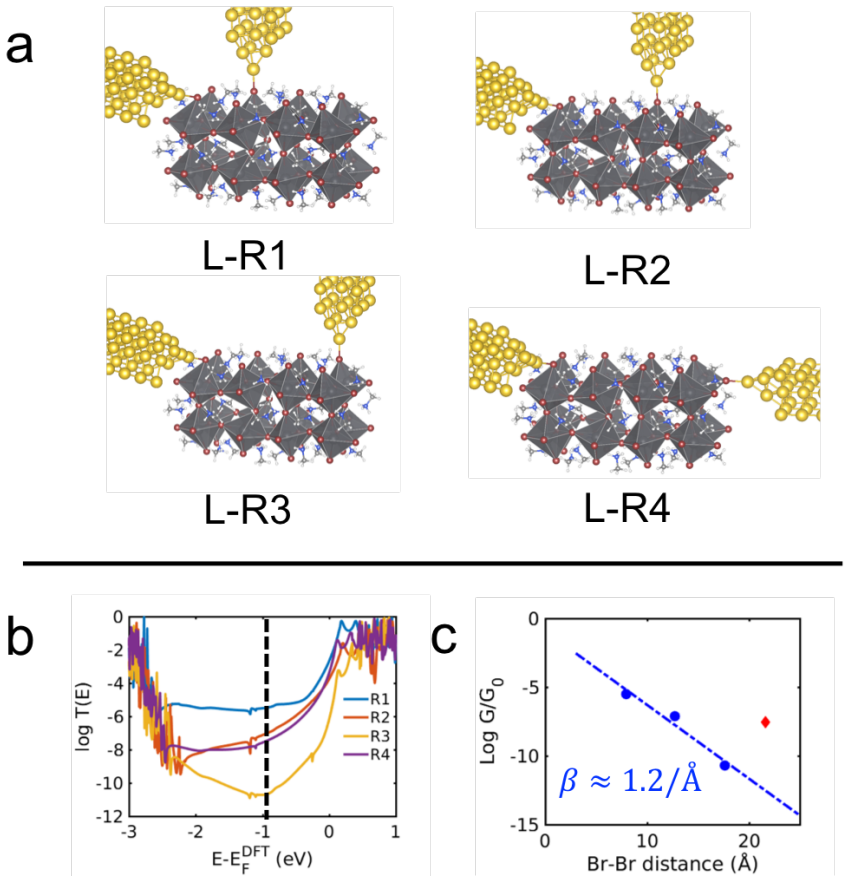

Figure 3-10 The DFT theoretical calculation of 16Pb $MAPbBr_3$ cluster with left lead connecting to another Br atom with a cross plane manner. a, The conformations for 16Pb $MAPbBr_3$ cluster embedded in junctions with 3 different connectivity L-R1, L-R2, L-R3 and L-R4. b, The corresponding transmission spectra. c, The room temperature conductance versus their distances with the E_F=-1 eV as indicated by the black dashed line in b. A larger β factor is obtained due to the higher energy barrier and the jump conformation L-R4 is indicated by the red diamond.

3.3 Conclusion

In summary, I have presented the theoretical investigation into some interesting experimental results of room-temperature QI effects in the electrical conductance of single perovskite QD junctions. Three distinct conductance features are

observed from the conductance measurement of perovskite QDs with Br, while the QDs with I and Cl show no significant features. The analysis of conductance trends with displacement reveals that the multiple conductance features are derived from the sliding of gold electrodes between the adjacent Br atoms in different unit cells. Counterintuitively, There is a distinct conductance jump at the end of individual conductance traces, which is direct evidence of a room-temperature QI effect. This work offers new insight into QI effects in perovskite materials at the single-unit-cell level, and offers an opportunity to explore new strategies for optimising electron transport in perovskite QDs electronic and photoelectric devices.

4 Unusual Length-Dependence of Conductance in Cumulene Molecular Wires

In this chapter, charge transport properties of cumulene wires are explored experimentally and theoretically. The experiments were carried out by colleagues in Oxford, Madrid and Liverpool Universities. Cumulenes are sometimes described as 'metallic' because an infinitely long cumulene would have the band structure of a metal. Here I report the single-molecule conductances of a series of cumulenes and cumulene analogues, where the number of consecutive C=C bonds in the core is $n = 1$, 2, 3 and 5. The [n]cumulenes with $n = 3$ and $n = 5$ have almost the same conductance, and they are both more conductive than the alkene ($n = 1$). This is remarkable because molecular conductance normally falls exponentially with length. The conductance of the allene ($n = 2$) is much lower, as expected from its

twisted structure. Computational simulations predict a similar trend to the experimental results and indicate that the low conductance of the allene is a general feature of [*n*]cumulenes where *n* is even. The lack of length-dependence in the conductances of [*n*]cumulenes where *n* is odd results from the strong decrease in HOMO-LUMO gap with increasing length.

4.1 Introduction

Long molecules generally conduct electricity less well than short ones, and this can be a problem when designing molecular wires for mediating efficient charge-transport over distances of several nanometers. When a homologous series of oligomers are connected between metal electrodes, and the transport mechanism is coherent tunneling, the conductance G of each oligomer typically decreases exponentially with its molecular length L according to equation (1),[66]

$$G \propto e^{-\beta L} \qquad (1)$$

where β is the exponential attenuation factor, which is normally in the range 0.2–0.5 $Å^{-1}$ for a conjugated organic π-system. [67]–[70] It has been predicted that molecules with low bond length alternation will give unusual attenuation factors, such a $\beta \approx 0$ (i.e. conductance independent of length) or even $\beta < 0$ (i.e. conductance increasing with length). [71], [72] Cumulenes are the simplest type of neutral π-system not to exhibit substantial bond length alternation. [73]–[75] Here the experimentalist and I report an experimental and computational investigation of the length-dependence of charge transport through these linear

carbon chains. Recently, length-independent conductances were reported for a set of cyanine dyes, which constitute a class of charged π-system without bond length alternation. [76] The positive charge on these cyanine makes it more difficult to compute their electronic structures, compared with the neutral cumulenes.

Figure 4-1 Cumulenes and polyynes: two types of linear *sp* carbon chains.

Cumulenes and polyynes are the two types of linear chains of sp-hybridized carbon atoms: in cumulenes, the carbon atoms are linked by double bonds, whereas in polyynes there are alternating single and triple bonds (Figure 4-1).[73], [74] Cumulenes and polyynes have fascinated chemists for many years as models for carbyne, the infinite 1D form of carbon.[74] Cumulenes are said to have a 'metallic' electronic structure, [72]–[75], [77] because an infinitely long cumulene would have a band structure characteristic of a metal, with a partially occupied band derived from the π and π* molecular orbitals. In contrast polyynes have a π-π* gap that persists even in long chains, and an infinite polyyne is expected to be a semiconductor. This difference in electronic structure is a direct consequence of the difference in bond length alternation. Although there is some bond length alternation in cumulenes,[75] the difference between the lengths of the C=C bonds in cumulene is much more subtle than the alternation between short C≡C and long C-C bonds in polyynes.

Here, I report a theoretical and experimental investigation of the conductances of the family of cumulenes 1, 2, 3 and 5 shown in Figure 4-2. I have included the [4]cumulene 4 in our theoretical investigation, but the experimentalistshave not yet tested it experimentally. All these molecules have terminal 4-thioanisole substituents for binding to gold electrodes. Single-molecule conductances were measured using the scanning tunneling microscopy break-junction (STM-BJ) method, using a gold tip and a gold surface, [15] as described in detail previously.[70]

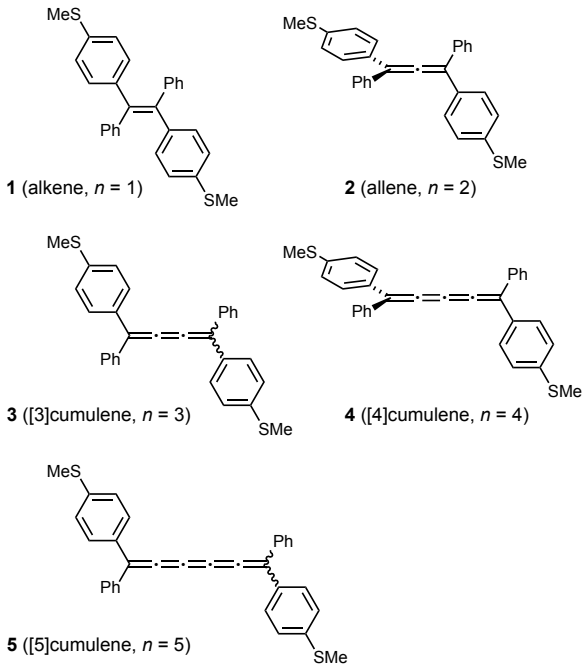

Figure 4-2 Structures of compounds 1–5. (Note that only 1, 2, 3 and 5 have been tested experimentally.)

Compounds 1, 2, 3 and 5 were synthesized as described in literature. [78] The alkene 1 was recrystallized to give a single isomer, which is probably E configuration, although this has yet to be confirmed, and the experimentalists expect the E and Z isomers to have very similar molecular conductances. Allene 2

is racemic meaning it has equal amounts of left- and right-handed enantiomers. Cumulenes 3 and 5 are mixtures of E and Z isomers (as confirmed by 1H NMR spectroscopy); we were unable to separate these stereoisomers and we expect them to convert readily under ambient conditions.[79]

4.2 Results and discussions

The experimental conductance results for compounds 1–3 and 5 are summarized in Figure 4-3 and Table 1. The 2D histograms (Figure 4-3a-d) show how the conductance (G/G_0, where $G_0 = 2e^2/h$) of each junction varies as the STM tip is retracted from the surface (increasing distance, z) for a large number of traces. All the compounds give well-defined plateaus, which become longer as the length of the molecule increases, indicating that the SMe groups connect across the Au-Au junction (see Table 1 for experimental and calculated molecular lengths, Lexp and Lcalc). The percentage of junctions that give a molecular plateau for each compound is given in the caption to Figure 4-3. Due to the fact that the conductance varies slightly with distance for the alkene and allene, the molecular conductances plotted in Figure 4-3g (and listed in Table 1) are quoted from the histograms in Figure 4-3f where we have considered only points from the end of the distribution, greater than the median length determined from a Gaussian fit. We demonstrated the value of this method previously for a family of porphyrins.[80] This analysis procedure ensures that the conductance values can be attributed to fully-stretched single-molecule junctions, and it also results in good overlap between histograms (of the same compound) from periods of

measurement with different percentages of molecular junctions. Often, we observe that when the percentage of molecular junctions is high, the conductance peak is higher (or weighted to higher values), normally when the percentage exceeds about 40%.[81] This phenomenon is attributed to the occurrence of junctions containing several molecules in parallel. However, if only the data points at longer plateau lengths are consider, the resulting histograms are more reproducible. This indicates that the probability of multiple-molecule junctions diminishes as the junctions are stretched.

The [3] and [5]cumulenes have essentially the same conductance, which is slightly larger than that of the alkene. The allene has a conductance that is about 50 times smaller than those of the [3] and [5]cumulenes, reflecting its twisted geometry. We have also investigated the voltage dependence of the conductance. All compounds tested showed a weak G(V) dependence. Junctions of [5]cumulene were stable generally to $\pm$ 1.2 V, whereas the shorter [2]cumulene was stable only to $\pm$ 0.5 V. These results suggest that the Fermi level lies far from any molecular levels, consistent with the Fermi level sitting towards the center of the HOMO-LUMO gaps. At 1.2 V, the maximum current through a [5]cumulene molecule approaches microamperes.

Table 1. Single-molecule conductances, lengths and HOMO-LUMO gaps for compounds **1**–**3** and **5**.

compound	$\log(G/G_0)$[a]	L_{exp} (nm)[b]	L_{calc} (nm)[c]	E_g(UV) (eV)[d]	E_g(DFT) (eV)[e]
1 ($n = 1$)	-4.09	0.94 (1.32)	1.45	3.7	2.21
2 ($n = 2$)	–5.25	1.01 (1.34)	1.47	4.2	2.74
3 ($n = 3$)	-3.74	1.07 (1.46)	1.63	2.7	1.54
5 ($n = 5$)	-3.64	1.09 (1.64)	1.80	2.4	1.24

[a] Experimental conductance peak positions from data in Figure 4-3f; Run to run variation in peak position is about 0.02. [b] Lengths are calibrated by adding 0.4 nm to the peak position of a Gaussian fit to the total distribution of plateau lengths. Values in brackets are derived from the 95th percentile. [c] Calculated using the Spartan quantum chemical package at the semi-empirical level. We bind a gold atom to each sulfur and measure the Au-Au distance. [d] HOMO-LUMO gap calculated from the peak wavelength of the lowest-energy absorption band in chloroform. [e] Calculated Kohn-Sham HOMO-LUMO gaps from DFT for isolated molecules in vacuum.

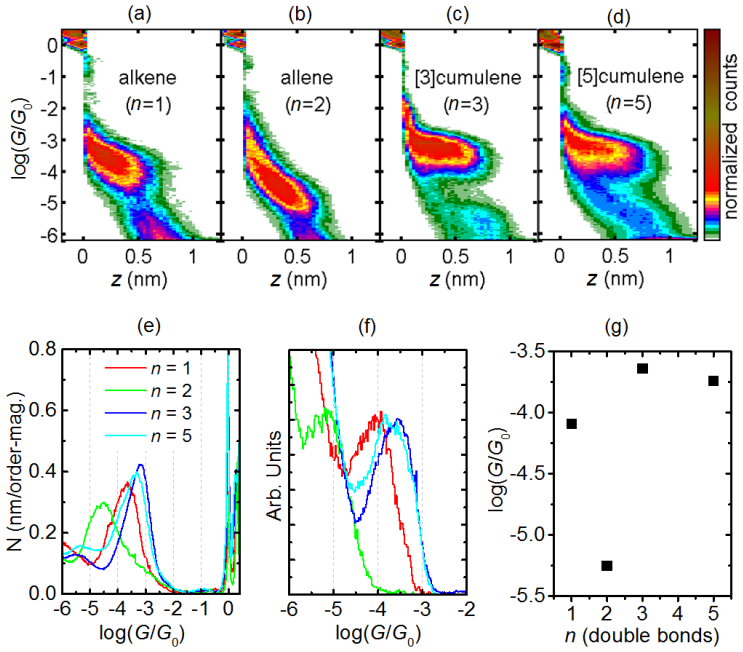

Figure 4-3 STM-BJ results on molecules 1–3 and 5 measured with a bias of 0.2 V. (a–d) 2D conductance histograms for the plateau-containing traces. The number of traces in each (and percentage of the total) are as follows: $n = 1$: 1309 (56%), $n = 2$: 2988 (58%), $n = 3$: 1139 (47%), $n = 5$: 3402 (34%). (e) 1D conductance histograms using all data points. (f) 1D conductance histogram using only points from the end of the plateau distribution (g) Molecular conductances from Gaussian fits to the data in (f). The errors in the fits are smaller than the size of the square symbols.

In order to gain further insight into the conductance trends in the family of cumulene molecular wires, and how their conductances change with length, transmission spectra *T(E)* were calculated by combining the DFT package SIESTA [82] and with the quantum transport code Gollum.[61] Since the cumulene wires have four phenyl rings, they are likely to be trapped in local energy minima during DFT relaxing process. Therefore, for alkene, [3]cumulene and [5]cumulene, two types of initial structures were used in which the two terminal thioanisole rings are initially planar or non-planar. The relaxed conformations as well as the

corresponding energies are shown in Figure 4-4(a) and (b) respectively, which indicating that those in panel b are the more energy favorable conformations (indicated by red square in Figure 4-4 (b)). For [2]cumulene and [4]cumulene, whether or not we choose the two terminal thioanisole rings to be planar or non-planar, after relaxation, I obtain molecules with the two terminal thioanisole rings perpendicular to each other due to the odd number of carbon atoms with two π electrons (*e.g.* The middle carbon atom for allene, the middle three carbon atoms for [4]cumulene).

Therefore, the structures in Figure 4-4(b) for alkene, [3]cumulene and [5]cumulene are used to understand the experimental results, since they are energy preferred conformations with two non planer terminal thioanisole rings as shown in Figure 4-4b (this is consistent with the experimental crystallographic results in literature)[83].

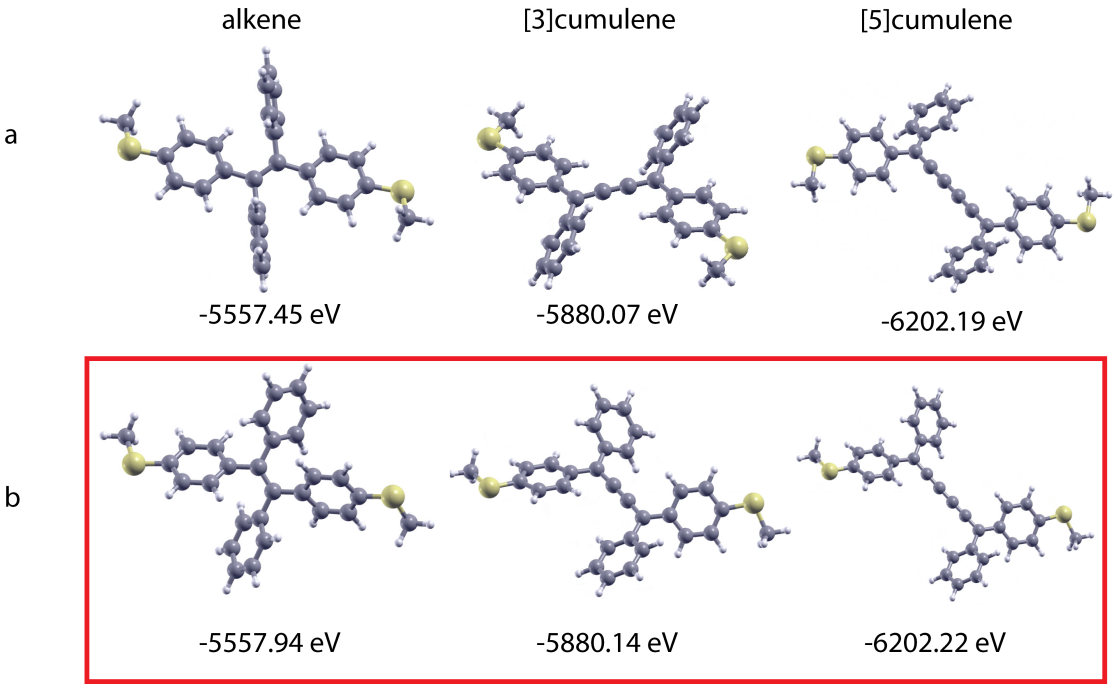

Figure 4-4 For alkene, [3]cumulene and [5]cumulene, the relaxed structures as well as the corresponding energy of two type of initial structures (a) the two terminal thioanisole rings are planar (b) the two terminal thioanisole rings are not planar. The conformations we chose for calculation in manuscript are indicated by red square.

The conformations of relaxed molecules embedded in Au-Au junctions are shown in Figure 4-6a. The frontier molecular orbitals (Figure 4-5) show that the HOMO of alkene, the HOMO and LUMO of [3]cumulene and [5]cumulene form extended π-conjugated transport paths through the whole molecule. In contrast, the molecular orbitals of the allene and [4]cumulene are formed from pz and px orbitals and follow chiral paths through the molecules, leading to terminal thioanisole rings which are orthogonal to each other, and the absence of an extended π-system in the HOMO and LUMO. As shown in Figure 4-6b, these differences between the even and odd-numbered cumulenes are reflected in their transmission functions. Over a range of E_F within the HOMO-LUMO gap, (indicated by the shaded region in Figure 4-6b), the conductances of allene and the [4]cumulene are expected to be lower than those of the other three molecules. More interestingly, the conductances of the [3]cumulene and the [5]cumulene are predicted to be about the same, despite the substantial change in length. The alkene has a slightly lower conductance than both [3]cumulene and [5]cumulene, due to the larger angle between its two terminal thioanisole rings, which is the result of steric interactions between the thioanisole and phenyl substituents. This prediction is consistent with previous computational studies of charge transport through cumulene molecular wires. The local density of states (LDOS) of alkene

and allene (Figure 4-6c) reveals a clear transport path for the alkene, while there is nearly no weight (magenta surface) on the allene molecule.

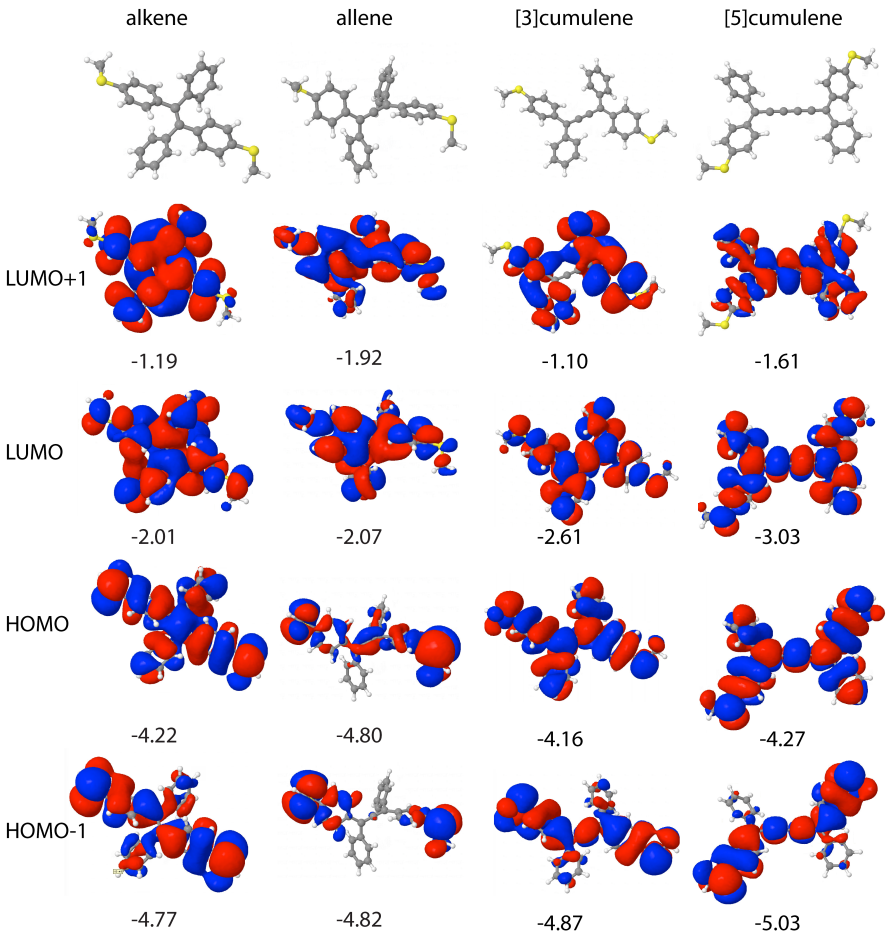

Figure 4-5 The frontier molecular orbitals HOMO-1, HOMO, LUMO and LUMO+1 of isolated molecules of alkene, allene, [3]cumulene and [5]cumulene as well as the corresponding energy eigenvalues (in eV).

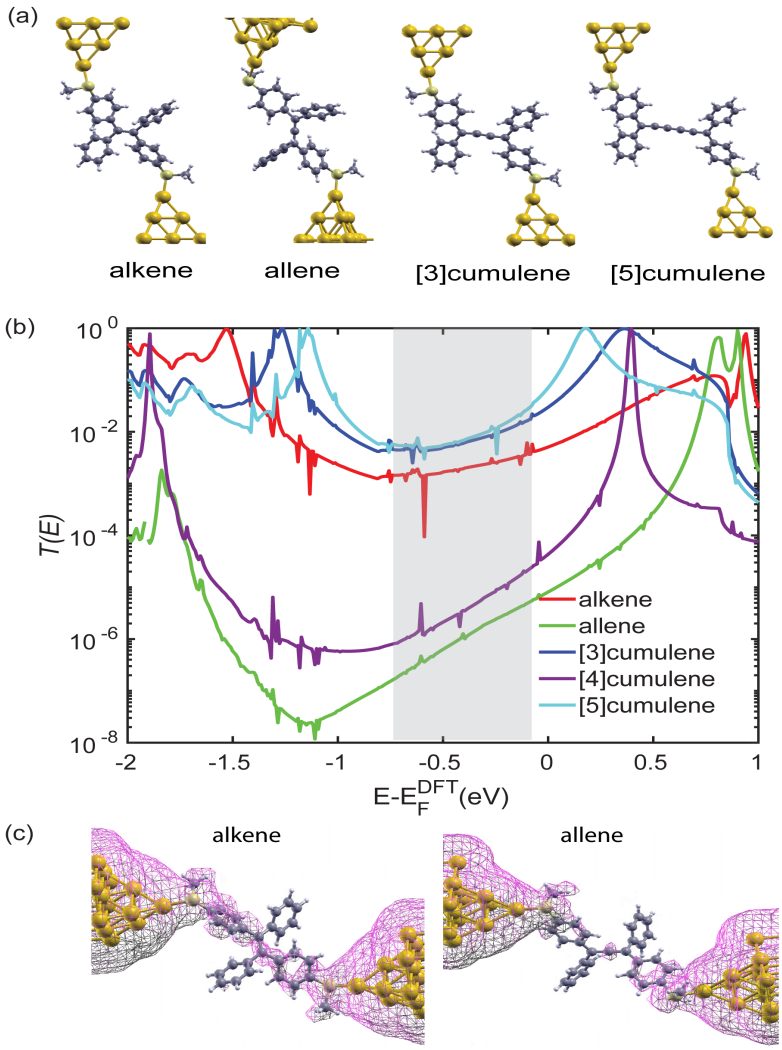

Figure 4-6 (a) Calculated conformations for alkene, allene, [3]cumulene, [5]cumulene attached to two gold leads, where the grey, white and pale yellow balls represent carbon, hydrogen and sulfur respectively. The yellow balls at both ends represent gold leads. (b) Transmission spectra. The shaded region indicates the range of Fermi energies within the HOMO-LUMO gap that contribute towards conduction at room temperature. (c) the LDOS with magenta color in the energy window from -0.5 eV to 0 eV for alkene and allene incorporated in two gold leads separately at the isosurface 0.00002.

The experimental conductances of molecules 1, 2, 3 and 5 correlate well with their HOMO-LUMO gaps, as illustrated by the optical gaps, Eg(UV) calculated from the wavelength of the lowest-energy UV-vis absorption band, and the Kohn-Sham

gaps, Eg(DFT) in Table 1. [84] The lack of attenuation in the conductance ($\beta \approx 0$) for the series of compounds alkene, [3]cumulene and [5]cumulene can be attributed to the decreasing HOMO-LUMO gaps of these molecules, which compensate for their increasing length. [15],[85] The lower molecular conductance of the allene is consistent with the large HOMO-LUMO gap which leads to a higher energy barrier for electron transport. Conductance oscillations have also been observed for various chains of single metal atoms (e.g. Au, Pt and Ir) as a function of the number of atoms in the chain.[86], [87] For chains with single conductance channels (Au and Na) this 'odd-even' effect has been suggested to originate from quantum interference, where odd-numbered chains conduct with $G = G_0$, while even-numbered chains have a conductance less than G_0. [88],[89] As Pt and Ir have more than one contributing conductance channel, this behavior is expected to be a universal feature of monoatomic chains. Cumulenes, as monoatomic chains of carbon atoms, appear to behave similarly. Notable differences, however, between our measurements and those of metal chains are that the chain and electrode atoms differ, producing an energy offset between the molecular bridge and the electrodes and there are 4-thioanisole anchor groups separating the chains and leads, which are only π-conjugated in the odd [n]cumulenes (i.e. even number of carbon atoms).

In the following part, for alkene, [3]cumulene, [5]cumulene, the conformations with terminal anisole rings coplanar as shown in Figure 4-7a are used to explore the conductance dependent only on the increasing length since the angles are same between the two terminal thioanisoles. The results as shown in Figure 4-7 demenstrating that removing this steric effect would be expected to make the

difference in conductance between the alkene, the [3]cumulene and the [5]cumulene even smaller compared with the results in Figure 4-6. This reinforces our main point: that the conductances of these three compounds are almost the same.

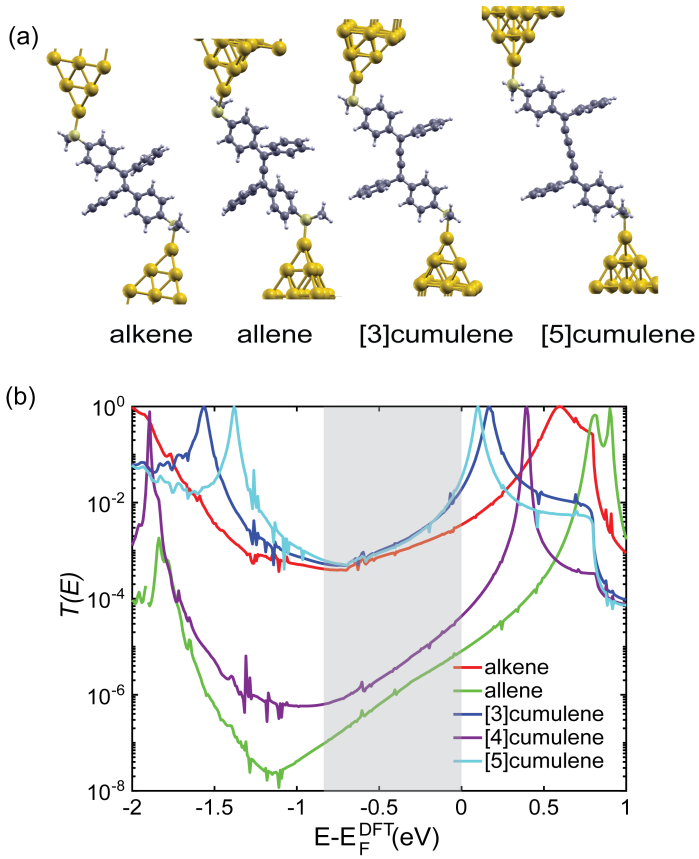

Figure 4-7 (a) Calculated conformations for alkene, allene, [3]cumulene, [5]cumulene attached to two gold leads with the thioanisole rings coplanar (grey, white and pale yellow balls represent carbon, hydrogen and sulfur, respectively). The yellow balls at both ends represent gold leads. (b) Transmission spectra. The shaded region indicates the range of Fermi energies within the HOMO-LUMO gap that contribute towards conduction at room temperature. For alkene, [3]cumulene and [5]cumulene, the conformations in (a) are used.

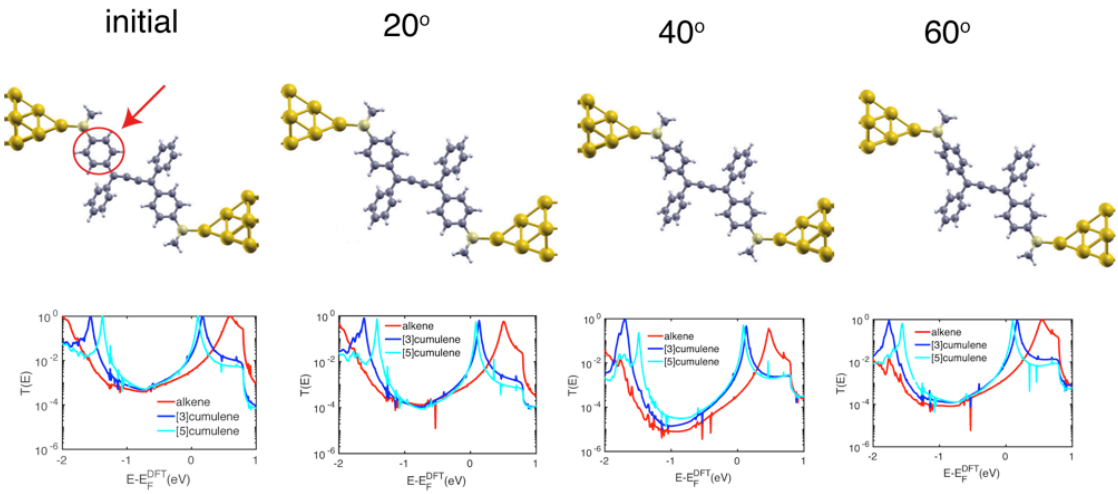

Figure 4-8 Transmission function *versus* the orientation of one of the two terminal phenyl rings relative to the other terminated phenyl ring for alkene, [3]cumulene and [5]cumulene. The red arrow indicates the phenyl ring which is rotated by 20°, 40° and 60°.

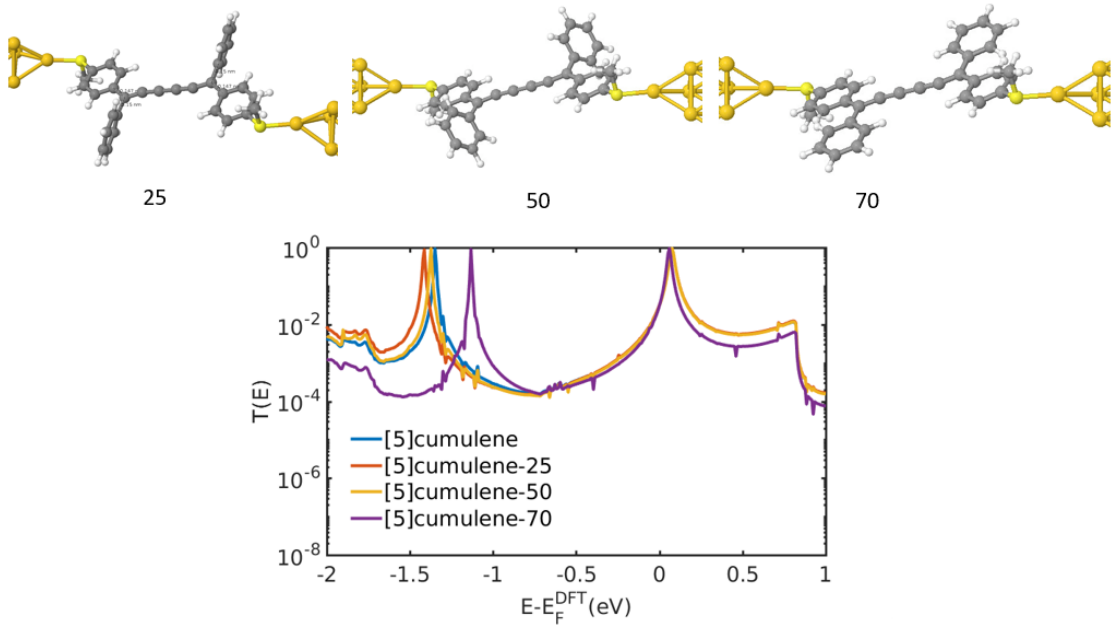

Figure 4-9 Transmission function *versus* the orientation of the two side phenyl ring relative to the plane of the two terminated phenyl rings connected to SMe anchor group for [5]cumulene.

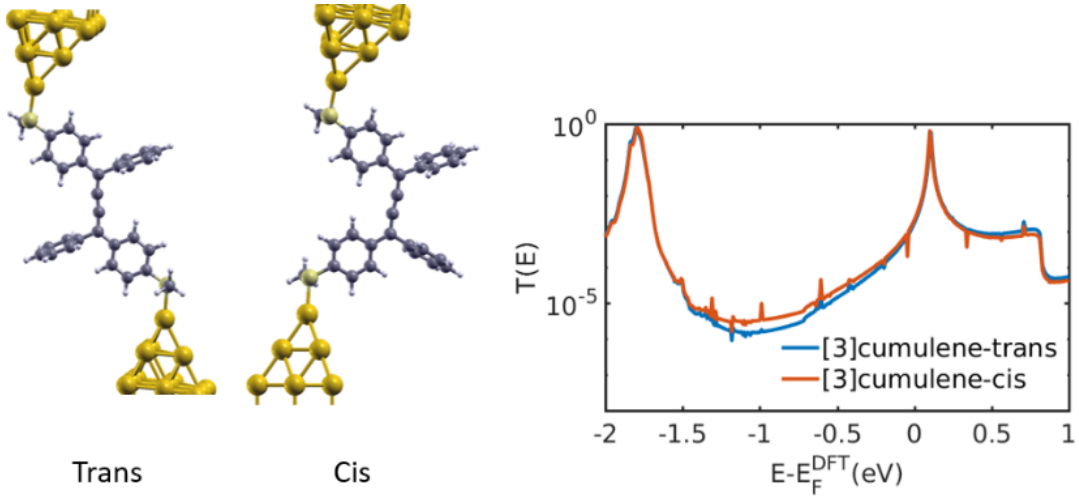

Figure 4-10 Transmission functions of two stereoisomers (*E*/*trans* and *Z*/*cis*) of the [3]cumulene.

We also explored the change in the transmission coefficient due to rotation of one phenyl ring in one terminal thioanisole group (indicated by the red arrow on the top of Figure 4-8) by 20°, 40° and 60°. The corresponding transmission functions indicate that the above trend (the conductance of [3]cumulene and [5]cumulene are similar, and both are slightly higher than that of alkene) does not change. Meanwhile, to clarify the effect of the two internal, pendant phenyl rings, taking [5]cumulene as an example, Figure 4-9 shows the effect of artificially rotating the rings by 25°, 50°, 75°, which indicate the conformation of these rings has only a small effect on the transmission coefficient within the gap. Furthermore, because the [3] and [5]cumulenes are synthesized as inseparable mixtures of *E* and *Z* isomers. Therefore, we tested whether the *E*/*Z* stereochemistry would be expected to have a strong effect on the conductance. Taking [3]cumulene as an example, Figure 4-10 shows a comparison between the transmission coefficients of the *E* and *Z* isomers and reveals that the difference between them is negligible.

4.3 Conclusion

In conclusion, this study reveals that the conductance of a series of cumulenes shows remarkably little dependence on the molecular length. This behavior is a consequence of the lack of strong bond length alternation in these compounds, which results in a steep reduction in the HOMO-LUMO gap with increasing length. [73]–[75] The [5]cumulene exhibits a high conductance of $\log(G/G_0) = -3.7$ ($\pm$ 0.5) and junctions containing this molecule are stable up to a potential difference of 1.2 V. This corresponds to maximal currents approaching microamperes. In contrast, with the shorter and more resistive allene ([2]cumulene), junctions became unstable at potentials greater than 0.5 V. The discovery that cumulenes exhibit length-independent conductance suggests that they might be used to construct longer highly-conductive molecular wires, however, this would require the development of effective strategies for controlling the reactivity of long cumulenes.[90], [91]

5 Thermoelectric Properties of Oligoglycine Molecular Wires

In this chapter, I investigate the electrical and thermoelectrical properties of glycine chains with and without cysteine terminal groups. The electrical conductance of $(\mathrm{Gly})_n$, $(\mathrm{Gly})_n\mathrm{Cys}$ and $\mathrm{Cys}(\mathrm{Gly})_n\mathrm{Cys}$ molecules (where Gly, Cys represent glycine and cysteine and n=1-3) was found to decay exponentially with length l as $e^{-\beta l}$. My results show that connecting the molecules to gold electrodes via the sulphur atom of the cysteine moiety leads to higher β factors of $1.57/\text{Å}$ and $1.22/\text{Å}$ for $(\mathrm{Gly})_n\mathrm{Cys}$ and $\mathrm{Cys}(\mathrm{Gly})_n\mathrm{Cys}$ respectively, while $\beta = 0.92/\text{Å}$ for $(\mathrm{Gly})_n$. I also find that replacing the peptide bond with a methylene group (-CH_2-) increases the conductance of $(\mathrm{Gly})_3\mathrm{Cys}$. Furthermore, I find the $(\mathrm{Gly})_1\mathrm{C}ys$ and $\mathrm{Cys}(\mathrm{Gly})_1\mathrm{Cys}$ systems show good thermoelectrical performance, because of their high Seebeck coefficients ($\sim$ 0.2 mV/K) induced by the sulphur of the cysteine(s). With the contributions of both electrons and phonons taken into consideration, a high figure of merit ZT=0.8 is obtained for $(\mathrm{Gly})_1\mathrm{Cys}$ at room temperature, which

increases further with the rise of temperature, suggesting that peptide-based SAM junctions are promising candidates for thermoelectric energy harvesting.

5.1 Introduction

Understanding electron transport through biomolecules is important, because they play central roles in cellular respiration, photosynthesis and enzymatic reactions [92]–[98]. Although much effort has been devoted to transport in peptides[99][100], the exact mechanism of charge transport through peptides and proteins is still under debate. Generally, it is accepted that quantum tunnelling through molecular orbitals is the dominant mechanism for short peptide chains[101][102] and consequently their electrical conductance G decays exponentially with length as $G = Ae^{-\beta l}$[103][104], where the prefactor A is a constant reflecting the molecule-electrode coupling strength, l is the separation between two electrodes and β is an attenuation constant. In an early work, it was reported that the attenuation factor β of cysteamine-(glycine)n-cysteine β (1.1 ± 0.1/atom or 0.87 ± 0.7/ Å) is nearly the same with that of alkanedithiol (1.0 ± 0.01/atom) in a single-molecule measurement[105]. On the other hand, in self-assembly monolayers (SAMs) of cysteine-(glycine)n it was demonstrated that oligoglycines have a smaller β factor (0.50 ± 0.02/atom) and are more conductive than alkanedithiols (0.94 ± 0.02/atom) [101]. After excluding the effect of the interactions between different peptide chains (eg hydrogen bonds) in the SAM, it was concluded that the interaction between the highest occupied amide orbitals in the single strand is the origin of the lower β factor. In contrast, scanning

tunnelling microscope-based break-junction (STM-BJ) measurements[106] revealed that the peptides of (alanine)n and (glycine)n without external anchors have greater β factors ($0.93 \pm 0.04/\text{Å}$ and $0.97 \pm 0.01/\text{Å}$) and are less conductive than the corresponding alkane chain ($0.75 \pm 0.02/$ Å) , due to the presence of tightly bound electronic states located at the peptide bond, which reduce the energy of orbitals relative to Fermi energy and the coupling to leads.

In the above measurements, although the main constituent is (glycine)n, different moieties (cysteamine ($HS(CH_2)_2NH_2$), cysteine ($HS(CH_2)_2(COOH)NH_2$), amine group (-NH_2), carboxylate group (-COO-)) are adopted as anchors, with the thiol group in cysteamine and cysteine used to connect the backbone to electrode. Anchors are expected have significant influence on the charge transport properties in molecular device[107][108][109][110], because the couplings between the molecule and the electrodes and alignment of molecular energy levels and the Fermi level of electrodes will change as anchors are modified. For example conducting atomic force microscope (AFM) measurements of anchor-(CH_2)n-anchor chains [110] demonstrate that the anchor groups have weak influence on the decay constant β. However, in oligoacene conducting probe atomic force microscopy (CP-AFM) measurements, the β factor of oligoacenedithiol ($0.2/\text{Å}$) is half that of oligoacenemonothiol ($0.5/\text{Å}$) [109]. Recently, it was demonstrated that additional electronic states due to thiol anchor groups can significantly decrease the value of β in alkane-phenyl molecular junctions[111]. Consequently, the effect of anchors on conductance and tunnelling attenuation factor β for different molecule systems should be investigated.

In this chapter, to understand the origin of the high attenuation factor measured in [14], I report the effect of anchor groups on the transport properties of single-molecule oligoglycine junctions. Furthermore, since high-β-factor molecules are likely to have high Seebeck coefficients, the thermoelectric properties of oligoglycine are investigated, to assess their potential to harness waste energy and generate electricity via the Seebeck effect. Inorganic thermoelectric materials such as Pb, Bi, Co, Sb are toxic and expensive due to limited global sources, which make them unattractive for a wide use [112]. Therefore, in recent years, different strategies have been proposed to exploit the thermoelectric properties of nanostructured organic materials or organic molecules[113][114][115][116]. Single-molecule devices provide a possible building block for constructing high-efficiency thermoelectric power generators[117]. However, to our knowledge, there are few reports about the thermoelectric properties of peptides. In the present work, I find that connecting to electrodes via sulphur anchor groups leads to higher β factors of 1.57/Å, 1.22/Å and 0.92/Å for $(\mathrm{Gly})_n\mathrm{Cys}$, $\mathrm{C}ys(\mathrm{Gly})_n\mathrm{Cys}$ and $(\mathrm{Gly})_n$ respectively. It is also found that replacing the peptide bond with a methylene group could increase the conductance of single- $(\mathrm{G})_3\mathrm{C}$ molecular junctions. In addition, I find the $(\mathrm{Gly})_n\mathrm{Cys}$ and $\mathrm{Cys}(\mathrm{Gly})_n\mathrm{Cys}$ systems show good thermoelectrical properties with high Seebeck coefficients ($\sim$0.2 mV/K) induced by the sulphur in cysteine. Furthermore, after considering both the phonon and electron contributions, for $(\mathrm{Gly})_1\mathrm{Cys}$ a high figure of merit $ZT \approx 0.8$ could be obtained at room temperature, which increases further as the temperature increases.

5.2 Results and discussions

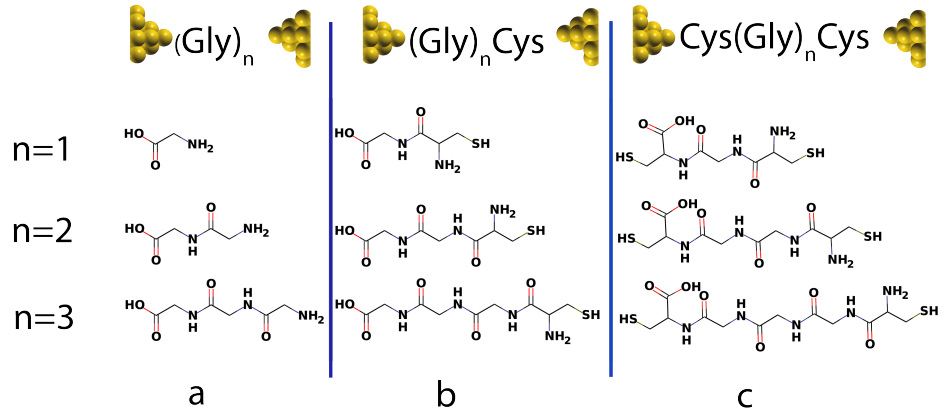

Figure 5-1 Au-molecule-Au junctions of oligoglycine system with three different anchors. Gly and Cys stand for glycine and cysteine separately and n=1-3. (a) Oligoglycine connected to gold electrodes directly. (b) Oligoglycine connected to gold electrodes by cysteine-peptide molecule where sulphur is the anchor atom. (c) Oligoglycine with two ends of cysteine connected to gold electrodes. For each series, the molecular structures (n=1-3) are shown below.

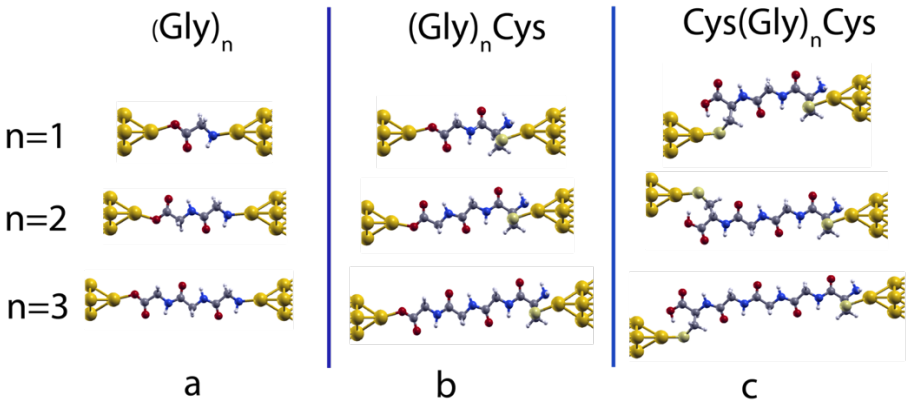

Figure 5-2 Au-molecule-Au junctions of oligolycine system with three different anchors. The red, grey, white, blue and pale yellow balls represent oxygen, carbon, hydrogen nitrogen and sulphur respectively. Four yellow balls at both ends represent gold leads.

Usually, three ways are used to bind peptide molecules to gold electrode: through alkyl thiols[118][119], through thiol-contained amino acids (cysteines)

[101][105][120] or through the "N-terminal" and "C-terminal" residues[106]. Here, I adopt the latter two methods, since they allow investigation of charge transport properties without introducing external groups. Figure 5-1 shows the junction conformations investigated below. In Figure 5-1(a), oligoglycine $(Gly)_n$ (n=1-3) is connected to gold electrodes directly, where one end is $-COO^-$, which could be achieved when the solution pH is 7 or higher[121], and the other is $-NH_2$. Based on the molecules in Figure 5-1(a), in Figure 5-1(b) oligoglycine $(Gly)_n$ is connected to gold electrodes through the thiol group incorporated in cysteine-peptide residues. For Figure 5-1(c), two cysteines are attached to the oligoglycine $(Gly)_n$ system at both ends, where the thiol groups serve as anchors. See Figure 5-2 for more detailed configurations.

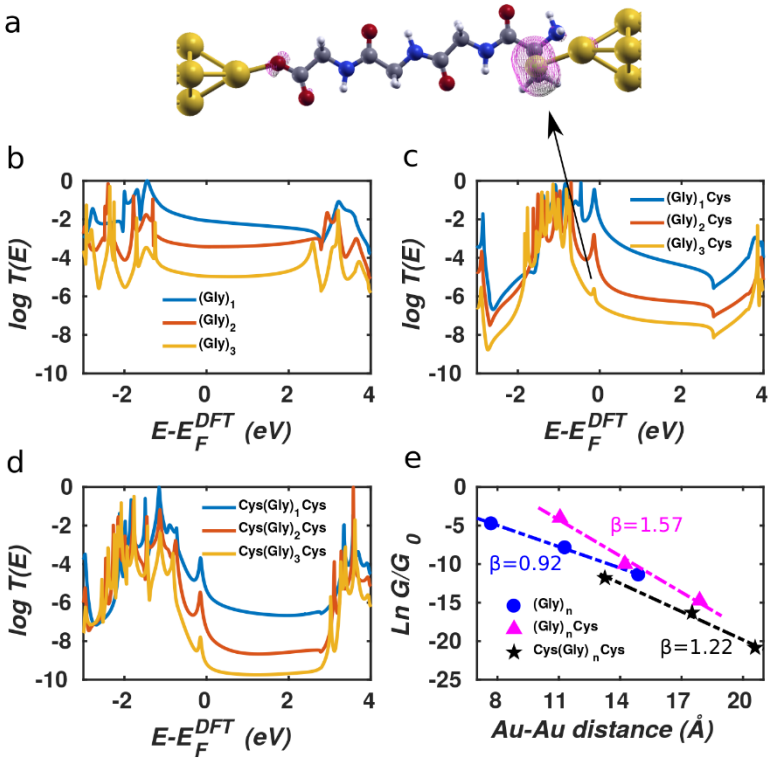

Figure 5-3 Transport properties for the three series of single oligoglycine devices. (a) shows the spacial local density of states (LDOS) of the peak around -0.2eV for

$(Gly)_3Cys$. The red, grey, white, blue and pale yellow balls represent oxygen, carbon, hydrogen nitrogen and sulphur respectively. Four yellow balls at both ends represent gold leads. (b-d) The transmission spectra of (b) $(Gly)_n$, (c) $(Gly)_nCys$, and (d) $Cys(Gly)_nCys$ as the function of $E - E_F^{DFT}$, where E is the energy of electron, E_F^{DFT} is the Fermi energy predicted by DFT. (e) The corresponding conductance evolution versus the increasing separation between the two electrodes. The blue, magenta and black dots stand for the conductance derived from the transmission spectra in (b-d) while the corresponding dashed lines show the corresponding linear fit with $y = \beta x + b$ where y is the natural logarithm of conductance G/G_O and x is the separation between two apex-Au atoms of the pyramids in the gold electrodes.

After computing the electron transmission functions $T(E)$ of these junctions (see methods), the low temperature electrical conductance G is given by $G = G_0 T(E_F)$, where G_0 is the conductance quantum and E_F is the Fermi energy of the electrodes. (see methods for the room-temperature formula) The computed transmission curves $T(E)$ of the junctions in Figure 5-1 are presented in Figure 5-3. The DFT-predicted Fermi energy E_F^{DFT} of $(Gly)_n$ is close to middle of the gap between the highest occupied molecular orbital (HOMO) and the lowest unoccupied molecular orbital (LUMO), while the Fermi energies of $(Gly)_nCys$ and $Cys(Gly)_nCys$ systems are located close to HOMO, because of the influence of the sulphur [122]. Since the Fermi energy of glycine-peptide-based junctions lies close to the HOMO, this means that charge transport in glycine-peptide-based junctions is hole-mediated, in agreement with the literature [106][123][118].

This phenomenon is demonstrated by the local density of states (LDOS) near the resonance of between -0.5eV and 0 shown in Figure 5-3a for molecule $(Gly)_3Cys$. The magenta surface shows that the weight of the LDOS corresponding to the peak

indicated by the arrow in Figure 5-3c is mainly located on the sulphur atom. Similar features are observed in Figure 5-3d, where sulphur atoms are also present.

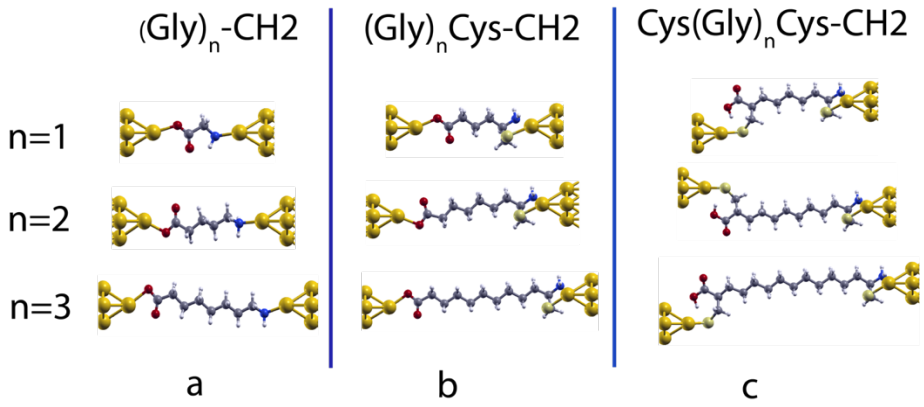

Figure 5-4 Based on the structures in Figure 5-2, I replace the peptide bonds in the middle of the molecules without changing the anchors to obtain the β factor.

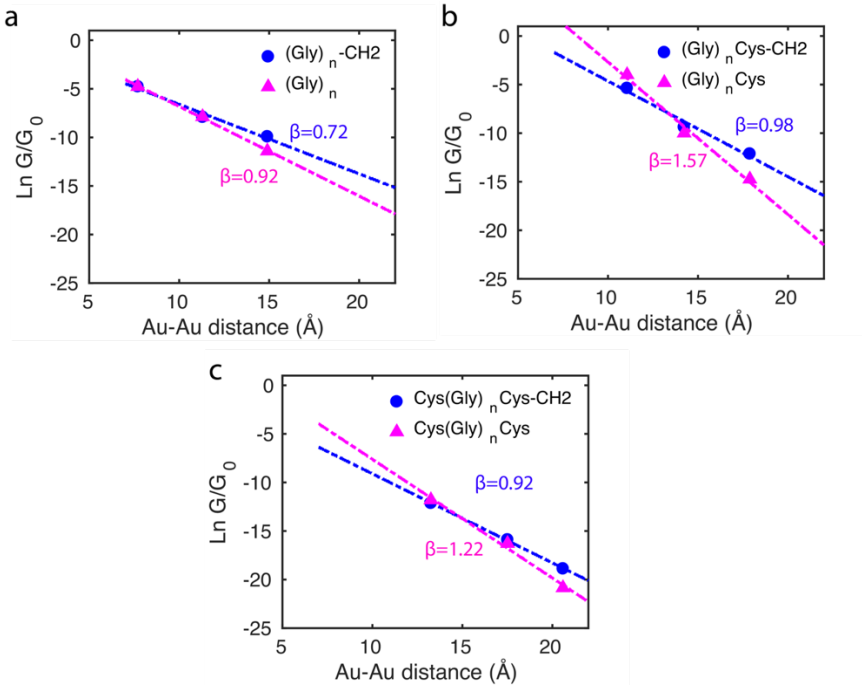

Figure 5-5 Comparison between β factors of oligoglycine before and after substituting peptide bond with -CH2- corresponding the structures shown in Figure 5-2 and Figure 5-4 (a) $(Gly)_n$, (b) $(Gly)_nCys$ and (c) $Cys(Gly)_nCys$. Which

shows after substituting with -CH2- group, the β factor becomes lower for each series comparing with peptide chain.

As the number of glycines increases from one to three for the three short peptide series with different anchor groups shown in Figure 5-1, the distance between the two gold-apex atoms in the pyramids of electrodes increases and the conductance of the junctions decreases. Since the Fermi energy is located within the HOMO-LUMO gap, charge transfer takes place via off resonant tunnelling [124] and as shown in Figure 5-3e, the conductance decays exponentially with distance is expected. After fitting the logarithm of the room-temperature conductance to a linear function and extracting the β factor for each series, I find that the β parameter for $(\mathrm{Gly})_n$ system is the smallest at $0.92/\text{Å}$, which agrees quite well with the result reported in literature[106], while the $(\mathrm{Gly})_n\mathrm{Cys}$ system has $\beta = 1.57/\text{Å}$ and the $\mathrm{Cys}(\mathrm{Gly})_n\mathrm{Cys}$ has $\beta = 1.22/\text{Å}$, both of which are higher than the β factor of $(\mathrm{Gly})_n$ system. This difference between the β factors of junctions with thiol and dithiol anchor groups has been reported in oligoacene systems[109]. I also note that the three calculated β factors are all greater than that of the oligoglycine-based SAM conductance measurements of Mostafa et. al [101]. For each series, I obtain lower β factors after replacing the peptide bond in the middle of the molecules with $-CH_2-$ group, indicating the peptide chain is less conductive than the saturated alkane chain as shown in Figure 5-5.

In order to obtain further insight into the mechanism of charge transport through peptide backbones, I investigated the effect of substituting the peptide bonds with methylene groups, as shown on the left of Figure 5-6. These molecules were investigated experimentally in ref [101]. In Figure 5-6a-c, the molecules

sandwiched in junctions are: $(Gly)_3Cys$, $(Gly)_3Cys$ with one peptide substituted by two -CH_2- groups (denoted $(Gly)_3Cys$-A) and $(Gly)_3Cys$ with two peptides substituted by four -CH_2- groups (denoted $(Gly)_3Cys$-B). Their corresponding transmissions are plotted in Figure 5-6d. I find that the transmission does not change significantly when replacing one peptide with two methylene groups, while the transmission increases rapidly when two peptide bonds are substituted. This shows that the lone pairs of electrons in oxygen and nitrogen atoms in oligopeptides do not enhance the single-molecule conductance compared with fully saturated alkane chains, which is consistent with literature results for oligoglycines without external sulphur anchors [106]. The similar phenomena of heteroatom substitution is found in oligoethers, where the conductance of alkanedithiols decreases after substituting every third -CH_2- group with O or S [125][126]. This feature can be understood by examining the LDOS as shown in Table 3.1, where an energy window from -0.5 to 0 eV has been chosen, which includes the peak dominating the transport (as shown in Figure 5-6). For $(Gly)_3Cys$ and $(Gly)_3Cys$-A, the weights of states in the centers of the molecules is small, while the states are extended across several carbon atoms in the middle of $(Gly)_3Cys$-B chain, indicating a better ability to transport electrons. These differences in LDOS originate from quantum interference among the different molecular paths[115][127] and variations in the coupling between the molecules and electrodes[128].

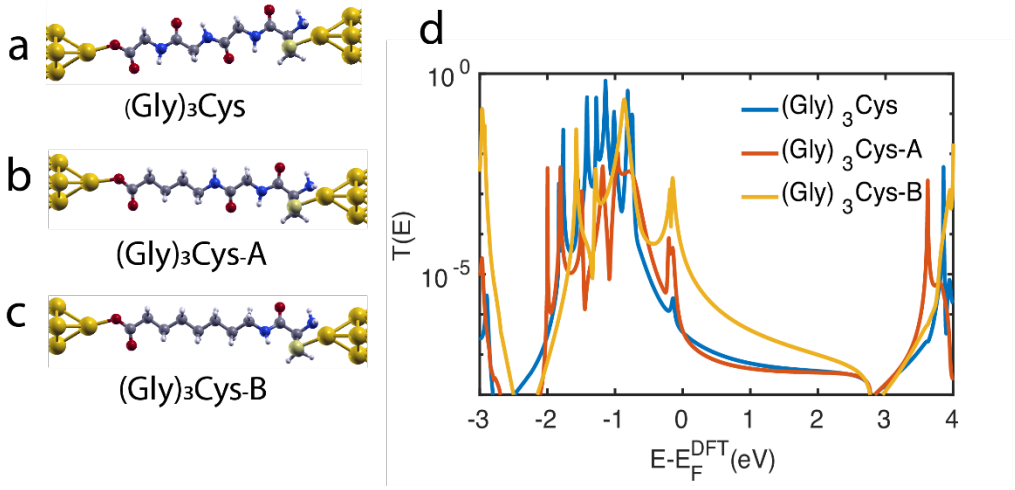

Figure 5-6 Transmission spectra of the junctions with the peptide bond replaced by methylene groups for $(Gly)_3Cys$ gradually. On the left, from top to bottom (a-c), the molecules sandwiched in junctions are: $(Gly)_3Cys$, $(Gly)_3Cys$ with one peptide substituted by two CH_2 groups ($(Gly)_3Cys$-A) and $(G)_3C$ with two peptides substituted by four CH_2 groups ($(Gly)_3Cys$-B).

isosurface	$(Gly)_3Cys$	$(Gly)_3Cys$-A	$(Gly)_3Cys$-B
0.01	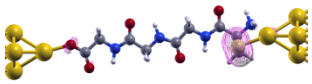	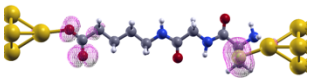	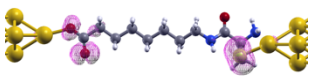
0.001	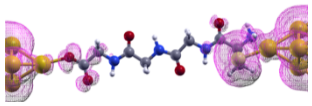	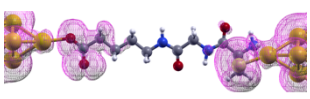	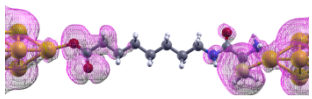
0.0001	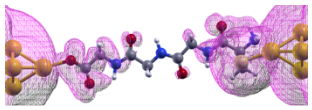	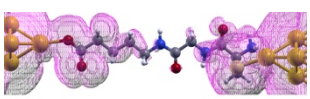	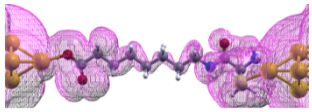
0.00006	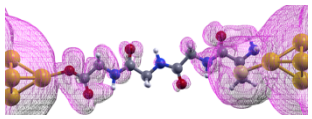	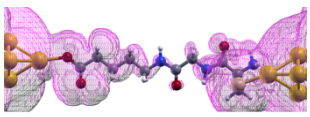	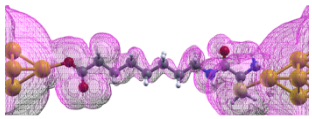

Table 3.1 The LDOS with magenta color in the energy window from -0.5 to 0 for $(Gly)_3Cys$, $(Gly)_3Cys$-A and $(Gly)_3Cys$-B incorporated in two gold leads separately with the decreasing isosurface from 0.01 to 0.00006.

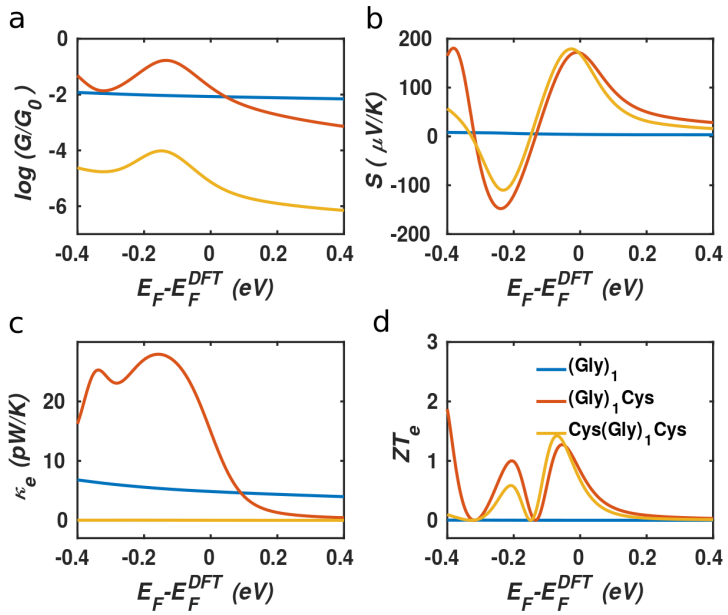

Figure 5-7 Thermoelectric properties as the function of energy relative to DFT-estimated Fermi energy $E_F - E_F^{DFT}$ at room temperature 300 K. (a) Electrical conductance (G), (b) Seebeck coefficients (S), (c)-(d) Electronic contribution to thermal conductance (κ_e) and figure of merit ZT_e . The blue, red and orange curves represent the $(Gly)_1$, $(Gly)_1Cys$ and $Cys(Gly)_1Cys$ junctions respectively.

Studies of transport through peptides have mainly focused the effect of side groups[118], the effect of the PH value of the solution[105] and the effect of secondary structure[99]. However, their thermoelectric properties have not been investigated extensively. Since many varieties of biomolecules can be assembled on metal surfaces to form SAM-based junctions[101][118], peptide-based thermoelectric materials could be a promising future target, provided that the thermoelectric properties of single molecules are sufficiently attractive. When the Fermi energy is located close to a HOMO resonance, a large Seebeck coefficient $\boldsymbol{S}$ is expected, because according to the Mott formula, $\boldsymbol{S}$ is proportional to the slope of the transmission coefficient T(E) at the Fermi energy [129][130][131].

In our case, the high slopes of the transmission curves around Fermi energy for $(\mathrm{Gly})_n\mathrm{Cys}$ and $\mathrm{Cys}(\mathrm{Gly})_n\mathrm{Cys}$ systems indicate that oligoglycines might be promising candidates for thermoelectric energy-harvesting materials. Figure 5-7 shows the thermoelectric properties of Gly, GlyCys and Cys(Gly)Cys molecules containing a single glycine group. In a large energy window within the HOMO-LUMO gap, the conductance decreases due to the increase of molecular length when one or two cysteines are added. However, near the Fermi energy, the electrical conductance of glycine with one cysteine is comparable or even higher than the one without cysteine, due to the peak caused by the sulphur anchor. For $\mathrm{Cys}(\mathrm{Gly})_1\mathrm{C}ys$, the electrical conductance is approximately three orders of magnitude lower than the $(\mathrm{Gly})_1\mathrm{Cys}$ and Gly devices. Similarly, the thermal conductance due to electrons of $\mathrm{Cys}(\mathrm{Gly})_1\mathrm{Cys}$ is much lower than those of other two structures. For glycine with cysteine(s), the Seebeck coefficients both reach to 0.2 mV/K at the vicinity of Fermi energy. Consequently a higher ZTe value ~1.5 could be obtained when oligoglycine is terminated by cysteines, as shown in Figure 5-7d around -0.05eV. In addition, the Seebeck coefficients and thermoelectric figures of merit are quite similar for the two molecules with cysteines. Figure 5-8 shows the effect of temperature on the thermoelectric performance and reveals that the electronic thermoelectric figure of merit ZT_e could increase further with increasing temperature.

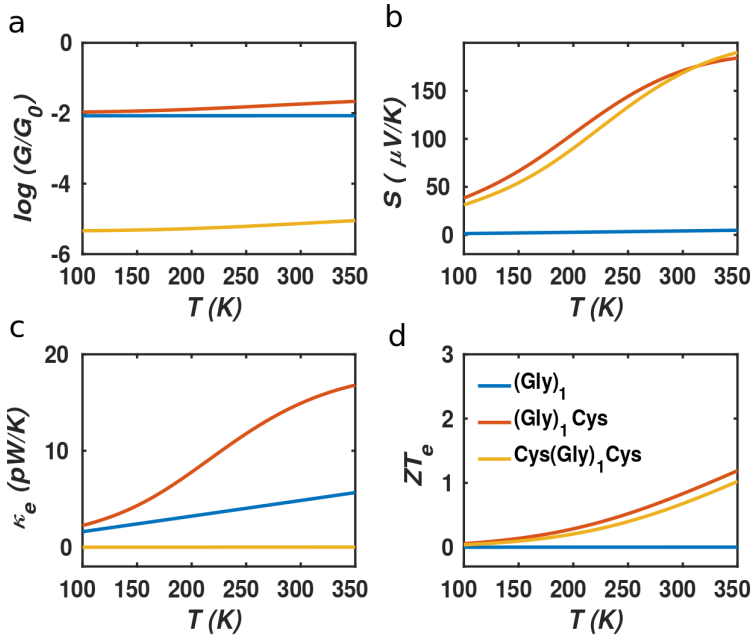

Figure 5-8 Thermoelectric properties as the function of temperature T at the DFT-estimated Fermi energy. (a) Electrical conductance (G), (b) Seebeck coefficients (S), (c)-(d) Electronic contribution to thermal conductance (κ_e) and figure of merit ZT_e. The blue, red and black curves represent the $(Gly)_1$, $(Gly)_1Cys$ and $Cys(Gly)_1Cys$ junctions separately.

It should be noted that the presented figure of merit ZTe in Figure 5-7 and Figure 5-8 excludes the contribution of phonons. When phonons are included, the full ZT will certainly be lower than ZTe, as discussed in literatures[112], [132]. Therefore, the phonon contribution to thermal conductance is also investigated. The phonon transmission and the corresponding phononic thermal conductance are shown in Figure 5-9a and b. The room-temperature thermal conductance due to phonon decreases from 14.6 pW/K to 10.8 pW/K, and then to 9.7 pW/K because the molecular lengths increase for $(Gly)_1$, $(Gly)_1Cys$ and $Cys(Gly)_1Cys$ junctions. The figure of merit ZT at room temperature versus Fermi energy are plotted in Figure 5-9c. Different from the evolution of ZTe, the ZT of $Cys(Gly)_1Cys$ is reduced to

nearly 0 since its phononic thermal conductance (~9.7 pW/K) plays a dominant role compared to the electronic part (~0.01 pW/K) as shown in Figure 5-7 and Figure 5-8. While for $(Gly)_1Cys$, since its phononic thermal conductance (about 10.8 pW/K) is comparable to its electronic counterpart (about 15 pW/K), ZT is approximately reduced by half compared with ZTe. Consequently, for $(Gly)_1Cys$, a high ZT = 0.8 is obtained around -0.05eV, as shown in Figure 5-9c. Figure 5-9d demonstrates the evolution of ZT at DFT-estimated Fermi energy as the function of temperature where ZT of (Gly)1Cys increases to 0.7 when the temperature reaches 350K and the other two series show ZT≈0.

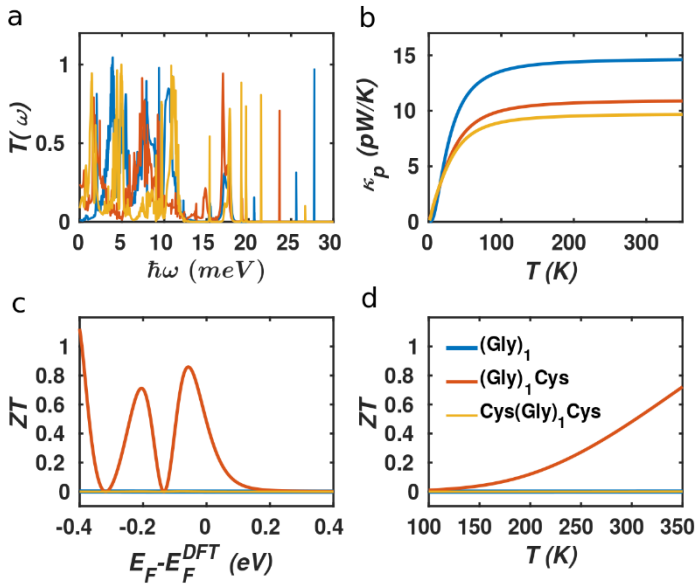

Figure 5-9 (a) Phonon transmission functions, (b) Phononic contribution to the thermal conductance, (c) Room-temperature ZT versus Fermi energy, (d) ZT at the DFT-estimated Fermi energy as the function of temperature. The blue, red and orange curves represent the $(Gly)_1$, $(Gly)_1Cys$ and $Cys(Gly)_1Cys$ junctions separately.

5.3 Conclusion

Combining density functional theory and Green's function scattering techniques, I have calculated the electrical conductance as a function of energy for $(Gly)_n$, $(Gly)_nC$ and $Cys(Gly)_nCys$ systems. Our results show that anchors containing sulphur have significant influence on their transport properties and lead to higher β factors. In particular, I find β factors of 1.57 /Å and 1.22 /Å for $(Gly)_nCys$ and $Cys(Gys)_nCys$ respectively while $\beta = 0.92$ /Å for $(Gly)_n$. Furthermore, it is also found that replacing the peptide bond with a methylene group increases the conductance of single-$(Gly)_3Cys$ molecular junctions. This demonstrates that the lone pairs of electrons in oxygen and nitrogen atoms in oligopeptide do not enhance the single-molecule conductance in comparison with fully saturated alkane chains. I find the $(Gly)_nCys$ and $Cys(Gly)_nCys$ systems show good thermoelectrical properties with high Seebeck coefficients ($\sim$0.2 mV/K) induced by the sulphur in cysteine. After taking both phonons and electrons contributions into account, I find the $(Gly)_1Cys$ shows good thermoelectrical properties where a high figure of merit ZT=0.8 could be achieved at room temperature and the ZT shows an increasing trend with the rise of temperature. This high ZT implies that peptide-based SAM junctions are promising candidates for thermoelectric energy harvesting.

6 Solvent Gating of the Single Molecular Junction Charge Transport Properties

To further understand the mechanism of how environment affect the nanoscale charge transport properties, the conductance of single molecular junctions in contrasting solvent environments were measured by colleagues in Xiamen University using mechanically controllable break junction technique. They found that the conductance of single molecular junctions can be manipulated by controlling the solvent environment in the range of nearly an order of magnitude. My theoretical calculations presented below suggest that the polar solvent shifts molecular orbitals energy depending on the coupling strength related to anchoring groups. The polar solvent reduces the energy gap between molecular orbitals and Fermi level of the electrode in the case of weak coupling while the broadening of molecular orbitals, caused by strong coupling, closes the energy gap. The work revealed that the effects of solvent should be taken into account while the anchoring groups in single molecular junctions are less robust. The control of conductance can be used to develop future functional nanoscale electronic devices.

6.1 Introduction

Charge transport properties of various molecules have been reported since the Mechanically controllable break junction (MCBJ) technique was confirmed as one of the most productive approaches to experimentally investigate electrical signal of single molecular junctions.[133], [134] The liquid environment is necessary to guarantee the stability of forming single molecular junctions in MCBJ measurements. Researchers were conscious of the solvent effects long before, but to date, only a small number of solvent effects have been investigated and only for a limited number of particular molecular systems. Depending on the system, these studies show that the mechanisms of solvent effects could be very different, which can be interpreted as being due to the solvent binding to the functional groups in molecular frameworks [135], electrostatic interactions between solvent and molecular backbone [136], protonation tuning of specific molecules with quantum interference effects [137] or solvent binding to gold electrode couple. [138], [139] Exploring the interaction between solvents and single molecular junctions should provide us with effective approaches to manipulate molecular charge transport properties and design nanoscale electronic devices further.

In this chapter, I demonstrate and explain a significant solvent gating effect on the conductance of single molecular junctions, revealed in a collaboration with experimental colleagues from Xiamen University. Oligophenylethynylene-Sulfurmethyl (OPE-SMe) is used as conducting molecule to form single molecular junctions, whose highly aromaticity and rigidity makes them an ideal candidate for elementary building blocks in constructing molecular wires. The mixture of 20

vol% tetrahydrofuran (THF) and 80 vol% 1,3,5-trimethylbenzene (TMB) used to be the standard solvent in single molecule conductance measurement (THF for solubility, TMB for stability and low permittivity) [140]. However, the solvents could also control the charge transport properties of single molecular junctions. To investigate this possibility, the conductance measurements of OPE-SMe in different solvents were carried out using MCBJ technique (as shown in Figure 6-1). It is found that the conductance of OPE-SMe can be improved by up to about one order of magnitude higher by adjusting the solvent environment, and we can manipulate the conductance to specific value within a certain range.

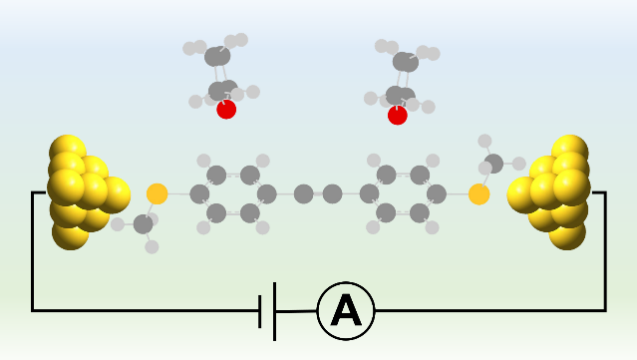

Figure 6-1 Schematic of MCBJ configuration.

6.2 Results and discussion

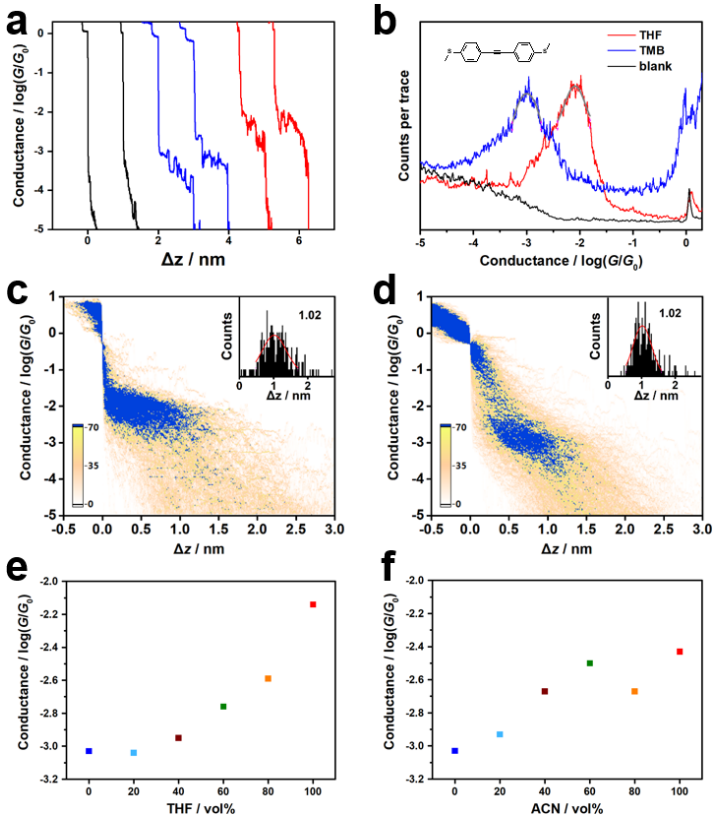

Figure 6-2 (a) Typical individual conductance-distance traces of pure TMB (black) and OPE-SMe junctions in different solvents (TMB in blue and THF in green). (b) Conductance histograms of pure TMB and OPE-SMe junctions in different solvents from ~1000 traces without data selection. (c) 2D conductance-displacement histograms constructed from ~1000 traces for OPE-SMe in THF or (d) TMB. Inset: The relative displacement distribution histograms. (e) Most probable conductance values of OPE-SMe in corresponding mixed solvents (THF and TMB v:v = 0:1 (blue), 1:4 (LT blue), 2:3 (wine), 3:2 (olive), 4:1 (orange), and 1:0 (red)). (f) Most probable conductance values of OPE-SMe in corresponding mixed solvents (ACN and TMB v:v = 0:1 (blue), 1:4 (LT blue), 2:3 (wine), 3:2 (olive), 4:1 (orange), and 1:0 (red)).

Using pure THF and TMB to prepare 0.01 mM/L solution of OPE-SMe respectively. For each condition, conductance-distance traces (as shown in Figure 6-2a) were

recorded in a continuous period. The individual traces show the variation of conductance as a function of distance while the process of breaking single molecular junction. It is found that the conductance rapidly drops to the plateau of molecular signal after a short stay at the quantum of conductance (G_0), which marks the rupture of Au-Au atomic contact followed by the formation of Au-molecule-Au junction, and then goes to the tunneling background. The one-dimensional conductance histograms in Figure 6-2b, constructed from thousands of corresponding traces, show the conductance peaks that indicate the most probable junction conductance. The conductance of OPE-SMe, determined from Gaussian fit to histograms, shows highly solvent-dependence, and peaks at $10^{-2.1}$ and $10^{-3.0}$ G_0 in THF and TMB, respectively. The two-dimensional conductance-displacement histograms were constructed, as shown in Figure 6-2c, d, to explore if solvents alter the configuration of molecular backbone. Insets of Figure 6-2c, d show the displacement distribution analysis of molecular plateaus, suggesting the configuration of OPE-SMe junctions are fully elongated in solvents.

The conductance of OPE-SMe were measured in various volume ratios of THF and TMB. As the molecular dipole moment, permittivity and the ability of attract electron are totally different comparing THF with TMB, mixing them with certain volume ratio would provide the gradient variation of solvent environment. Figure 6-2e shows statistical conductance of OPE-SMe junctions in different mixtures of THF and TMB. The single molecular conductance of OPE-SMe is found to correlate with the volume ratio of THF in mixed solvent. This solvent dependence also can be found in another common polar solvent (acetonitrile/ACN), as shown in Figure 6-2f.

To explore the solvent gating effect on charge transport through some common molecular wires, a control experiment was carried out with Oligoaryleneethynylene (OAE), 1,8-octanedithiol (ODT) and Oligophenylethynylene-Sulfuracetyl (OPE-SAc). Results of conductance measurements for OAE, ODT and OPE-SAc in different solvents are shown in Figure 6-3a, b, c. Comparing with literature data ($G_{OAE}=10^{-3.3}$ G_0, Hong et al. [141] and $G_{ODT}=10^{-3.6}$ G_0, Li et al.),[142] the single molecular junctions conductance of OAE, ODT and OPE-SAc do not show that one order of magnitude solvent induced shift in single molecular conductance measurement. Therefore it is suggested that the solvents may take effect on molecular junctions with specific anchoring groups. As the THF has a low boiling point, it evaporates very quickly during the conductance measurement. Measuring the different concentration of OPE-SMe in THF, the conductance shows stability with change of concentration.

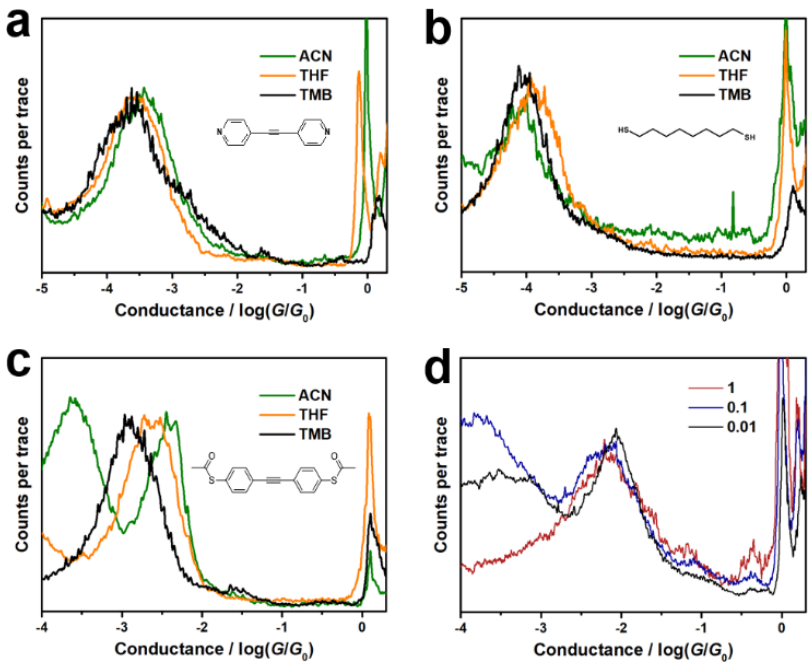

Figure 6-3 (a) Conductance histograms of OAE in different solvents (TMB in black, THF in orange, and ACN in green) from ~1000 individual traces. (b) Conductance

histograms of ODT in different solvents (TMB in black, THF in orange, and ACN in green) from ~1000 individual traces. (c) Conductance histograms of OPE2-SAc in different solvents (TMB in black, THF in orange, and ACN in green) from ~1000 individual traces. (d) Conductance histograms of OPE2-SMe in THF with different concentration (1 mM in red, 0.1 mM in blue, and 0.01 mM in black).

However, there is no functional groups on OPE-SMe backbone for THF or TMB to form chemical bond, and the interaction between solvents and gold atoms is too weak to affect the contact work function. Thus, electrostatic interactions are predicted to play a predominant role in gating the conductance of molecular junctions by shifting the energy of molecular frontier orbitals.

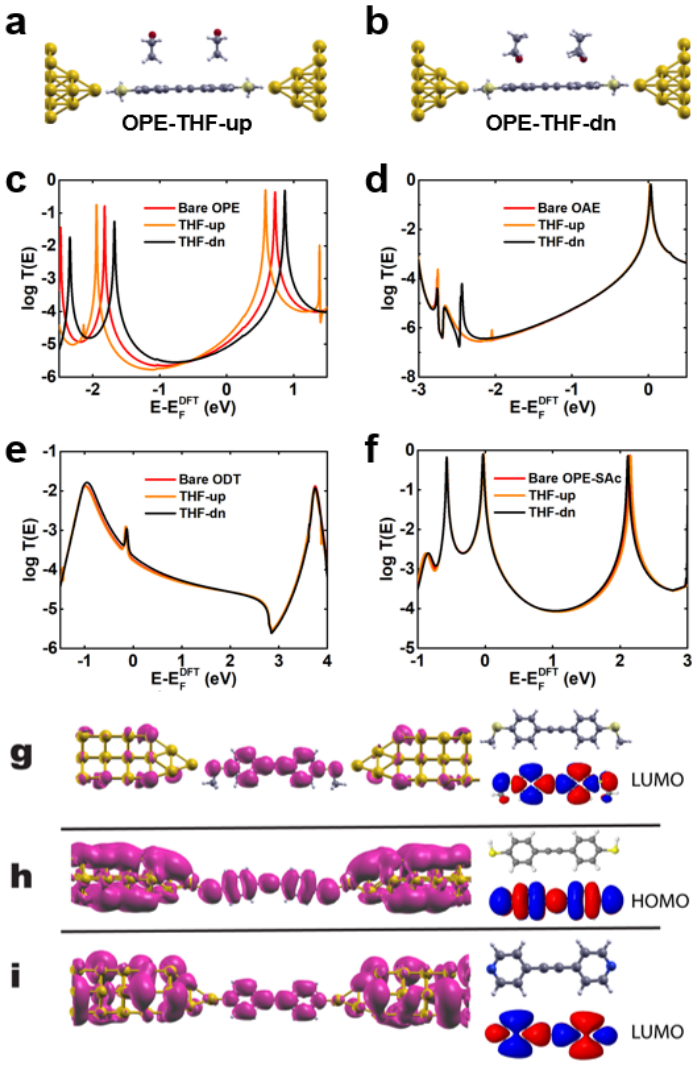

Figure 6-4 (a) The conformation for OPE-SMe with two THF molecules pointing outside named as 'THF-up'. (b) The conformation for OPE-SMe with two THF molecules pointing inside named as 'THF-dn'. The transmission coefficient T(E) vs electron energy for (c) OPE-SMe, (d) OAE, (e) ODT and (f) OPE-SAc with or without two THF molecules. For the case with THF molecules, the conformation is similar with (a) and (b). (g) The LDOS (left) with magenta color in the energy window 0.1 eV around LUMO resonance peak and the isolated OPE-SMe molecule as well as the corresponding LUMO (right), and for the case of (h) OPE-SAc and (i) OAE.

In order to gain further insight into how the conductances responds with different solvent molecules, transmission spectra T(E) were calculated by combining the DFT package SIESTA with the quantum transport code Gollum. Different molecules OPE, OAE, ODT measured in experiment are attached to gold electrodes in simulations and different solvents THF, ACN, TMB are considered. For solvent molecules with an electric dipole moment (e.g. THF and ACN), only the conformations with the dipole moment pointing inside or outside the backbone molecule are shown in Figure 6-4a. For solvent molecule without electric dipole moment (e.g. TMB), two configurations are chosen: the TMB parallel and TMB perpendicular to the backbone, as shown in Figure 6-5b.

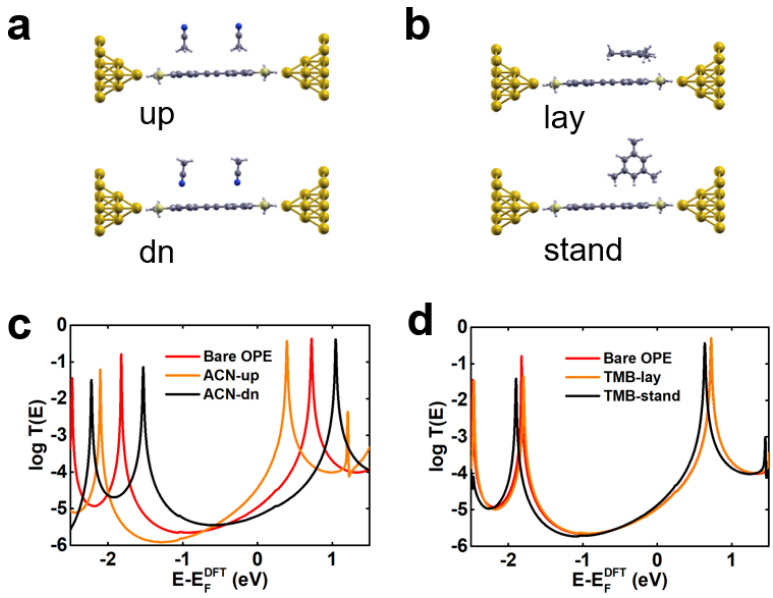

Figure 6-5 The conformation for OPE anchored by SMe group to two gold leads with two solvent molecules pointing different sides (a) ACN (b) TMB. The transmission spectra of OPE anchored by SMe group to two gold leads with and without solvent molecules (c) ACN (d) TMB.

The role of anchors in the conductance measurement in the presence of polarized solvent molecule was firstly considered. To simplify the problem, backbone molecules were fixed during the optimization process, while only the solvent molecules were allowed to relax. The results for THF are shown in Figure 6-4. For OPE-SMe, when the oxygen-side of THF solvent molecule is close to the backbone, the transmission curve shifts to higher energy (black curve in Figure 6-4); In contrast, when the other end of solvent molecule moves close to it, the transmission curve shifts to lower energy (orange curve in Figure 6-4). The two opposite shifting of transmission function is attributed to different gating effects due to the orientation of solvent around where the dipole moment points from the positive side to negative oxygen-side. However, for backbone molecules OAE, ODT

and OPE-S with solvent molecule, their transmission functions nearly doesn't change in a large range near DFT-predicted Fermi energy comparing to the bare OAE , ODT and OPE-S, indicating their conductance are less likely influenced by the solvent shown in Figure 6-4d, e and f. Similar shifting trends in transmission function of the three backbone molecule are observed in solvent ACN as shown in Figure 6-5, Figure 6-6, Figure 6-7 and Figure 6-8.

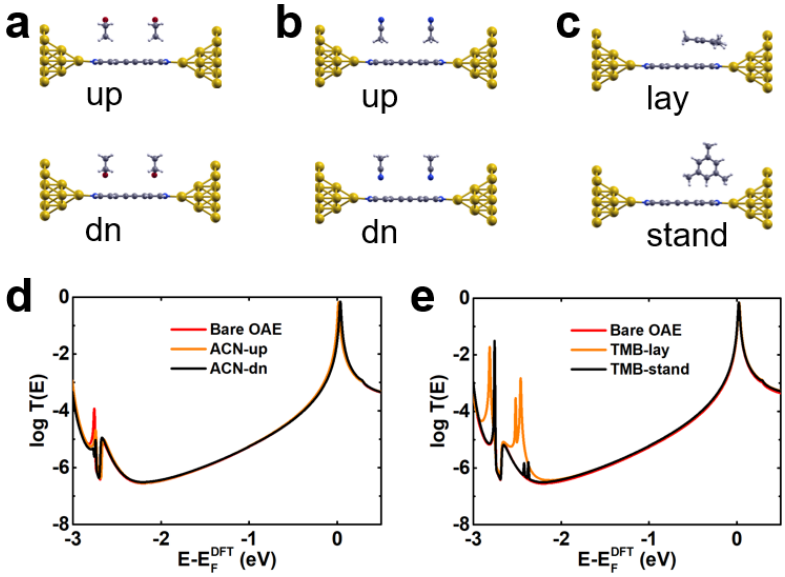

Figure 6-6 The conformation for OAE with two solvent molecules pointing different sides (a) THF (b) ACN (c) TMB. The transmission spectra of OAE attached to two gold leads with and without solvent molecules (d) ACN (e) TMB.

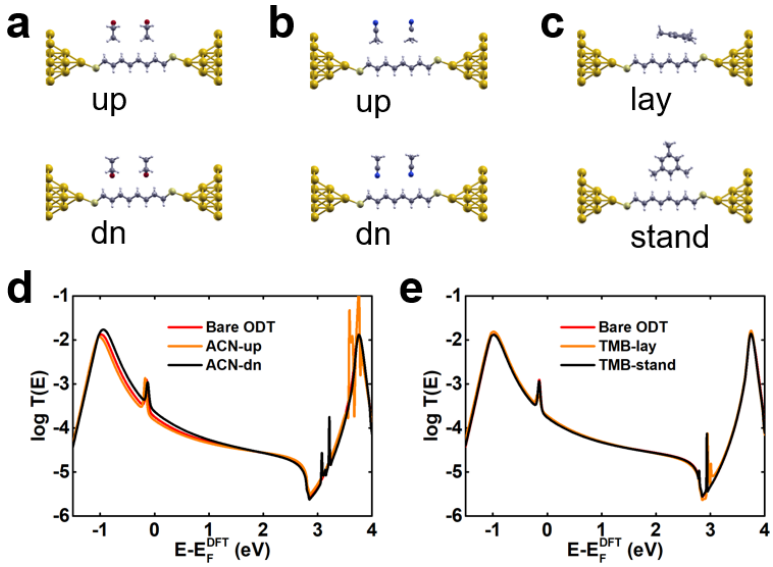

Figure 6-7 The conformation for ODT with two solvent molecules pointing different sides (a) THF (b) ACN (c) TMB. The transmission spectra of ODT attached to two gold leads with and without solvent molecules (d) ACN (e) TMB.

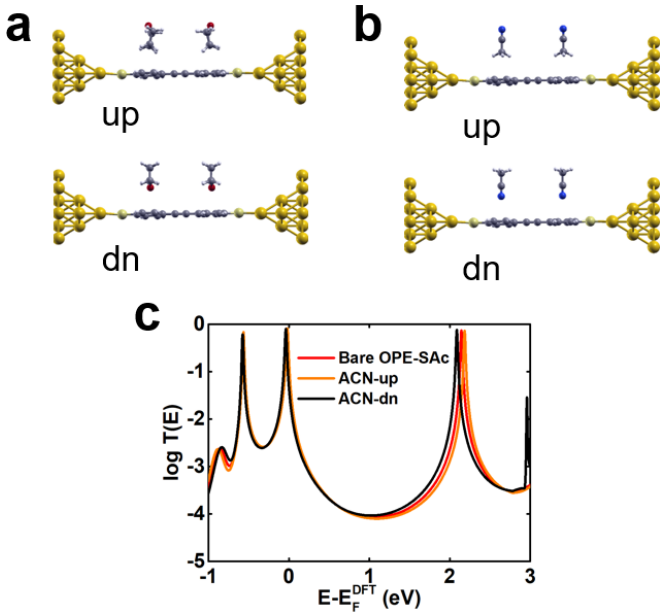

Figure 6-8 The conformation for OPE anchored by SAc to two gold leads with two solvent molecules pointing different sides (a) THF (b) ACN. The transmission spectra of OPE anchored by SAc to two gold leads with and without solvent molecules (c) ACN.

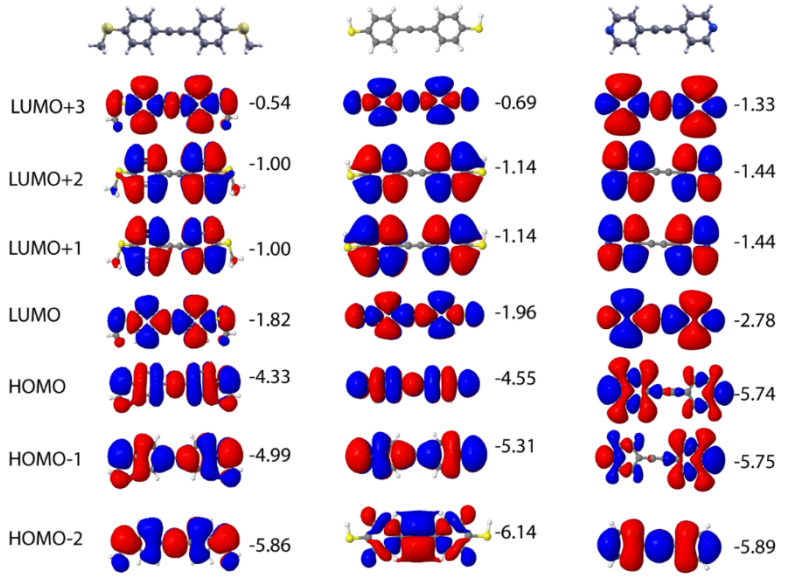

Figure 6-9 The frontier molecular orbitals HOMO-2, HOMO-1, HOMO, LUMO, LUMO+1, LUMO+2 and LUMO+3 of isolated molecules of OPE-SMe, OPE-SH and OAE as well as the corresponding energy eigenvalues (in eV).

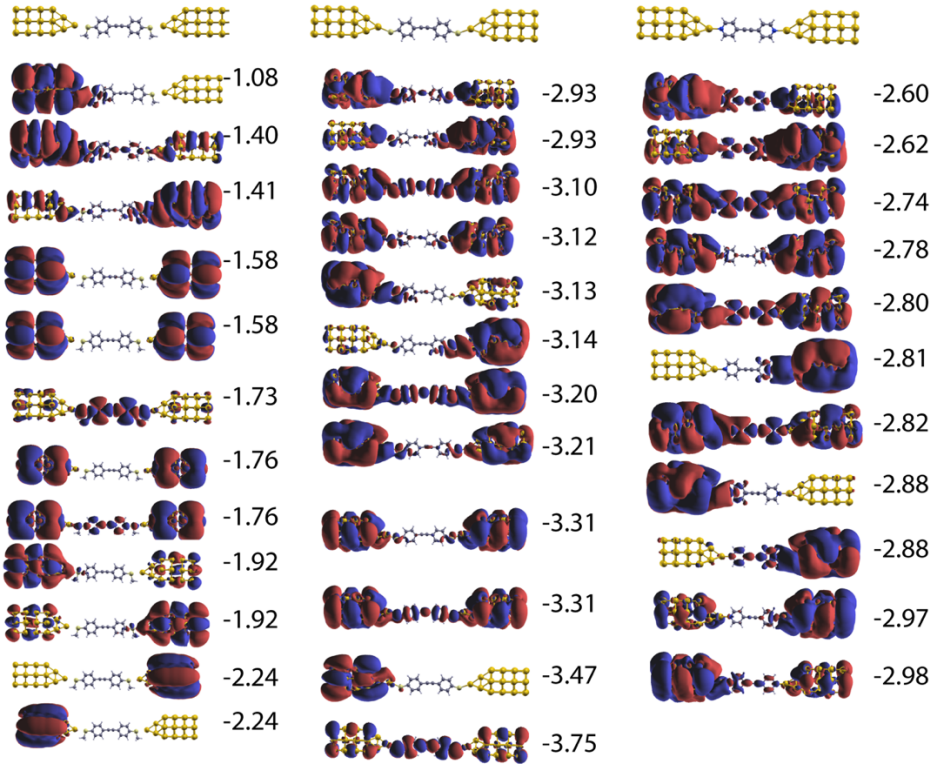

Figure 6-10 The frontier molecular orbitals close to LUMO, HOMO and LUMO for OPE-SMe, OPE-SH and OAE separately as well as the corresponding energy eigenvalues (in eV).

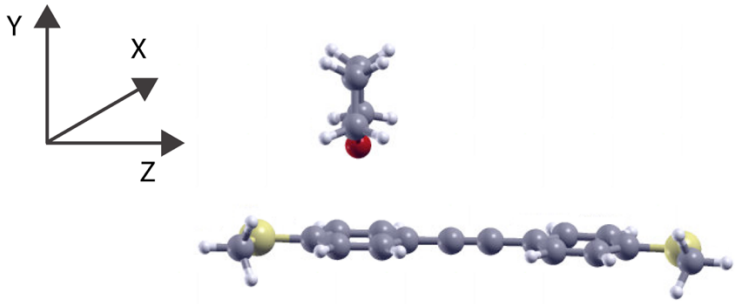

Figure 6-11 The initial conformation of OPE with one THF molecule.

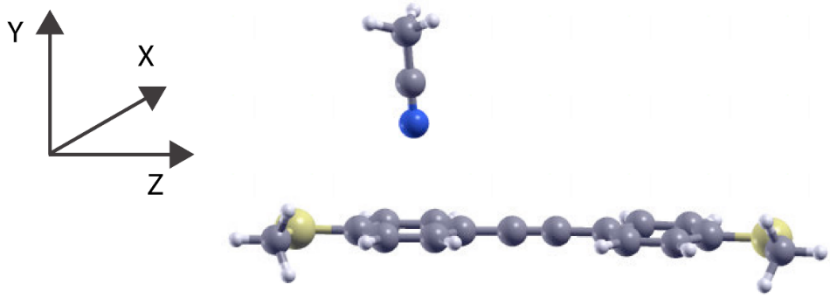

Figure 6-12 The initial conformation of OPE with one ACN molecule.

The only difference between OPE-SMe and OPE-S is the anchors, which indicates that the anchors play a predominant role in the fact whether a backbone molecule would be influenced by the gating effect of solvent or not. To gain a further insight into the origin of these gating effects, the local density states (LDOS) around LUMO, HOMO and LUMO resonances for OPE with anchors -SMe, -S and OAE with pyridyl anchor embedded in junction are shown in Figure 6-4e-g. For anchors -SMe, its LDOS mainly sit on the OPE backbone molecule, indicating a localized feature, while either the HOMO for anchor -S or the LUMO for pyridyl anchor distributes almost equally on the gold electrodes as well as the backbone molecule. (These features also could be observed from wavefunctions in Figure 6-10) In this case, the gold and molecule form a united electron system distributing on both molecule and gold atom. So they are less likely to be influenced by the gating effect of solvent. This effect could be explained by perturbation theory, because for an

extended eigenstate spread over N site, a local perturbation acting over M sites will shift the orbital energy by an amount ΔE, proportional to M/N, so if N is large, ΔE would be relatively small.

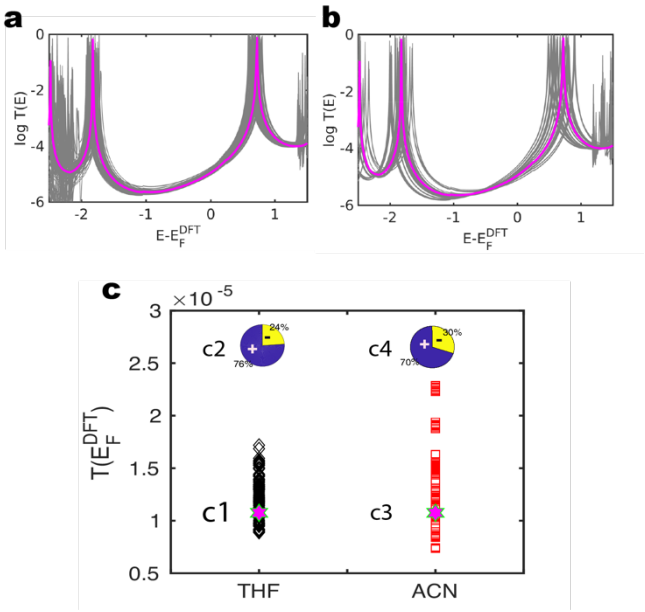

Figure 6-13 The transmission curves of 112 configurations (details see SI) for OPE with one solvent molecule (THF (a), ACN (b)), the magenta and grey curves stand for bare OPE and OPE in solvent separately. With the transmission coefficient in at DFT-predicted Fermi energy, the statistical results are shown in (c), where the magenta hexagonal stars, black diamonds and red squares present bare OPE, OPE with one THF (c1) and OPE with one ACN (c3) separately. The plus and minus signs mean conductance increase and decrease separately.

After discussing the importance of anchors on solvent gating effect, now the influence of different solvent on backbone is explored. Herein, OPE is taken as an example. For TMB, there is no influence on OPE in parallel case while a little shift appears for standing case due to the slightly positively charged H in methyl group. Therefore the influence of THF and ACN is considered in this part. In order to simulate what happens in real experiment, the initial configurations of OPE with

one THF or ACN molecule are chose as shown in Figure 6-11 and Figure 6-12, then 112 configurations are obtained by rotating THF(ACN) around x axis 10° each time until 360° and shifting THF(ACN) along the z axis 0.2 Å each time. The solvent molecule is relaxed using LDA with the backbone molecule fixed. Then they are attached to gold electrodes to get the transmission spectra.

These curves are shown in Figure 6-13a,b. Although shifting upwards and downwards of the transmission curves both possibly happen, there are more curves prefer shifting to left, indicating an increasing trend when put the OPE molecule in polarized solvent. This is attributed the negatively charged carbon atoms in the two phenyl rings of OPE, which would attract the positive part of solvent molecule. These results are clearly shown in Figure 6-13 (c2) and (c4), more than 70% of the total configurations show increasing trend, which are consistent with experimental results. For ACN, the larger conductance range are shown in Figure 6-13c and additionally, the conductance variations are more sensitive to the orientation and movement of ACN which are all attributed to the greater electric dipole momentum than THF.

6.3 Conclusion

A method to tune the single molecular conductance through control of the solvent environment has been investigated both experimentally and theoretically. The conductance of molecular wires can be manipulated to specific values within a certain range by adjusting the polarity of environment. Theoretical calculations

show that solvents can influence the molecular orbital energy in all cases, but the robustness of anchor groups decide whether the shift of conductance happens or not. This study shows a simple and widely applicable way to control single molecular charge transport.

7 Conclusion

In this thesis, I employed a combination of DFT and equilibrium Green's functions to obtain insight into the electron and phonon transport of several systems at a molecular scale. These methods are discussed in chapter 2 at length.

In chapter 3 I presented the first experimental and theoretical investigation of room-temperature QI effects in the electrical conductance of single perovskite QD junctions, using a combination of DFT and the MCBJ technique. Three distinct conductance features are observed from the conductance measurement of perovskite QDs with Br. The analysis of conductance trends with displacement reveals that the multiple conductance features are derived from the sliding of gold electrodes between the adjacent Br atoms in different unit cells. Counterintuitively, we also observe a distinct conductance jump at the end of individual conductance traces, which is direct evidence of a room-temperature QI effect. This work offers new insight into QI effects in perovskite materials at the single-unit-cell level, and offers an opportunity to explore new strategies for

optimising electron transport in perovskite QDs electronic and photoelectric devices.

In chapter 4 my theory, when compared with meaurements from experimental colleagues, reveals that the conductance of a series of cumulenes shows remarkably little dependence on the molecular length (n). This behavior is a consequence of the lack of strong bond length alternation (BLA) in these compounds, which results in a steep reduction in the HOMO-LUMO gap with increasing length. In contrast, polyynes show strong BLA resulting in an exponential attenuation of conductance with length ($\beta \approx$ 0.2–0.3 Å^{-1} at low bias voltage). The [5]cumulene exhibits a high conductance of $\log(G/G_0) = -3.7\ (\pm 0.5)$ and shows stable junctions up to a bias of 1.2 V. The discovery that cumulenes exhibit length-independent conductance suggests that they might be used to construct longer highly-conductive molecular wires. This work could be expanded with investigating the thermoelectrical property of cumulene wires since the steep reduction in the HOMO-LUMO gap could lead to higher Seebeck coefficients.

In chapter 5 I calculated the electrical conductance as a function of energy for $(Gly)_n$, $(Gly)_nC$ and $Cys(Gly)_nCys$ systems. My results show that anchors containing sulphur have significant influence on their transport properties and lead to higher β factors. Furthermore, it is also found that replacing the peptide bond with a methylene group increases the conductance of single-$(Gly)_3Cys$ molecular junctions. I also find the $(Gly)_nCys$ and $Cys(Gly)_nCys$ systems show good thermoelectrical properties with high Seebeck coefficients (~0.2 mV/K) induced by the sulphur in cysteine. After taking both phonons and electrons

contributions into account, I find the $(Gly)_1Cys$ shows good thermoelectrical properties where a high figure of merit ZT=0.8 could be achieved at room temperature. This high ZT implies that peptide-based SAM junctions are promising candidates for thermoelectric energy harvesting. In addition, due to the hydrogen bonding interactions between different oligopeptide wires, it is interesting to explore the difference behaviors (e.g. β factor) between oligopeptide and the saturated alkane wires in SAM.

In chapter 6 I investigated the effect of solvents and anchors on electric conductance, and proposed a method of tuning single-molecule conductances by controlling the solvent environment. Measurements from Xiamen University show that the conductance of molecular wires can be varied by one order of magnitude by adjusting the polarity of the environment. My theoretical calculations show that solvents can influence the molecular orbital energies, but the coupling strength of anchoring groups groups controls the magnitude of the shift. This study demonstrates that solvent-molecule interactions could provide a simple and widely applicable way to control the charge transport in single-molecule devices.

For the future, apart from the studies in this thesis, there are many other aspects that deserve our attention. Since the electric properties of single molecule devices are sensitive to the molecule-electrode contact geometry, it is challenging to obtain reproducible results. It seems that SAMs are more likely to be utilized in future applications to obtain reproducibility. It is therefore of interest to investigate the differences between charge (and phonon) transport in single molecule devices and SAMs. Moreover, more strategies are needed to enhance the thermoelectric

property of molecular devices. For example it may be possible to suppress phonon transport using supra-molecular interactions including $\pi - \pi$ stacking and hydrogen bonding. These are just a small number of the many challenges which remain to be addressed in this rapidly expanding field of research.

Bibliography

[1] E. Lörtscher, "Wiring molecules into circuits," *Nat. Nanotechnol.*, vol. 8, p. 381, Jun. 2013.

[2] D. Xiang, X. Wang, C. Jia, T. Lee, and X. Guo, "Molecular-Scale Electronics: From Concept to Function," *Chem. Rev.*, vol. 116, no. 7, pp. 4318–4440, 2016.

[3] A. T. Haedler *et al.*, "Long-range energy transport in single supramolecular nanofibres at room temperature," *Nature*, vol. 523, no. 7559, pp. 196–199, 2015.

[4] P. Gould, "Moletronics closes in on silicon," *Mater. Today*, vol. 8, no. 7, pp. 56–60, 2005.

[5] A. Batra *et al.*, "Tuning Rectification in Single-Molecular Diodes," *Nano Lett.*, vol. 13, no. 12, pp. 6233–6237, Dec. 2013.

[6] A. S. Martin, J. R. Sambles, and G. J. Ashwell, "Molecular rectifier," *Phys. Rev. Lett.*, vol. 70, no. 2, pp. 218–221, Jan. 1993.

[7] Q. Wu, S. Hou, H. Sadeghi, and C. J. Lambert, “A single-molecule porphyrin-based switch for graphene nano-gaps,” *Nanoscale*, vol. 10, no. 14, pp. 6524–6530, 2018.

[8] S. Y. Quek *et al.*, “Mechanically controlled binary conductance switching of a single-molecule junction,” *Nat. Nanotechnol.*, vol. 4, p. 230, Mar. 2009.

[9] G. E. Moore and L. Fellow, “Cramming More Components onto Integrated Circuits,” vol. 86, no. 1, pp. 82–85, 1998.

[10] M. a Ratner and Arish Aviram, “Molecular rectifiers,” *Chem. Phys. Lett.*, vol. 29, no. 2, pp. 277–283, 1974.

[11] H. Kuhn and D. Möbius, “Systems of Monomolecular Layers—Assembling and Physico-Chemical Behavior,” *Angew. Chemie Int. Ed. English*, vol. 10, no. 9, pp. 620–637, 1971.

[12] P. S. Weiss *et al.*, “Are Single Molecular Wires Conducting?,” *Science (80-.).*, vol. 271, no. 5256, pp. 1705–1707, 2006.

[13] F. Clark, J. Moreland, T. B. Laboratories, and M. Hill, “Break-junction tunneling measurements of the high-T, superconductor YtBa2Cu3O9,” *Phys. Rev. B*, vol. 35, no. 16, pp. 8856–8857, 1987.

[14] C. J. Muller, J. M. van Ruitenbeek, and L. J. de Jongh, “Experimental observation of the transition from weak link to tunnel junction,” *Phys. C Supercond. its Appl.*, vol. 191, no. 3–4, pp. 485–504, 1992.

[15] L. Sun, Y. A. Diaz-Fernandez, T. A. Gschneidtner, F. Westerlund, S. Lara-Avila,

and K. Moth-Poulsen, “Single-molecule electronics: From chemical design to functional devices,” *Chem. Soc. Rev.*, vol. 43, no. 21, pp. 7378–7411, 2014.

[16] E. Wierzbinski, X. Yin, K. Werling, and D. H. Waldeck, “The effect of oxygen heteroatoms on the single molecule conductance of saturated chains,” *J. Phys. Chem. B*, vol. 117, no. 16, pp. 4431–4441, 2013.

[17] M. L. Perrin *et al.*, “Large tunable image-charge effects in single-molecule junctions,” *Nat. Nanotechnol.*, vol. 8, no. 4, pp. 282–287, 2013.

[18] B. Xu and N. J. Tao, “Measurement of single molecule resistance by repeated formation of molecular junctions,” *Science (80-.).*, vol. 301, no. August, pp. 1221–1223, 2003.

[19] Z. Tan *et al.*, “Atomically defined angstrom-scale all-carbon junctions,” *Nat. Commun.*, vol. 10, no. 1, p. 1748, 2019.

[20] J. M. Soler *et al.*, “The SIESTA method for *ab initio* order- *N* materials simulation,” *J. Phys. Condens. Matter*, vol. 14, no. 11, pp. 2745–2779, Mar. 2002.

[21] J. Ferrer *et al.*, “GOLLUM: a next-generation simulation tool for electron, thermal and spin transport,” *New J. Phys.*, vol. 16, no. 9, p. 093029, Sep. 2014.

[22] C. J. Lambert, “Basic concepts of quantum interference and electron transport in single-molecule electronics,” *Chem. Soc. Rev.*, vol. 44, no. 4, pp. 875–888, 2015.

[23] W. Kohn, “Nobel Lecture: Electronic structure of matter—wave functions

and density functionals," *Rev. Mod. Phys.*, vol. 71, no. 5, pp. 1253–1266, 1999.

[24] C. M. Guédon, H. Valkenier, T. Markussen, K. S. Thygesen, J. C. Hummelen, and S. J. van der Molen, "Observation of quantum interference in molecular charge transport," *Nat. Nanotechnol.*, vol. 7, p. 305, Mar. 2012.

[25] C. M. Finch, V. M. Garc\'\ia-Suárez, and C. J. Lambert, "Giant thermopower and figure of merit in single-molecule devices," *Phys. Rev. B*, vol. 79, no. 3, p. 33405, Jan. 2009.

[26] K. K. Saha, B. K. Nikoli\ifmmode \acutec\else ć\fi, V. Meunier, W. Lu, and J. Bernholc, "Quantum-Interference-Controlled Three-Terminal Molecular Transistors Based on a Single Ring-Shaped Molecule Connected to Graphene Nanoribbon Electrodes," *Phys. Rev. Lett.*, vol. 105, no. 23, p. 236803, Dec. 2010.

[27] X. Liu *et al.*, "Gating of Quantum Interference in Molecular Junctions by Heteroatom Substitution," *Angew. Chemie - Int. Ed.*, vol. 56, no. 1, pp. 173–176, 2017.

[28] S. Sangtarash, H. Sadeghi, and C. J. Lambert, "Exploring quantum interference in heteroatom-substituted graphene-like molecules," *Nanoscale*, vol. 8, no. 27, pp. 13199–13205, 2016.

[29] Y. Yang *et al.*, "Heteroatom-Induced Molecular Asymmetry Tunes Quantum Interference in Charge Transport through Single-Molecule Junctions," *J. Phys. Chem. C*, vol. 122, no. 26, pp. 14965–14970, Jul. 2018.

[30] M. H. Garner *et al.*, "Comprehensive suppression of single-molecule conductance using destructive σ-interference," *Nature*, vol. 558, no. 7710, pp. 415–419, 2018.

[31] Z.-K. Tan *et al.*, "Bright light-emitting diodes based on organometal halide perovskite," *Nat. Nanotechnol.*, vol. 9, p. 687, Aug. 2014.

[32] H. Takashima *et al.*, "Low-Driving-Voltage Electroluminescence in Perovskite Films," *Adv. Mater.*, vol. 21, no. 36, pp. 3699–3702, Sep. 2009.

[33] X. Hu *et al.*, "High-Performance Flexible Broadband Photodetector Based on Organolead Halide Perovskite," *Adv. Funct. Mater.*, vol. 24, no. 46, pp. 7373–7380, Dec. 2014.

[34] Y. Lin, G. Lin, B. Sun, and X. Guo, "Nanocrystalline Perovskite Hybrid Photodetectors with High Performance in Almost Every Figure of Merit," *Adv. Funct. Mater.*, vol. 28, no. 7, p. 1705589, Feb. 2018.

[35] L. Liu *et al.*, "Grain-Boundary 'Patches' by In Situ Conversion to Enhance Perovskite Solar Cells Stability," *Adv. Mater.*, vol. 30, no. 29, p. 1800544, Jul. 2018.

[36] G. Fang *et al.*, "Differential Pd-nanocrystal facets demonstrate distinct antibacterial activity against Gram-positive and Gram-negative bacteria," *Nat. Commun.*, vol. 9, no. 1, p. 129, 2018.

[37] M. Liu, M. B. Johnston, and H. J. Snaith, "Efficient planar heterojunction perovskite solar cells by vapour deposition," *Nature*, vol. 501, p. 395, Sep.

2013.

[38] V. Malgras *et al.*, "Observation of Quantum Confinement in Monodisperse Methylammonium Lead Halide Perovskite Nanocrystals Embedded in Mesoporous Silica," *J. Am. Chem. Soc.*, vol. 138, no. 42, pp. 13874–13881, Oct. 2016.

[39] D. Shi *et al.*, "Low trap-state density and long carrier diffusion in organolead trihalide perovskite single crystals," *Science (80-.).*, vol. 347, no. 6221, pp. 519–522, 2015.

[40] H. Song, M. A. Reed, and T. Lee, "Single Molecule Electronic Devices," *Adv. Mater.*, vol. 23, no. 14, pp. 1583–1608, Apr. 2011.

[41] S. Fujii *et al.*, "Rectifying Electron-Transport Properties through Stacks of Aromatic Molecules Inserted into a Self-Assembled Cage," *J. Am. Chem. Soc.*, vol. 137, no. 18, pp. 5939–5947, May 2015.

[42] W. Zhang *et al.*, "Single-Molecule Conductance of Viologen–Cucurbit[8]uril Host–Guest Complexes," *ACS Nano*, vol. 10, no. 5, pp. 5212–5220, May 2016.

[43] M. Famili *et al.*, "Self-Assembled Molecular-Electronic Films Controlled by Room Temperature Quantum Interference," *Chem*, vol. 5, no. 2, pp. 474–484, Feb. 2019.

[44] T. Morita and S. Lindsay, "Determination of single molecule conductances of alkanedithiols by conducting-atomic force microscopy with large gold nanoparticles," *J. Am. Chem. Soc.*, vol. 129, no. 23, pp. 7262–7263, 2007.

[45] G. Lovat, B. Choi, D. W. Paley, M. L. Steigerwald, L. Venkataraman, and X. Roy, "Room-temperature current blockade in atomically defined single-cluster junctions," *Nat. Nanotechnol.*, vol. 12, p. 1050, Aug. 2017.

[46] L. Xiang *et al.*, "Non-exponential Length Dependence of Conductance in Iodide-Terminated Oligothiophene Single-Molecule Tunneling Junctions," *J. Am. Chem. Soc.*, vol. 138, no. 2, pp. 679–687, Jan. 2016.

[47] E. Leary, A. La Rosa, M. T. González, G. Rubio-Bollinger, N. Agraït, and N. Martín, "Incorporating single molecules into electrical circuits. The role of the chemical anchoring group," *Chem. Soc. Rev.*, vol. 44, no. 4, pp. 920–942, 2015.

[48] L.-L. Peng *et al.*, "Low Tunneling Decay of Iodine-Terminated Alkane Single-Molecule Junctions," *Nanoscale Res. Lett.*, vol. 13, no. 1, p. 121, 2018.

[49] C. J. Lambert and S. X. Liu, "A Magic Ratio Rule for Beginners: A Chemist's Guide to Quantum Interference in Molecules," *Chem. - A Eur. J.*, vol. 24, no. 17, pp. 4193–4201, 2018.

[50] X. Zhao, V. Geskin, and R. Stadler, "Destructive quantum interference in electron transport: A reconciliation of the molecular orbital and the atomic orbital perspective," *J. Chem. Phys.*, vol. 146, no. 9, p. 092308, 2017.

[51] G. Giorgi, T. Yoshihara, and K. Yamashita, "Structural and electronic features of small hybrid organic-inorganic halide perovskite clusters: A theoretical analysis," *Phys. Chem. Chem. Phys.*, vol. 18, no. 39, pp. 27124–27132, 2016.

[52] F. Zhang *et al.*, "Brightly Luminescent and Color-Tunable Colloidal CH3NH3PbX3 (X = Br, I, Cl) Quantum Dots: Potential Alternatives for Display Technology," *ACS Nano*, vol. 9, no. 4, pp. 4533–4542, Apr. 2015.

[53] W. Hong *et al.*, "An MCBJ case study: The influence of π-conjugation on the single-molecule conductance at a solid/liquid interface," *Beilstein J. Nanotechnol.*, vol. 2, no. 1, pp. 699–713, 2011.

[54] R. Frisenda, V. A. E. C. Janssen, F. C. Grozema, H. S. J. Van Der Zant, and N. Renaud, "Mechanically controlled quantum interference in individual Ï-stacked dimers," *Nat. Chem.*, vol. 8, no. 12, pp. 1099–1104, 2016.

[55] M. Frei, S. V Aradhya, M. Koentopp, M. S. Hybertsen, and L. Venkataraman, "Mechanics and Chemistry: Single Molecule Bond Rupture Forces Correlate with Molecular Backbone Structure," *Nano Lett.*, vol. 11, no. 4, pp. 1518–1523, Apr. 2011.

[56] A. Pan *et al.*, "Insight into the Ligand-Mediated Synthesis of Colloidal CsPbBr3 Perovskite Nanocrystals: The Role of Organic Acid, Base, and Cesium Precursors," *ACS Nano*, vol. 10, no. 8, pp. 7943–7954, Aug. 2016.

[57] S. Sourisseau *et al.*, "Reduced Band Gap Hybrid Perovskites Resulting from Combined Hydrogen and Halogen Bonding at the Organic—Inorganic Interface," *Chem. Mater.*, vol. 19, no. 3, pp. 600–607, Feb. 2007.

[58] J. F. Li *et al.*, "Shell-isolated nanoparticle-enhanced Raman spectroscopy," *Nature*, vol. 464, p. 392, Mar. 2010.

[59] H.-X. Lin *et al.*, "Constructing Two-Dimensional Nanoparticle Arrays on Layered Materials Inspired by Atomic Epitaxial Growth," *J. Am. Chem. Soc.*, vol. 137, no. 8, pp. 2828–2831, Mar. 2015.

[60] J. M. Soler *et al.*, "SIESTA Method For Ab Initio Order-N Materials Simulation, The," *J. Phys. Condens. Matter*, vol. 14, no. 11, pp. 2745–2779, 2002.

[61] J. Ferrer *et al.*, "GOLLUM: A next-generation simulation tool for electron, thermal and spin transport," *New J. Phys.*, vol. 16, p. 093029, 2014.

[62] Z. Yang *et al.*, " Two-Inch-Sized Perovskite CH 3 NH 3 PbX 3 (X = Cl, Br, I) Crystals: Growth and Characterization ," *Adv. Mater.*, vol. 27, no. 35, pp. 5176–5183, 2015.

[63] B. Capozzi, E. J. Dell, T. C. Berkelbach, D. R. Reichman, L. Venkataraman, and L. M. Campos, "Length-Dependent Conductance of Oligothiophenes," *J. Am. Chem. Soc.*, vol. 136, no. 29, pp. 10486–10492, Jul. 2014.

[64] Q. Lu, K. Liu, H. Zhang, Z. Du, X. Wang, and F. Wang, "From Tunneling to Hopping: A Comprehensive Investigation of Charge Transport Mechanism in Molecular Junctions Based on Oligo(p-phenylene ethynylene)s," *ACS Nano*, vol. 3, no. 12, pp. 3861–3868, Dec. 2009.

[65] Y. Zang *et al.*, "Resonant Transport in Single Diketopyrrolopyrrole Junctions," *J. Am. Chem. Soc.*, vol. 140, no. 41, pp. 13167–13170, Oct. 2018.

[66] A. Nitzan, "ELECTRON TRANSMISSION THROUGH MOLECULES AND MOLECULAR INTERFACES," *Annu. Rev. Phys. Chem.*, vol. 52, no. 1, pp. 681–

750, Oct. 2001.

[67] J. He *et al.*, "Electronic Decay Constant of Carotenoid Polyenes from Single-Molecule Measurements," *J. Am. Chem. Soc.*, vol. 127, no. 5, pp. 1384–1385, Feb. 2005.

[68] I. Visoly-Fisher *et al.*, "Conductance of a biomolecular wire.," *Proc. Natl. Acad. Sci. U. S. A.*, vol. 103, no. 23, pp. 8686–90, Jun. 2006.

[69] W. Chen *et al.*, "Highly Conducting π-Conjugated Molecular Junctions Covalently Bonded to Gold Electrodes," *J. Am. Chem. Soc.*, vol. 133, no. 43, pp. 17160–17163, Nov. 2011.

[70] E. Leary *et al.*, "Bias-Driven Conductance Increase with Length in Porphyrin Tapes," *J. Am. Chem. Soc.*, vol. 140, no. 40, pp. 12877–12883, Oct. 2018.

[71] Y. Tsuji, R. Movassagh, S. Datta, and R. Hoffmann, "Exponential Attenuation of Through-Bond Transmission in a Polyene: Theory and Potential Realizations," *ACS Nano*, vol. 9, no. 11, pp. 11109–11120, Nov. 2015.

[72] M. H. Garner, W. Bro-Jørgensen, P. D. Pedersen, and G. C. Solomon, "Reverse Bond-Length Alternation in Cumulenes: Candidates for Increasing Electronic Transmission with Length," *J. Phys. Chem. C*, vol. 122, no. 47, pp. 26777–26789, Nov. 2018.

[73] D. Wendinger and R. R. Tykwinski, "Odd [n]Cumulenes ($n = 3, 5, 7, 9$): Synthesis, Characterization, and Reactivity," *Acc. Chem. Res.*, vol. 50, no. 6, pp. 1468–1479, Jun. 2017.

[74] J. A. Januszewski and R. R. Tykwinski, "Synthesis and properties of long [*n*]cumulenes ($n \geq 5$)," *Chem. Soc. Rev.*, vol. 43, no. 9, pp. 3184–3203, 2014.

[75] J. A. Januszewski, D. Wendinger, C. D. Methfessel, F. Hampel, and R. R. Tykwinski, "Synthesis and Structure of Tetraarylcumulenes: Characterization of Bond-Length Alternation versus Molecule Length," *Angew. Chemie Int. Ed.*, vol. 52, no. 6, pp. 1817–1821, Feb. 2013.

[76] S. Gunasekaran, D. Hernangómez-Pérez, I. Davydenko, S. Marder, F. Evers, and L. Venkataraman, "Near Length-Independent Conductance in Polymethine Molecular Wires," *Nano Lett.*, vol. 18, no. 10, pp. 6387–6391, Oct. 2018.

[77] M. Tommasini *et al.*, "π-Conjugation and End Group Effects in Long Cumulenes: Raman Spectroscopy and DFT Calculations," *J. Phys. Chem. C*, vol. 118, no. 45, pp. 26415–26425, Nov. 2014.

[78] X. Fang *et al.*, "Facile Synthesis, Macroscopic Separation, E/Z Isomerization, and Distinct AIE properties of Pure Stereoisomers of an Oxetane-Substituted Tetraphenylethene Luminogen," *Chem. Mater.*, vol. 28, no. 18, pp. 6628–6636, Sep. 2016.

[79] M. U. Bühringer *et al.*, "Double Bonds? Studies on the Barrier to Rotation about the Cumulenic C=C Bonds of Tetraaryl[*n*]cumulenes ($n = 3, 5, 7, 9$)," *Angew. Chemie Int. Ed.*, vol. 57, no. 27, pp. 8321–8325, Jul. 2018.

[80] E. Leary *et al.*, "Detecting Mechanochemical Atropisomerization within an STM Break Junction.," *J. Am. Chem. Soc.*, vol. 140, no. 2, pp. 710–718, Jan.

2018.

[81] M. T. González *et al.*, "Structural versus Electrical Functionalization of Oligo(phenylene ethynylene) Diamine Molecular Junctions," *J. Phys. Chem. C*, vol. 118, no. 37, pp. 21655–21662, Sep. 2014.

[82] J. M. Soler *et al.*, "The SIESTA method for ab initio order N materials simulation," *J. Phys. Condens. Matter*, vol. 14, no. 11, pp. 2745–2779, 2002.

[83] Z. Berkovitch-Yellin and L. Leiserowitz, "Electron density distribution in cumulenes: an X-ray study of tetraphenylbutatriene at 20°C and –160°C," *Acta Crystallogr. Sect. B Struct. Crystallogr. Cryst. Chem.*, vol. 33, no. 12, pp. 3657–3669, 1977.

[84] E. J. Baerends, O. V. Gritsenko, and R. van Meer, "The Kohn–Sham gap, the fundamental gap and the optical gap: the physical meaning of occupied and virtual Kohn–Sham orbital energies," *Phys. Chem. Chem. Phys.*, vol. 15, no. 39, p. 16408, 2013.

[85] F. Chen and N. J. Tao, "Electron Transport in Single Molecules: From Benzene to Graphene," *Acc. Chem. Res.*, vol. 42, no. 3, pp. 429–438, Mar. 2009.

[86] S. Tsukamoto and K. Hirose, "Electron-transport properties of Na nanowires under applied bias voltages," *Phys. Rev. B*, vol. 66, no. 16, p. 161402, Oct. 2002.

[87] J.-X. Yu, Y. Cheng, S. Sanvito, and X.-R. Chen, "Bias-dependent oscillatory electron transport of monatomic sulfur chains," *Appl. Phys. Lett.*, vol. 100,

no. 10, p. 103110, Mar. 2012.

[88] R. H. M. Smit, C. Untiedt, G. Rubio-Bollinger, R. C. Segers, and J. M. van Ruitenbeek, "Observation of a Parity Oscillation in the Conductance of Atomic Wires," *Phys. Rev. Lett.*, vol. 91, no. 7, p. 076805, Aug. 2003.

[89] H.-S. Sim, H.-W. Lee, and K. J. Chang, "Even-Odd Behavior of Conductance in Monatomic Sodium Wires," *Phys. Rev. Lett.*, vol. 87, no. 9, p. 096803, Aug. 2001.

[90] P. Gawel *et al.*, "Push-Pull Buta-1,2,3-trienes: Exceptionally Low Rotational Barriers of Cumulenic C=C Bonds and Proacetylenic Reactivity," *Chem. - A Eur. J.*, vol. 21, no. 16, pp. 6215–6225, 2015.

[91] M. Franz *et al.*, "Cumulene Rotaxanes: Stabilization and Study of [9]Cumulenes," *Angew. Chemie Int. Ed.*, vol. 54, no. 22, pp. 6645–6649, May 2015.

[92] H. B. Gray and J. R. Winkler, "Electron tunneling through proteins," *Q. Rev. Biophys.*, vol. 36, no. 3, pp. 341–372, 2003.

[93] B. Giese, M. Graber, and M. Cordes, "Electron transfer in peptides and proteins," *Curr. Opin. Chem. Biol.*, vol. 12, no. 6, pp. 755–759, 2008.

[94] P. G. Falkowski, T. Fenchel, and E. F. Delong, "The Microbial Engines That Drive Earth 's Biogeochemical Cycles," *Science (80-.).*, vol. 320, no. 5879, pp. 1034–1039, 2008.

[95] J. Juhaniewicz, J. Pawlowski, and S. Sek, "Electron Transport Mediated by

Peptides Immobilized on Surfaces," *Isr. J. Chem.*, vol. 55, no. 6, pp. 645–660, 2015.

[96] S. Sek, "Review: Peptides and proteins wired into the electrical circuits: an SPM-based approach," *Biopolymers*, vol. 100, no. 1, pp. 71–81, 2013.

[97] N. Amdursky, "Electron Transfer across Helical Peptides," *Chempluschem*, vol. 80, no. 7, pp. 1075–1095, 2015.

[98] N. Amdursky, D. Marchak, L. Sepunaru, I. Pecht, M. Sheves, and D. Cahen, "Electronic Transport via Proteins," *Adv. Mater.*, vol. 26, no. 42, pp. 7142–7161, 2014.

[99] Y. K. Shin, M. D. Newton, and S. S. Isied, "Distance dependence of electron transfer across peptides with different secondary structures: The role of peptide energetics and electronic coupling," *J. Am. Chem. Soc.*, vol. 125, no. 13, pp. 3722–3732, 2003.

[100] J. Gao *et al.*, "Electron transfer in peptides: The influence of charged amino acids," *Angew. Chemie - Int. Ed.*, vol. 50, no. 8, pp. 1926–1930, 2011.

[101] M. Baghbanzadeh *et al.*, "Charge tunneling along short oligoglycine chains," *Angew. Chemie - Int. Ed.*, vol. 54, no. 49, pp. 14743–14747, 2015.

[102] R. A. Malak, Z. Gao, J. F. Wishart, and S. S. Isied, "Long-range electron transfer across peptide bridges: The transition from electron superexchange to hopping," *J. Am. Chem. Soc.*, vol. 126, no. 43, pp. 13888–13889, 2004.

[103] R. A. Marcus and N. Sutin, "Electron transfers in chemistry and biology," *BBA*

Rev. Bioenerg., vol. 811, no. 3, pp. 265–322, 1985.

[104] M. Magoga and C. Joachim, "Conductance and transparence of long molecular wires," *Phys. Rev. B - Condens. Matter Mater. Phys.*, vol. 56, no. 8, pp. 4722–4729, 1997.

[105] X. Xiao, B. Xu, and N. Tao, "Conductance Titration of Single-Peptide Molecules," *J. Am. Chem. Soc.*, vol. 126, no. 17, pp. 5370–5371, 2004.

[106] J. M. Brisendine *et al.*, "Probing Charge Transport through Peptide Bonds," *J. Phys. Chem. Lett.*, vol. 9, no. 4, pp. 763–767, 2018.

[107] E. Lörtscher, C. J. Cho, M. Mayor, M. Tschudy, C. Rettner, and H. Riel, "Influence of the anchor group on charge transport through single-molecule junctions," *ChemPhysChem*, vol. 12, no. 9, pp. 1677–1682, 2011.

[108] V. Obersteiner, D. A. Egger, and E. Zojer, "Impact of Anchoring Groups on Ballistic Transport: Single Molecule vs Monolayer Junctions," *J. Phys. Chem. C*, vol. 119, no. 36, pp. 21198–21208, 2015.

[109] B. Kim, S. H. Choi, X. Y. Zhu, and C. D. Frisbie, "Molecular tunnel junctions based on π-conjugated oligoacene thiols and dithiols between Ag, Au, and Pt contacts: Effect of surface linking group and metal work function," *J. Am. Chem. Soc.*, vol. 133, no. 49, pp. 19864–19877, 2011.

[110] F. Chen, X. Li, J. Hihath, Z. Huang, and N. Tao, "Effect of anchoring groups on single-molecule conductance: Comparative study of thiol-, amine-, and carboxylic-acid-terminated molecules," *J. Am. Chem. Soc.*, vol. 128, no. 49,

pp. 15874–15881, 2006.

[111] S. Sangtarash *et al.*, "Gateway state-mediated, long-range tunnelling in molecular wires," *Nanoscale*, vol. 10, no. 6, pp. 3060–3067, 2018.

[112] Q. Zhang, Y. Sun, W. Xu, and D. Zhu, "Organic Thermoelectric Materials: Emerging Green Energy Materials Converting Heat to Electricity Directly and Efficiently," *Adv. Mater.*, vol. 26, no. 40, pp. 6829–6851, 2014.

[113] H. Karamitaheri, M. Pourfath, R. Faez, and H. Kosina, "Geometrical effects on the thermoelectric properties of ballistic graphene antidot lattices," in *Journal of Applied Physics*, 2011, vol. 110, no. 5, p. 054506.

[114] V. M. Garcia-Suarez, R. Ferrads, and J. Ferrer, "Impact of Fano and Breit-Wigner resonances in the thermoelectric properties of nanoscale junctions," *Phys. Rev. B - Condens. Matter Mater. Phys.*, vol. 88, no. 23, p. 235417, 2013.

[115] Q. Wu, H. Sadeghi, V. M. García-Suárez, J. Ferrer, and C. J. Lambert, "Thermoelectricity in vertical graphene-C60-graphene architectures," *Sci. Rep.*, vol. 7, p. 11680, 2017.

[116] Q. Wu, H. Sadeghi, and C. Lambert, "MoS2 nano flakes with self-adaptive contacts for efficient thermoelectric energy harvesting," *Nanoscale*, vol. 10, pp. 7575–7580, 2018.

[117] R. Venkatasubramanian, E. Siivola, T. Colpitts, and B. O'Quinn, "Thin-film thermoelectric devices with high room-temperature figures of merit," *Nature*, vol. 413, no. 6856, pp. 597–602, 2001.

[118] L. Sepunaru *et al.*, "Electronic transport via homopeptides: The role of side chains and secondary structure," *J. Am. Chem. Soc.*, vol. 137, no. 30, pp. 9617–9626, 2015.

[119] H. Uji, T. Morita, and S. Kimura, "Molecular direction dependence of single-molecule conductance of a helical peptide in molecular junction," *Phys. Chem. Chem. Phys.*, vol. 15, no. 3, pp. 757–760, 2013.

[120] J. Juhaniewicz and S. Sek, "Peptide molecular junctions: Distance dependent electron transmission through oligoprolines," *Bioelectrochemistry*, vol. 87, pp. 21–27, 2012.

[121] X. Roy, M. L. Steigerwald, and L. Venkataraman, "Electronic transport and mechanical stability of carboxyl linked," *Phys. Chem. Chem. Phys.*, vol. 14, pp. 13841–13845, 2012.

[122] E. Leary *et al.*, "Single-molecule solvation-shell sensing," *Phys. Rev. Lett.*, vol. 102, no. 8, pp. 1–4, 2009.

[123] C. Guo *et al.*, "Tuning electronic transport via hepta-alanine peptides junction by tryptophan doping," *Proc. Natl. Acad. Sci.*, vol. 113, no. 39, pp. 10785–10790, 2016.

[124] D. N. B. Tatiana R. Prytkova, Igor V. Kurnikov, "Coupling Coherence Distinguishes Structure Sensitivity in Protein Electron Transfer," *Science (80-.).*, vol. 315, no. February, pp. 622–626, 2007.

[125] M. Wang *et al.*, "Effect of molecular conformations on the electronic

transport in oxygen-substituted alkanethiol molecular junctions Effect of molecular conformations on the electronic transport in oxygen-substituted alkanethiol molecular junctions," vol. 184703, 2018.

[126] Z. Xie, I. Bâldea, S. Oram, C. E. Smith, and C. D. Frisbie, "Effect of Heteroatom Substitution on Transport in Alkanedithiol-Based Molecular Tunnel Junctions: Evidence for Universal Behavior," *ACS Nano*, vol. 11, no. 1, pp. 569–578, 2017.

[127] M. G. Reuter, M. C. Hersam, T. Seideman, and M. A. Ratner, "Signatures of Cooperative E ff ects and Transport Mechanisms in Conductance Histograms," *Nano Lett.*, vol. 12, no. 5, pp. 2243–2248, 2012.

[128] C. S. S. Sangeeth, L. Jiang, and C. A. Nijhuis, "Bottom-electrode induced defects in self-assembled monolayer (SAM)-based tunnel junctions affect only the SAM resistance, not the contact resistance or SAM capacitance," *RSC Adv.*, vol. 8, no. 36, pp. 19939–19949, 2018.

[129] J. P. Small, K. M. Perez, and P. Kim, "Modulation of thermoelectric power of individual carbon nanotubes," *Phys. Rev. Lett.*, vol. 91, no. 25, pp. 1–4, 2003.

[130] M. Jonson and G. D. Mahan, "Mott's formula for the thermopower and the Wiedemann-Franz law," *Phys. Rev. B*, vol. 21, no. 10, pp. 4223–4229, 1980.

[131] A. M. Lunde and K. Flensberg, "On the Mott formula for the thermopower of non-interacting electrons in quantum point contacts," *J. Phys. Condens. Matter*, vol. 17, no. 25, pp. 3879–3884, 2005.

[132] O. Bubnova and X. Crispin, “Towards polymer-based organic thermoelectric generators,” *Energy Environ. Sci.*, vol. 5, no. 11, pp. 9345–9362, 2012.

[133] M.~A.~Reed, C.~Zhou, C.~J.~Muller, T.~P.~Burgin, and J.~M.~Tour, “Conductance of a Molecular Junction,” *Science (80-.).*, vol. 278, no. October, p. 252, 1997.

[134] E. Lörtscher, J. W. Ciszek, J. Tour, and H. Riel, “Reversible and Controllable Switching of a Single-Molecule Junction,” *Small*, vol. 2, no. 8–9, pp. 973–977, Aug. 2006.

[135] E. Leary *et al.*, “Single-Molecule Solvation-Shell Sensing,” *Phys. Rev. Lett.*, vol. 102, no. 8, p. 086801, Feb. 2009.

[136] D. C. Milan *et al.*, “Solvent Dependence of the Single Molecule Conductance of Oligoyne-Based Molecular Wires,” *J. Phys. Chem. C*, vol. 120, no. 29, pp. 15666–15674, 2016.

[137] G. Yang *et al.*, “Protonation tuning of quantum interference in azulene-type single-molecule junctions,” *Chem. Sci.*, vol. 8, no. 11, pp. 7505–7509, 2017.

[138] V. Fatemi, M. Kamenetska, J. B. Neaton, and L. Venkataraman, “Environmental Control of Single-Molecule Junction Transport,” *Nano Lett.*, vol. 11, no. 5, pp. 1988–1992, May 2011.

[139] M. Kotiuga, P. Darancet, C. R. Arroyo, L. Venkataraman, and J. B. Neaton, “Adsorption-Induced Solvent-Based Electrostatic Gating of Charge Transport through Molecular Junctions,” *Nano Lett.*, vol. 15, no. 7, pp. 4498–

4503, Jul. 2015.

[140] R. Li *et al.*, "Switching of Charge Transport Pathways via Delocalization Changes in Single-Molecule Metallacycles Junctions," *J. Am. Chem. Soc.*, vol. 139, no. 41, pp. 14344–14347, Oct. 2017.

[141] W. Hong *et al.*, "Single Molecular Conductance of Tolanes: Experimental and Theoretical Study on the Junction Evolution Dependent on the Anchoring Group," *J. Am. Chem. Soc.*, vol. 134, no. 4, pp. 2292–2304, Feb. 2012.

[142] X. Li, J. He, J. Hihath, B. Xu, S. M. Lindsay, and N. Tao, "Conductance of Single Alkanedithiols: Conduction Mechanism and Effect of Molecule—Electrode Contacts," *J. Am. Chem. Soc.*, vol. 128, no. 6, pp. 2135–2141, Feb. 2006.